Università di Pisa

Galileo Galilei School of Graduate Studies
Applied Physics Course
FIS/01

XVII Ciclo 2002–2004

Ph.D. Thesis

Modeling some Sources of Thermal Noise through Finite Element Analysis: Application to the Virgo Interferometric Antenna.

Candidate	*Advisor*
Enrico Campagna	Flavio Vetrano

Contents

Introduction

Gravitational waves are a prediction of general relativity but have not yet been directly detected.

Ground based interferometric antennae like Virgo, LIGO or GEO600 aim at doing it in the next years.

Virgo sensitivity extends from a few Hz to a few kHz and is limited at low frequency (around 5 Hz) by seismic and gravity gradient noise and at high frequencies (over 500Hz) by shot noise. In the intermediate frequency range there are two noise floors, due to pendulum thermal noise (below 100 Hz) and to mirror thermal noise (over 100 Hz). Therefore, the comprehension and the modelization of the thermal noise in its various aspects is of crucial importance for Virgo and for any interferometer of the 2$^{\mathrm{nd}}$ or 3$^{\mathrm{rd}}$ generation too.

The main problem is that the real components of the suspension system are more complex than the ideal ones used for thermal noise analytical calculations: the symmetry of the problem can be very different from the one used in the theoretical models. Therefore, at the level of sensitivity involved, even small geometric deviations are important. It is necessary to have a flexible tool for investigating thermal noise effects with the *actual* designed mirror and mirror suspensions: finite element analysis.

Secondly, especially in the context of R&D activities, looking at cryogenic interferometric detectors as a new workable solution, it is interesting to study new materials, characterizing *ex novo* their thermomechanical properties. Silicon is a very promising candidate and it is worthwhile to build up an experiment to test crystalline silicon fibers to be used as future suspensions.

Chapter 1

Gravitational Waves

Since the theory of gravitation was stated, many efforts have been made to detect gravitational wave radiation. Gravitational waves come directly as a solution of Einstein field equations [1] in the weak field approximation and they are a spin-2 metric distortion that propagates at the speed of light. Their emission takes place during catastrophic cosmic events that involve large masses rapidly changing their distribution — e.g. coalescing binary systems, asymmetric pulsars or the Big bang itself.

There are many experiments around the world that are active at the moment but none of them has detected anything yet. Gravitational wave emission and propagation processes are well theorised, and with the study on the revolution period of the binary pulsar system PSR1913+16 the existence of gravitational radiation was indirectly proved [2]. The problem of direct detection lies on the extremely small coupling of the gravitational field. For this reason all the experiments implemented for their detection — from the resonant bar to the interferometer antennas — have to face great technical problems to reach the needed sensitivities.

1.1 Propagation

1.1.1 Theory of General Relativity

According to the theory of general relativity space and time are merged together in a 4-dimensional manifold. The presence of masses on this manifold causes its distortion and, on the other hand, the distortion of the 4-dimensional space governs the dynamics of the masses on it. This is the kernel concept that is embedded in the Einstein field equations that can be written as

$$G_{\mu\nu} = 8\pi G T_{\mu\nu} \ , \tag{1.1}$$

where $G_{\mu\nu}$ is the Einstein tensor and $T_{\mu\nu}$ is the energy-momentum tensor, representing the distribution of mass and energy in the space-time. To identify the Einstein tensor other basic definitions are needed: first of all the metric tensor $g_{\mu\nu}$, which defines the distance ds of two slightly separate points

$$ds^2 = g_{\mu\nu} dx^\mu dx^\nu \tag{1.2}$$

and it's used to raise and lower the indexes of the other tensors; then the affine connection ${\Gamma^\mu}_{\nu\lambda}$

$${\Gamma^\mu}_{\nu\lambda} \doteq \frac{1}{2} g^{\mu\alpha}(g_{\alpha\nu,\lambda} + g_{\alpha\lambda,\nu} - g_{\nu\lambda,\alpha}) \tag{1.3}$$

and the Riemann tensor defined using the affine connection

$${R^\mu}_{\nu\alpha\beta} \doteq {\Gamma^\mu}_{\nu\beta,\alpha} - {\Gamma^\mu}_{\nu\alpha,\beta} + {\Gamma^\mu}_{\gamma\alpha}{\Gamma^\gamma}_{\nu\beta} - {\Gamma^\mu}_{\gamma\beta}{\Gamma^\gamma}_{\nu\alpha} \ . \tag{1.4}$$

Introducing the Ricci tensor and the Ricci scalar

$$R_{\mu\nu} \doteq {R^\alpha}_{\mu\alpha\nu} \ , \tag{1.5}$$

$$R \doteq {R^\alpha}_\alpha \ , \tag{1.6}$$

the Einstein tensor is defined as

$$G_{\mu\nu} \doteq R_{\mu\nu} - \frac{1}{2} g_{\mu\nu} R \ . \tag{1.7}$$

1.1.2 The weak-field approximation

Owing to the non-linearity of Einstein field equations, it's very hard to find general radiative solutions to them. In fact, any solution carries energy and momentum that modify the second member of the equation itself. One approach can be to study the weak-field radiative solution which describes waves carrying not enough energy and momentum to affect their own propagation. This seems reasonable because any observable gravitational radiation is likely to be of very low intensity. Suppose to have a metric $g_{\mu\nu}$ differing from the Minkowskian one $\eta_{\mu\nu}$ by a little quantity $h_{\mu\nu}$ so that

$$g_{\mu\nu} = \eta_{\mu\nu} + h_{\mu\nu} \ , \tag{1.8}$$

with $|h_{\mu\nu}| \ll 1$; using $\eta_{\mu\nu}$ to raise and lower all indexes and writing Ricci tensor and affine connection up to the first order in h, the Einstein field equations read

$$\Box h_{\mu\nu} - \frac{\partial}{\partial x^\lambda \partial x^\mu} h^\lambda{}_\nu - \frac{\partial^2}{\partial x^\lambda \partial x^\nu} h^\lambda{}_\mu + \frac{\partial}{\partial x^\mu \partial x^\nu} h^\lambda{}_\lambda = -16\pi G S_{\mu\nu} \ , \tag{1.9}$$

with

$$S_{\mu\nu} \doteqdot T_{\mu\nu} - \frac{1}{2}\eta_{\mu\nu} T^\lambda_{\ \lambda} \ . \tag{1.10}$$

Choosing the so called harmonic coordinate defined by the gauge

$$g^{\mu\nu}\Gamma^\lambda_{\mu\nu} = 0 \ , \tag{1.11}$$

that, to the first order in h corresponds to

$$\frac{\partial}{\partial x^\mu} h^\mu{}_\nu = \frac{1}{2}\frac{\partial}{\partial x^\nu} h^\mu{}_\mu \ , \tag{1.12}$$

the field equations now read

$$\Box h_{\mu\nu} = -16\pi G S_{\mu\nu} \tag{1.13}$$

leading to the *retarded potential* solutions:

$$h_{\mu\nu}(\vec{x}, t) = 4G \int d^3\vec{x}' \frac{S_{\mu\nu}(\vec{x}', t - |\vec{x} - \vec{x}'|)}{|\vec{x} - \vec{x}'|} \ . \tag{1.14}$$

This solution describes a gravitational radiation, produced by the source $S_{\mu\nu}$, that propagates with unit velocity, i.e. the velocity of light. As $r \rightarrow \infty$ the retarded wave approaches a plane wave of the form

$$h_{\mu\nu}(x) = e_{\mu\nu} e^{ik_\lambda x^\lambda} + c.c. \ , \tag{1.15}$$

satisfying

$$k_\mu k^\mu = 0 \ , \tag{1.16}$$

coming from (1.13) with $S^\mu{}_\nu = 0$, and

$$k_\mu e^\mu{}_\nu = \frac{1}{2} k_\nu e^\mu{}_\mu \ , \tag{1.17}$$

coming from (1.12). The symmetric matrix $e^\mu{}_\nu$ is the polarization tensor. For a monochromatic wave, propagating along the z axis (1.15) reduces to

$$h_{\mu\nu} = \begin{pmatrix} 0 & 0 & 0 & 0 \\ 0 & h_+ & h_\times & 0 \\ 0 & h_\times & -h_+ & 0 \\ 0 & 0 & 0 & 0 \end{pmatrix} e^{ik_\lambda x^\lambda} \ , \tag{1.18}$$

where it is evident that there are only two independent components usually called plus and cross polarization.

1.1.3 Effects on free-falling particles

What happens during the passage of a gravitational wave on the matter? If we consider a particle at rest in the coordinate frame of the harmonic gauge, using the geodesic equation it comes out that the particle is not subject to any acceleration. So we have to consider the relative motion of two particles and, consequently, we have to use the equation of geodesic deviation

$$\frac{d^2 n^\mu}{d\tau^2} - R^\mu{}_{\alpha\beta\gamma} \frac{dx^\alpha}{d\tau} \frac{dx^\beta}{d\tau} n^\gamma = 0 \ , \tag{1.19}$$

where n^μ is the vector connecting the two masses and x^μ the position of one of them. Considering only the first order in $h_{\mu\nu}$ and using the fact that the masses will move with a velocity much smaller than the speed of light, equation (1.19) brings to a solution

$$n^\mu(t) = n^\alpha(0)\Big(\delta_\alpha{}^\mu + \frac{1}{2}h_\alpha{}^\mu\Big) \,, \tag{1.20}$$

where we took the two particles at rest at $t = 0$. It is evident that the relative displacement of the two masses oscillates periodically with the same frequency of the overpassing gravitational wave. The effect is directly proportional to the distance of the particles and to the amplitude of the wave. In figure 1.1 the effect induced by a gravitational wave on a ring of particles is shown either for a plus polarization, or for a cross one.

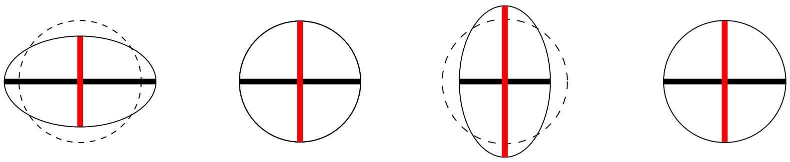

plus polarization

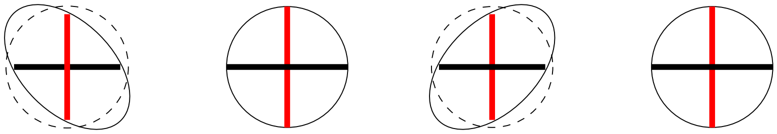

cross polarization

Figure 1.1: Effect on a ring of particles posed on the x-y plane due to the passage of a gravitational wave coming along z axis with a plus polarization or a cross polarization. It is shown that the effect on two chosen orthogonal directions is strongly depending on the polarization of the wave.

1.2 Generation

1.2.1 Radiation formula

From rather complicated tensor calculations, in the approximation of slow moving masses, it is possible to calculate the gravitational-wave power L expressed in terms of the reduced quadrupole moment of the source I_{jk}. The final result is

$$L = \frac{1}{5} \langle \dddot{I}_{jk} \dddot{I}_{jk} \rangle \ , \tag{1.21}$$

where the average is intended over several characteristic periods of the source system and I_{jk} is defined as

$$I_{jk} \doteqdot \int \rho \Big(x_i x_j - \frac{1}{3} \delta_{ij} r^2 \Big) d^3 x \ . \tag{1.22}$$

The gravitational wave radiation is a quadrupole radiation and so it is impossible for spherically or axially symmetric sources to emit anything.

1.2.2 Sources

There are essentially three kinds of gravitational wave sources: burst sources, periodic sources and stochastic sources.

Impulsive sources

These are sources that emit an impulsive signal in a very short time.

The main sources of this kind are supernovae, especially the supernovae of type II, that are exploding in a non axial-symmetric way. For such an event, called burst, at 10 kpc, the amplitude has been estimated to be of the order of 10^{-20} at hundreds or thousands of Hz. A detection can give information about explosion itself and also about the process of neutron-star and black-hole birth.

Compact binaries in their last instants before coalescence, are supposed to be impulsive sources too. For neutron-star neutron-star (NS-NS) binaries the signal is expected to be at a few thousand Hz with $h \sim 10^{-21}$ at 20 Mpc. Gravitational waves from NS-NS binaries carry important information about the equation of state of the NS, the physics of the emission and the distance from the source. If the binary is a black-hole black-hole (BH-BH) system the peak of emission, for a source in our galactic halo, is expected to be at about 500 Hz with $h \sim 10^{-18}$ [3, 4]. Unfortunately, at the present time, no systems of this kind are known.

For a very massive BH couple the gravitational wave emission moves down in frequency to 0.01 mHz, far from the sensitivity band of ground based interferometers and the signal cannot be considered impulsive anymore lasting even thousands of seconds.

Among the impulsive sources one should consider also the BH formation and the falling of matter on a massive BH. These events are expected to happen in the center of galaxies in a frequency band from 1 mHz to 10 mHz.

Periodic sources

These systems, for their intrinsic constitution, are emitting gravitational radiation at a well defined frequency for a consistent amount of time.

This is the case of compact binaries. The emission of gravitational waves from such a system has been proved in an indirect way measuring the decay of the revolution period of the two rotating stars [2]. In the first part of their rotation the signal is periodic and of low intensity ($h \sim 10^{-22}$). The final part of their rotation cannot be considered periodic anymore: we are in presence of the so called chirp, that is classified under the burst sources.

Another group of periodic sources comes from pulsars among which there are two kinds of candidates for gravitational waves emission: pulsars with a quadrupolar momentum, i.e. pulsars that are slightly asymmetric, emitting at a frequency that is twice the rotational one, and pulsars with no quadrupolar momentum, but rotating along an axis that is not the axis of symmetry; in this case the emission frequency is the rotational one. The amplitude for these signals is of the order of $10^{-27} \div 10^{-24}$.

Despite the little amplitude, these signals can overcome the detection background thanks to their periodicity, which permits a long integration time.

Stochastic sources

The origin of stochastic gravitational waves can simply be the summation over a large amount of bursts or periodic sources.

But during the evolution of the universe various phenomena originating stochastic signals could have taken place. This can be the case of the gravitational radiation as an echo of the moment in which the gravitational waves decoupled from the other elementary particles (this happened at about the Plank time from the beginning of the universe)[1].

Other sources could be related to the consequence of the eventual phase transitions occurred during the evolution of the universe. One can imagine exotic events like collisions of bubbles, collapses of cosmic strings or pressure fluctuations as a cause of stochastic gravitational waves in the frequency region below 1 mHz.

1.3 Detection

1.3.1 Resonant detectors

The first kind of gravitational wave detector developed in the last decades are the resonant bars. There are many experiments of this kind all over the world: the Italian AURIGA (Padova) [5], EXPLORER (CERN, Geneva) [6]

---

[1] If the inflation occurred this radiation should be replaced by the gravitational waves caused by quantum fluctuation.

and NAUTILUS (LNF, Rome) [7]; ALLEGRO (USA) [8].The detection system can be schematized as two masses m at a distance L interacting through a spring of elastic constant k. If a gravitational wave passes through the system, the masses start oscillating, modulating their distance. The bar detectors are long isolated cylinders — or spheres — made of a material with a low viscous coefficient and free to oscillate in the longitudinal direction. The role of the restoring force is played by the intrinsic elasticity of the material. The measurement of bar-length variations is done through capacitive transductors. The response of the system is the best at the resonance frequency of the bar, where the signal is maximally amplified. A gravitational signal at this frequency is also stored for a long time: for this reason bar detectors are considered systems with memory. The main limitation of this kind of detector is the narrow frequency-window in which the bar is highly sensitive. For frequencies out of the resonance band the signal induced on the bar is almost null. The sensitivity is limited by the thermal elastic vibration and by the noise of the transducers. For these reasons the detectors are made of low loss material and are cooled to cryogenic temperatures.

1.3.2 Interferometric detectors

A very promising technique to reveal gravitational waves involves the use of large Michelson-Morley interferometers. There are currently 4 experiments based on this idea: LIGO [9] (USA, with two 4 km long interferometers), VIRGO [10] (Italy and France, 3 km), GEO600 [11] (United Kingdom and Germany, 600 m), TAMA [12] (Japan, 300 m). The Michelson-Morley interferometer is a device that measures with high precision distance differences along two chosen directions using the time travel of photons. A laser beam passes through a beam splitter generating two twin beams each one traveling back and forth along an arm thanks to the reflection on end mirrors. The two beams recombine at the beam splitter and the signal is analyzed through a photo detector. If a gravitational wave propagating along z with a plus polarization passes through the interferometer that has its arms along the x and y directions, the proper distance ds^2 is given by

$$ds^2 = -c^2dt^2 + (1+h(t))dx^2 + (1-h(t))dy^2 + dz^2 \; . \tag{1.23}$$

For a ray propagating along the x direction, $dy = dz = 0$ and $ds^2 = 0$, so it follows

$$\frac{dx}{dt} = \pm \frac{c}{\sqrt{1+h(t)}} \; , \tag{1.24}$$

with the plus and minus signs referring to the two directions of propagation along the arm. The mirrors in the x and y directions can be considered as free falling, so, doing the calculation in the TT gauge, their position is constant in time. Assuming that the light enters the arm of length l_x at the time t_1 and arrives on the beam splitter at the time t_0, integrating equation (1.23), it follows

$$\int_{t_1}^{t_0} \frac{dt'}{\sqrt{1+h(t')}} = \frac{2l_x}{c} \; . \tag{1.25}$$

In the first term of the equation it is possible to use the approximation of $h \ll 1$,

$$\int_{t_1}^{t_0} \Big(1 - \frac{1}{2}h(t')\Big)dt' \simeq (t_0 - t_1) - \frac{1}{2}\int_{t_0-\frac{2l_x}{c}}^{t_0} h(t')dt' \; . \tag{1.26}$$

Calling Ω the angular frequency of the light, the round-trip phase $\phi_x(t)$ is

$$\phi_x(t) = \Omega t_1 = \Omega\Bigg(t_0 - \frac{2l_x}{c} - \frac{1}{2}\int_{t_0-\frac{2l_x}{c}}^{t_0} h(t')dt'\Bigg) \; . \tag{1.27}$$

From an analogous argument, considering the light traveling along the y axis,

$$\phi_y(t) = \Omega t_2 = \Omega\Bigg(t_0 - \frac{2l_y}{c} + \frac{1}{2}\int_{t_0-\frac{2l_y}{c}}^{t_0} h(t')dt'\Bigg) \; , \tag{1.28}$$

where t_2 is the entering time of the light in the y arm and l_y is its length. So, the phase difference of the two beams is:

$$\Delta\phi(t) \doteq \phi_x(t) - \phi_y(t) = \frac{2\Omega(l_x - l_y)}{c} - \Delta\phi_{\mathrm{GW}}(t) \; , \tag{1.29}$$

where

$$\Delta\phi_{\mathrm{GW}}(t) = \Omega \int_{t_0 - \frac{2l}{c}}^{t_0} h(t')dt' \tag{1.30}$$

and it has been used $l_x \simeq l_y = l$. The transfer function from the incoming gravitational wave to the phase change of the Michelson interferometer is then

$$H(\omega) = \frac{2\Omega}{\omega} \sin\left(\frac{l\omega}{c}\right) e^{-il\omega/c} \,, \tag{1.31}$$

revealing that there is an optimal length l_{opt} depending on the angular frequency ω_{GW} of the gravitational wave of interest

$$l_{\mathrm{opt}} = \frac{\pi c}{2\omega_{\mathrm{GW}}} = 250\,\mathrm{km}\left(\frac{300\ \mathrm{Hz}}{f}\right) \,. \tag{1.32}$$

Delay line and Fabry-Perot cavity

From the equation (1.32) it is evident that an experiment that aims to reveal gravitational waves at a few hundred Hz needs an interferometer with a few hundred km arms! There are problems of cost and construction that limits the length of the arms to few kilometers. But there are two methods to enhance the effective optical length: delay-lines and Fabry-Perot cavities. In the first case the light path is folded in the arms through a multiple reflection between the two faced mirrors. The actual path is $L = nl$ with l the length of the arm and n the number of reflections that occur in the arm before the light comes back to the beam splitter. Unfortunately there are great difficulties in constructing an arm with $n > 10$. Another drawback is in the response function of the arm: owing to the delay-line configuration, it presents a lot of zeros corresponding to the multiple reflections occurring to the beam. In the second case Michelson arms are two Fabry-Perot cavities. The parameter that defines the features of a Fabry-Perot cavity is the *finesse* F defined as the ratio between the distance of two resonant peaks and the width at half height of the resonant peak for the transmission coefficient:

$$F = \frac{\pi\sqrt{r_1 r_2}}{1 - r_1 r_2} \ , \tag{1.33}$$

where r_1 and r_2 are the reflection coefficients of the input and of the end mirror of the cavity. The effect of such a cavity is to "store" the light, simulating an enhancement of the optical path in the interferometer arms. It is possible to define a *storage time* $\tau_{\rm s}$ as the time required for the reflected light to decrease its power of a factor $1/e$ once the laser is turned off, that is

$$\tau_{\rm s} = \frac{L}{c}\frac{r_1}{1 - r_1} \simeq \frac{LF}{\pi c} \ . \tag{1.34}$$

A drawback of the Fabry-Perot cavity is that the heating of the laser on the mirrors starts to be relevant and can cause distortion of the surface. It is possible to calculate that the phase shift produced in the laser from a displacement variation δL between the two mirrors is

$$\left|\frac{\partial\phi}{\partial L}\right| = \frac{4r_1}{1 - r_1}k \ , \tag{1.35}$$

with k=$2\pi/\lambda$ and λ is the wave length of the laser light. For a displacement ΔL= $2Lh$ due to a gravitational wave, the power modulation at the output of the interferometer is

$$P_{\rm out} = P_{\rm in}\cos^2\left(\frac{4r_1}{1 - r_1}k\Delta L\right) = P_{\rm in}\cos^2\left(\frac{4r_1}{1 - r_1}2kLh\right) \ . \tag{1.36}$$

Comparing this equation with the one of a classic Michelson it is evident that the visible phase shift is amplified of a factor $\frac{4r_1}{1-r_1}$. To maximize the contrast[2], the working point for the interferometer is chosen by satisfying

$$k\Delta L = \frac{\pi}{2} + n\pi \ \ (n \in \mathbb{N}) \ \ \textit{“dark fringe”} \ , \tag{1.38}$$

---

[2] The contrast is defined as:

$$C = \frac{P_{\rm max} - P_{\rm min}}{P_{\rm max} + P_{\rm min}} \tag{1.37}$$

where $P_{\rm max}$ and $P_{\rm min}$ are the maximum and the minimum power read from the output photodiode when the signal phase changes from 0 to 2π.

but in this condition the sensitivity of the interferometer is at its minimum:

$$P_{\mathrm{out}} = P_{\mathrm{in}} \cos^2(k\Delta L) = 0 \;\; \text{and} \;\; \frac{\partial P_{\mathrm{out}}}{\partial \Delta L} = 0 \; . \tag{1.39}$$

To avoid this situation a heterodyne phase modulation is used: through a small asymmetry in the length of the two arms it permits to have $\frac{\partial P_{\mathrm{out}}}{\partial \Delta L} \neq 0$. As for the detection a technique that goes under the name of *Pound-Drever* technique is implemented. The phase of the incoming light in the interferometer is modulated through a Pockel-cell, an electro-optic transducer whose refraction index varies proportionally to the potential ΔV. This technique allows to isolate the gravitational signal from any kind of noise external to the interferometric cavity, translating the information in higher frequency regions (usually radio frequency). The acquired signal is non-null only in presence of real variation of the optical path of the light due to gravitational signal or real displacement of the optic elements. For this reason this kind of detectors are referred to as “null instruments”.

Chapter 2

Noise sources in interferometric detector

In this chapter the main important noise-sources limiting the sensitivity of a gravitational wave interferometer will be discussed in the frequency band of interest. Throughout this thesis the strain sensitivity h will be used, defined as $h = \frac{2}{L}\sqrt{S_X}$ (in units $1/\sqrt{\mathrm{Hz}}$), where S_X is the displacement power spectrum of the quantity considered and L is the length of one interferometer arm.

2.1 Optical read-out noises

2.1.1 Shot noise

In the previous chapter it was explained that the detection of gravitational waves with interferometers is possible through the measurement of the power variation at the output port. This corresponds to the count of the number of photons that arrive at the photo-diode in the unit of time, because

$$P_{\mathrm{out}} = \overline{n}\frac{\hbar c}{\lambda} \ , \tag{2.1}$$

with $\overline{n}$ medium number of photons coming on the photo-diode in the unit of time, $\hbar$ Planck's constant, c velocity of light and λ wave length of the laser. Such a counting is governed by the Poisson statistic; the fluctuation $\sigma_{\overline{n}}$ of the mean number is

$$\frac{\sigma_{\overline{n}}}{\overline{n}} = \frac{1}{\sqrt{\overline{n}}} \, . \tag{2.2}$$

For a Michelson interferometer, in the working point in which $P_{\rm out}= P_{\rm in}/2$, this happens to be a simulated variation of the arm-length difference [15]

$$\delta \Delta L = \frac{\sigma_{\overline{n}}}{\overline{n}} P_{\rm out} \left(\frac{dP_{\rm out}}{d\Delta L} \right)^{-1} = \sqrt{\frac{\hbar c \lambda}{4\pi P_{\rm in} \tau}} \, , \tag{2.3}$$

where τ is the observation time interval. This phenomenon is called *shot noise* and, for a Fabry-Perot interferometer in the dark fringe working point, it takes the following form [16]:

$$\delta \tilde{h}_{\rm Shot}(f) = \frac{\chi}{8LF} \sqrt{\frac{4\pi c \hbar \lambda}{\eta C P_{\rm in}}} \sqrt{1 + \left(\frac{f}{f_{\rm FP}} \right)^2} \, , \tag{2.4}$$

where $\delta h_{\rm Shot}$ is the strain sensitivity contribution due to the shot noise, $f_{\rm FP}= \frac{c\pi}{2LF}$ is the frequency corresponding to the characteristic wave length of the Fabry-Perot cavity of finesse F, C is the recycling factor, η is the quantum-efficiency of the output photo-diode and χ is a corrective factor taking into account the modulation[1].

The presence of a recycling factor C is due the positioning of a *recycling mirror*, between the mode cleaner and the beam splitter (refer to figure 2.1 on page 26). Since the interferometer is close to a null in the interference pattern, nearly all of the light supplied would be reflected back towards the laser; in other words the laser would not be properly impedance matched to the interferometer. The recycling mirror, with a correctly chosen transmission, improves the impedance matching allowing to reach the kilovolts needed on the beam splitter from the tens of volts coming from the laser.

---

[1] Bondu estimated [17] that for Virgo $\chi = \sqrt{3/2}$.

For high and low frequency regions w.r.t. f_{FP} the shot noise reduces to:

$$\delta\tilde{h}_{\mathrm{Shot}}(f) = \begin{cases} \dfrac{\chi}{8LF}\sqrt{\dfrac{4\pi c\hbar\lambda}{\eta C P_{\mathrm{in}}}} \propto \dfrac{1}{F\sqrt{CP_{\mathrm{in}}}} \,, & \text{for } f \ll f_{\mathrm{FP}} \,, \\ \dfrac{\chi f}{2}\sqrt{\dfrac{4\pi\hbar\lambda}{c\eta C P_{\mathrm{in}}}} \propto \dfrac{f}{\sqrt{CP_{\mathrm{in}}}} \,, & \text{for } f \gg f_{\mathrm{FP}} \,, \end{cases} \tag{2.5}$$

showing, for low frequency, a constant behavior followed, over the Fabry-Perot frequency, by a slope proportional to the frequency. Therefore this noise is the dominant one at high frequencies. It is evident that going at high finesse and power laser on the beam splitter (high CP_{in}) can be a solution to limit this noise. But there are technical limitations that put constraints on F and C. In fact introducing the optical loss l and the transmittance of the inner mirror t one has:

$$F \leqslant \frac{2\pi}{t+2l} \tag{2.6}$$

and

$$C \leqslant \frac{1}{2n_{\mathrm{eff}}l + l_{\mathrm{BS}}} \,, \tag{2.7}$$

where n_{eff} is the effective number of bounces of the laser in the Fabry-Perot cavity ($n_{\mathrm{eff}} = 2F/\pi$) and l_{BS} is the loss of the beam splitter.

2.1.2 Radiation pressure noise

The mirror is pushed by the back-action of the reflected photons, whose number is fluctuating according to the photon statistics. The radiation pressure noise is the noise related to this uncertainty of the mirror position on a macroscopic scale. In the case of a Fabry-Perot cavity, the radiation pressure induced displacement is [18]

$$\delta\tilde{h}_{\mathrm{Rad}} = \frac{F}{mL\pi^2 f^2}\sqrt{\frac{\hbar C P_{\mathrm{in}}}{\pi c\lambda}}\frac{1}{\sqrt{1+(f/f_{\mathrm{FP}})^2}} \,. \tag{2.8}$$

For high and low frequency regions w.r.t. f_{FP} the radiation pressure noise reduces to

$$\delta\tilde{h}_{\mathrm{Rad}}(f) = \begin{cases} \dfrac{F}{mL\pi^2 f^2}\sqrt{\dfrac{\hbar C P_{\mathrm{in}}}{\pi c\lambda}} \propto \dfrac{F\sqrt{CP_{\mathrm{in}}}}{f^2} \ , & \text{for } f \ll f_{\mathrm{FP}} \ , \\ \dfrac{1}{4mL^2\pi^2 f^3}\sqrt{\dfrac{c\hbar C P_{\mathrm{in}}}{\pi\lambda}} \propto \dfrac{\sqrt{CP_{\mathrm{in}}}}{f^3} \ , & \text{for } f \gg f_{\mathrm{FP}} \ , \end{cases} \tag{2.9}$$

showing a f^{-2} behavior at low frequencies, followed by a slope proportional to f^{-3} over the Fabry-Perot frequency. It is evident that this noise dominates at low frequencies and that can be limited decreasing the finesse and the power on the beam splitter (CP_{in}). Unfortunately this is a requirement that is opposite to the one found for the shot noise reduction.

Actually, shot noise and radiation pressure noise are strongly related through a quantum-mechanical relation: the quantum noise $\delta h_{\mathrm{Quant}}$ satisfies

$$\delta\tilde{h}^2_{\mathrm{Quant}} \doteqdot \delta\tilde{h}^2_{\mathrm{Shot}} + \delta\tilde{h}^2_{\mathrm{Rad}} \geqslant 2\sqrt{\delta\tilde{h}^2_{\mathrm{Shot}}\delta\tilde{h}^2_{\mathrm{Rad}}} = 2\delta\tilde{h}_{\mathrm{Shot}}\delta\tilde{h}_{\mathrm{Rad}} \ . \tag{2.10}$$

This is an obvious consequence, being the interferometer a Heisenberg microscope. The equality is verified when $\delta\tilde{h}_{\mathrm{Shot}} = \delta\tilde{h}_{\mathrm{Rad}}$ and in this case the quantum noise is called Standard Quantum Limit (SQL) and it is

$$\delta\tilde{h}_{\mathrm{SQL}} = \frac{1}{L\pi f}\sqrt{\frac{2\hbar}{m\sqrt{\eta}}} \ . \tag{2.11}$$

The SQL represents an intrinsic limit for the sensitivity of an interferometer and can be overpassed in a limited frequency band (obviously losing information in other bands) using new techniques like the signal recycling [13] or the light squeezing [14].

2.2 Thermal noise

Thermal noise constitutes the most important noise source in the band from some dozen Hz to many hundred Hz. It represents the fluctuation of a macroscopic observable of the system at the thermodynamic equilibrium with the ambient, due to the thermal agitation of the microscopic elements constituting it. For this reason this noise comes out to be an unavoidable limit for the precision of many measurements. In the interferometers this noise enters the sensitivity in the following ways:

- suspension thermal noise, which is responsible for displacement of the mirrors center of mass. It has three different sources:
  - pendulum mode thermal oscillation,
  - vertical mode thermal oscillation,
  - violin modes thermal oscillation;
- mirror thermal noise (in the bulk and in the coating), which can be divided into:
  - Brownian thermal noise,
  - thermoelastic noise,
  - thermorefractive noise.

All these noise sources will be examined in detail in chapter 4.

2.3 Environmental noises

2.3.1 Seismic noise

Seismic noise is the main source of noise at low frequency (below 100 Hz). In this band it is mainly due to human or geologic activity. Typically the spectral amplitude has the form [23]

$$\tilde{x}_{\mathrm{Seism}}(f) \approx 10^{-7} \left(\frac{1\,\mathrm{Hz}}{f} \right)^2 \frac{\mathrm{m}^2}{\mathrm{Hz}} \,, \quad \text{for } \; f > 0.01\,\mathrm{Hz}. \tag{2.12}$$

The damping of the seismic noise is obtained through the use of a mechanical oscillator. The transfer function $H(f)$ of an oscillator of mass m, elastic constant k, under a viscous damping b is

$$H(f) = \frac{f_0^2}{f_0 - f^2 + if\frac{b}{2\pi m}} \; , \tag{2.13}$$

where $f_0 = \frac{1}{2\pi}\sqrt{\frac{k}{m}}$. At frequency f greater than the resonance

$$H(f) \approx \frac{f_0^2}{f^2} \; , \;\; \text{for} \;\; f \gg f_0 \; , \tag{2.14}$$

that is, the oscillator acts as a filter for frequencies over the resonance frequency. By the way, at the resonance an input signal is amplified of a factor $Q = 2\pi m f_0/b$. So it is important for the system to be highly dissipative, i.e. with a very low Q.

2.3.2 Gravity gradient noise

The Gravity gradient noise, also known as Newtonian noise, is the noise due to the change in the gravitational attraction felt by the mirrors of the interferometer. Variations in the position of masses in the vicinity of the mirrors or in the ground or atmosphere density around the mirrors generate a differential gravitational force that acts directly on the mirrors, bypassing all the isolation systems. Obviously the interferometers are built in areas far away from human activity — car, truck or train passages —; on the other hand the atmospheric Newtonian noise is estimated to be well below the sensitivity of the interferometers of this generation. The main important contribution to the Newtonian noise is so due to the ground movements induced by surface waves from the seismic activity.

Different models were done to estimate gravity gradient noise [19, 20], all presenting similar behaviors. The most important variable that enters the calculation is the local seismic activity model. According to Saulson's model [19]:

$$\delta\tilde{h}_{\mathrm{GG}}^{\mathrm{Saul}} = \beta\frac{2G\rho}{\pi L}\frac{\tilde{x}_{\mathrm{Seism}}}{f^2} \tag{2.15}$$

where ρ is the density of the ground around the mirror, $\tilde{x}_{\mathrm{Seism}}$ is the power spectrum density of the seismic noise and β is an order-of-unity parameter that takes into account the seismic noise level for the particular moment under consideration. In the next-generation interferometers, with the increased sensitivity gravity gradient noise should be relevant in the interesting band around 10 Hz. At the moment there are studies to limit this noise through the construction of underground interferometers, with elliptical caves to displace the mirrors in, to mainly annihilate also the effect of the seismic compression wave propagating parallel to earth surface.

2.3.3 Residual gas noise

The gas molecules along the optical path affect the sensitivity of the interferometer through their refraction-index fluctuation. The effect is estimated to be [15]

$$\delta\tilde{h}_{\mathrm{Gas}} = \frac{2}{L}\sqrt{\frac{V_0}{N_A}\frac{(n-1)^2}{2\pi u_0}\sqrt{\frac{L}{\lambda}}\left(\frac{p}{p_0}\right)\left(\frac{T_0}{T}\right)^{\frac{3}{2}}}\,, \tag{2.16}$$

where n is the refractive index of the gas, V_0 is the volume of one gas mole at the standard temperature T_0, N_A is the Avogadro's number, u_0 is the mean velocity of the gas molecules at the standard state and p and p_0 are the pressures at the temperature T and at the standard state respectively. The typical required vacuum level for a kilometer class detector is $\sim 10^{-6}\,\mathrm{Pa}$. In most of the constructed pipes there is a pressure of $\sim 10^{-8}\,\mathrm{Pa}$, taking a good safety margin.

2.4 Other noises

There are also other noise sources depending on the characteristics of the laser, on the readout electronics and on the vacuum apparatus.

2.4.1 Laser frequency noise

In a single Fabry-Perot cavity the spectral frequency noise $\delta\tilde{\nu}$ of the laser light directly couples to the spectral displacement noise $\delta\tilde{L}$ through a simple relation:

$$\delta\tilde{L} = L\frac{\delta\tilde{\nu}}{\nu} \ , \tag{2.17}$$

where L is the optical length of the cavity and ν is the frequency of the light; thus with a shorter cavity the effect is less important. In the Fabry-Perot Michelson interferometer, the frequency noise is subtracted optically at the interference of the detection port and it appears as a signal through the asymmetry ΔL of the two arms:

$$\delta\tilde{h}_{\mathrm{Freq}} = 2\frac{\delta\tilde{\nu}}{\nu}\frac{\Delta L}{L} \ . \tag{2.18}$$

2.4.2 Laser intensity noise

In a single Fabry-Perot cavity a laser intensity fluctuation in input is seen as a displacement noise at the output and the locking of the cavity will compensate for it as if it were a gravitational wave signal. In the case of a Fabry-Perot Michelson interferometer this effect almost cancels out; it remains because of a coupling with the residual displacement x_{RMS} of the mirrors around the resonance of the cavity, giving a strain equivalent noise δh_{Int}:

$$\delta\tilde{h}_{\mathrm{Int}} = \frac{2}{L}\frac{\delta\tilde{P}}{P}x_{\mathrm{RMS}} \tag{2.19}$$

where P is the power and $\delta\tilde{P}$ is the spectral power fluctuation.

2.4.3 Thermal lensing

If the power circulating in the cavities is increased in order to lower the shot noise, as planned for future interferometers, a static distortion of the mirror (thermal lensing) appears. This distortion must be corrected by using some thermal compensation through auxiliary laser, as in LIGO, or through peripheral heated devices on the mirrors, as in GEO600. This noise can be huge, depending on the finesse asymmetry [23].

2.4.4 Electric noise

The mirror position is changed by the seismic motion, especially at the resonance of the isolation system; for this reason the Fabry-Perot cavity length has to be controlled and kept at its resonance through a feed-back force acting on the mirror. The servo circuit and the actuator circuit for this control can disturb the mirror position. On the one hand the servo circuit is designed to have a sufficient gain for stable operation and suppression of the other noises, but on the other also a high gain can introduce noise. Thus the design of the servo-loop comes from a balance between a high gain and a low introduced noise. Similarly the actuators should have enough dynamic range and a sufficiently strong coupling. The actuator-circuit noise is typically of the order of few $\mathrm{nV}/\sqrt{\mathrm{Hz}}$ so, in order to make the actuator noise smaller than the goal sensitivity, the uncontrolled motion of the mirror has to be damped as much as possible using passive isolation or various active control at different stages.

2.4.5 Scattered light

It can happen that photons of the beam are scattered by mirror imperfections and bounce on the pipe walls getting different phases. If they recombine with the laser beam a phase noise arises. To avoid this problem a set of mechanical filters made by absorbing steel are usually placed along the pipe [21].

2.5 An example: the Virgo interferometer

It is interesting to see how the various noise levels discussed above reflect on the sensitivity of an actual interferometer like the Virgo one, constructed during the last years by a French-Italian collaboration in Cascina, near Pisa.

2.5.1 A Virgo overview

It will be helpful to have an overview of the whole interferometer with the scheme showed in figure 2.1. The main important technical features of the Virgo interferometer are discussed in the following.

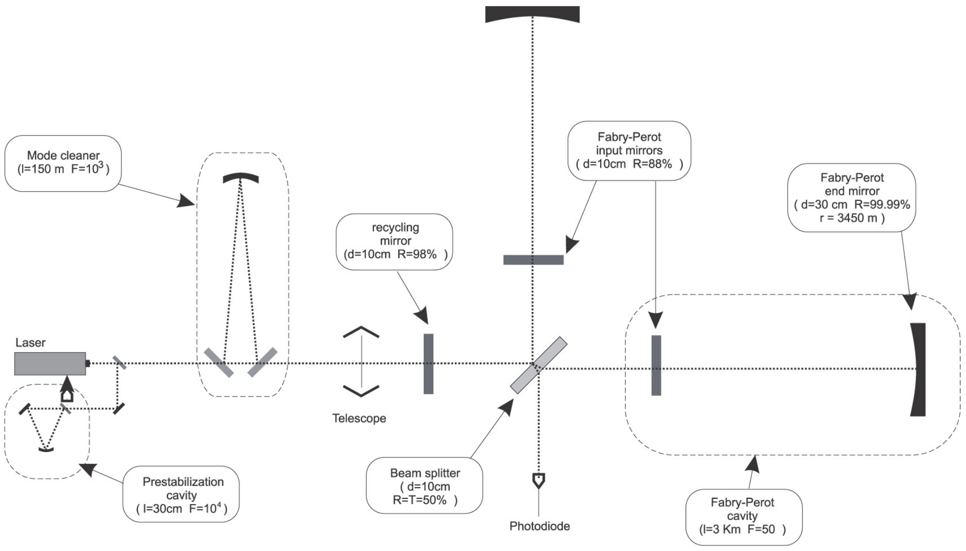

Figure 2.1: A schematic representation of the Virgo optical scheme.

- **Suspension system.** Virgo has developed a suspension system called *superattenuator* [22] for suppressing the seismic noise transmission to the mirror above 5÷10 Hz. This is a peculiar feature of this interferometer w.r.t. the ones of the other gravitational wave experiments. The superattenuator is essentially a multi-stage pendulum about 10 m tall, where each suspended mass is a special device acting as a vibration low-pass filter in each of the 6 degrees of freedom. A scheme of a superattenuator is shown in figure 2.2.

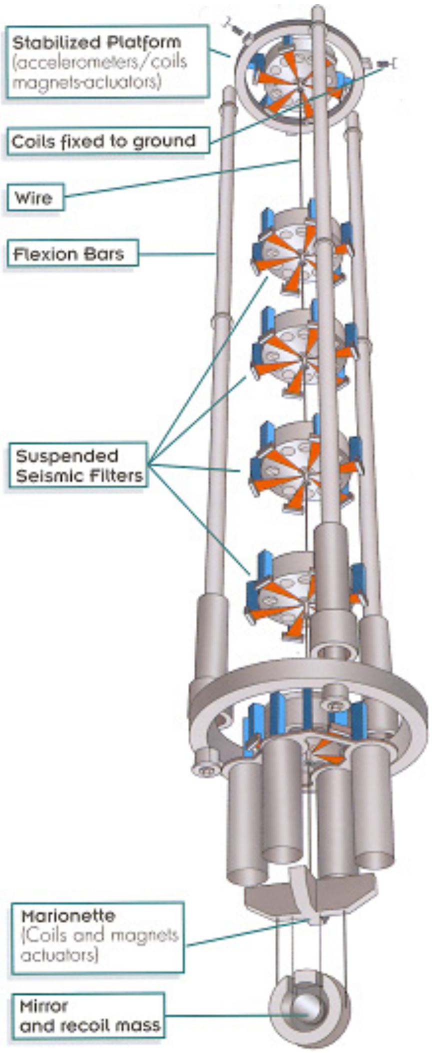

Figure 2.2: A schematic representation of the Virgo superattenuator. A chain of 5 filters (with a horizontal resonant frequency $f_h = 0.45$ Hz and a vertical one $f_v = 0.4$ Hz) is attached to the top of a big tripod, that acts as an inverted pendulum (with $f_h = 30$ mHz). The mirror is hanged through a device called *marionetta* that allows a fine control of its position along the three relevant degrees of freedom.

Shorter suspensions are used for the input bench, the mode cleaner and the detection bench.

- **Laser.** It is a Nd:YVO_4 emitting at $\lambda = 1064$ nm. Its output, in the TEM_{00} mode, is about 20 W and its stability requirements (derived from (2.18) and (2.19) assuming the measured x_{RMS} of the residual movements of the mirror) are:
  - in power:
    $$\frac{\delta\tilde{P}}{P} < \begin{cases} 3\times 10^{-5}/\sqrt{\mathrm{Hz}}\ , & \text{for } f = 10\ \mathrm{Hz}\ , \\ 3\times 10^{-7}/\sqrt{\mathrm{Hz}}\ , & \text{for } 100 < f < 1\ \mathrm{kHz}\ ; \end{cases} \tag{2.20}$$
  - in frequency:
    $$\frac{\delta\tilde{\nu}}{\nu} \simeq \begin{cases} 10^{-4}/\sqrt{\mathrm{Hz}}\ , & \text{for } f = 10\ \mathrm{Hz}\ , \\ 10^{-6}/\sqrt{\mathrm{Hz}}\ , & \text{for } 100 < f < 1\ \mathrm{kHz}\ . \end{cases} \tag{2.21}$$

  The laser, its stabilization apparatus and the phase modulator are not under vacuum and they are placed on an optical table in a clean room.

- **Input bench.** It is under vacuum and it holds the triangular reference cavity for the laser frequency pre-stabilization, the input and the output mirrors of the mode cleaner and the main beam expansion and alignment optotronics.

- **Mode cleaner.** It is a triangular 144 m long cavity with the middle mirror suspended to a short superattenuator and connected with the two other mirrors by a dedicated pipe.

- **Power recycling.** The recycling cavity is made by an additional suspended mirror and the interferometer itself. The recycling factor is about 50 and a power of about 1 kW goes on the beam splitter.

- **Fabry-Perot cavities.** Four fused silica mirrors (35 cm in diameter and 9.6 cm thick) form two 3 km long Fabry-Perot cavities with a finesse F=50. Input mirrors are made of Suprasil with a coating (10 cm in diameter, 2.25 μm thick) made of 12 alternating layers of SiO_2 and Ta_2O_5; end mirrors are made of Herasil with a coating (28 cm in diameter, 5.45 μm thick) made of 35 alternating layers of the same materials. The optical requirements on the end mirrors are reported in table 2.1.

Property	Value	Units
reflectivity	0.99995	—
roughness	10	nm
coating loss	< 5	ppm
bulk loss	< 0.7	ppm/cm

Table 2.1: Optical properties required for end mirrors.

- **Detection system.** It is composed of a detection bench holding the output mode cleaner and an optical table outside the vacuum vessel holding the photodiodes (with a quantum efficiency $\eta = 0.85$).

- **Vacuum system.** The vacuum vessel is composed of two parts: the pipes (containing the optics) and the towers (containing the superattenuators). The pipes are 1.2 m in diameter and have a partial pressure of 10^{-9} mbar for hydrogen, 10^{-14} mbar for hydrocarbons[2] and 10^{-10} mbar for other gases. The ultra-high vacuum required in the pipe cannot be achieved in the towers because of the devices outgassing; thus the towers are divided into two parts by a roof with a little hole for allowing the passage of the wire holding the last stage of the suspension.

---

[2] The limit on hydrocarbons is more stringent because of the capability they have to stick on the mirror surfaces degrading their quality.

2.5.2 Virgo sensitivity curve

In figure 2.3 the main important noise contributions for the Virgo interferometer are shown [23]. The sum of them, expressed in unit of strain (defined at the beginning of this chapter), is the so called sensitivity curve. It is evident that there are four frequency intervals characterized by a dominating noise source over the others:

- **Seismic wall.** Below 4÷5 Hz the seismic noise cannot be sufficiently filtered by the superattenuators (see figure 2.2) and rapidly grows, roughly with f^{-11}.
- **Pendulum thermal noise.** It dominates approximately between 5 and 40 Hz and it goes as $f^{-5/2}$ (see § 4.3).
- **Mirror thermal noise.** It is the dominant noise in the range 40÷500 Hz and it goes as $f^{-1/2}$ (see § 4.1).
- **Shot noise.** Above 500 Hz it dominates increasing proportionally to the frequency (see § 2.1.1).

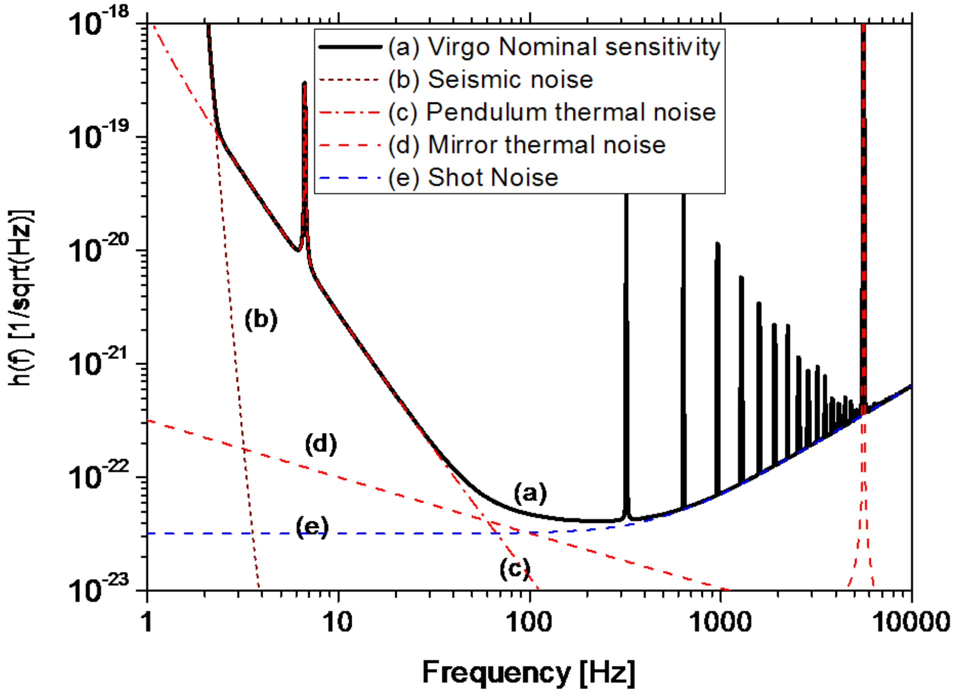

Figure 2.3: Virgo sensitivity curve.

Chapter 3

Theory of thermal noise

In this chapter a theoretical background for the comprehension and calculation of the thermal noise is given through the fluctuation-dissipation theorem. The quality factor and the loss angle are introduced as essential quantities in the characterization of the dissipative behavior of the materials. The basic estimation methods of thermal noise are introduced and the evaluation of the relevant thermal noise for interferometric gravitational wave detectors is discussed.

3.1 The fluctuation-dissipation theorem

It is known that systems, left free to evolve in thermodynamical equilibrium at a temperature T, show a fluctuation in the variables describing them. An example is the Brownian motion of particles suspended in water [24]. The particles follow complex trajectories that can be seen as fluctuations of the position variable; the origin of this behavior resides in the collision processes between them and the water molecules. The momentum transfer depends on the velocity distribution of the molecules and therefore on the temperature of the bath.

The same collisions are at the base of another process: the viscous damping. A particle, moving in a fluid loses momentum by collisions with the other molecules, until it dissipates all its non-thermal kinetic energy. The above examples show that it exists a relationship between the physical processes responsible for the dissipation and fluctuation: they are originated from the same mechanism. Having a tight link with the equilibrium temperature of the system, the fluctuation takes the name of *thermal noise*.

The comprehension of the link between irreversible processes and fluctuation allows to find quantitatively the power spectrum of the thermal noise once the nature of the irreversibility is known. This result had been obtained in a general way by Callen and Welton that stated it in the so called Fluctuation-Dissipation Theorem (FDT) [25, 26, 27, 28]. Consider a linear[1] and dissipative[2] system in thermodynamical equilibrium. Let $F(t)$ be an external solicitation and $\dot{X}(t)$ the response of the system derived from the equation of motion. In order to introduce the generalized force into this equation of motion, the new term

$$H_{\text{int}} = -F(t)X(t) \tag{3.1}$$

is added to the Hamiltonian of the system. The information of the dissipation of the system is embedded in the *impedance* function $Z(\omega)$, defined as

$$Z(\omega) \doteqdot \frac{\widetilde{F}(\omega)}{\widetilde{\dot{X}}(\omega)} , \tag{3.2}$$

where the tilde stands for the Fourier transform. It is also useful to define the admittance as

$$Y(\omega) \doteqdot \frac{1}{Z(\omega)} \tag{3.3}$$

and the transfer function as

$$H(\omega) \doteqdot \frac{\widetilde{X}(\omega)}{\widetilde{F}(\omega)} = \frac{1}{i\omega Z(\omega)} = \frac{Y(\omega)}{i\omega} . \tag{3.4}$$

---

[1] The linearity states that the dissipated power is quadratical w.r.t. the amplitude of the solicitation.

[2] A system is considered dissipative if, under an external solicitation, it absorbs energy through irreversible processes.

The FDT states that the power spectrum of the thermal noise for the quantity X is

$$S_X(\omega) = \frac{4k_BT}{\omega^2}\mathcal{R}e[Y(\omega)] \tag{3.5}$$

or, using (3.2) and (3.3), that the power spectrum of F is

$$S_F(\omega) = 4k_BT\mathcal{R}e[Z(\omega)] \ , \tag{3.6}$$

where k_B is the Boltzmann's constant and T is the temperature of the system. Integrating the spectrum of (3.5) over frequency, one gets $k_BT/2$ as it should be from the equipartition theorem.

As an example it can be considered a resistor in an electric circuit. Calling R the impedance of the resistor, the voltage V plays the role of F, the charge the role of X and, from (3.5), it follows that the power spectral noise of the tension is

$$V^2(\omega) = 4k_BTR(\omega) \ , \tag{3.7}$$

that is the well known Johnson-Nyquist formula [29].

3.1.1 FDT in an n-dimensional system

The previous discussion can be extended to a system which has n coordinates X_i. The interaction between the system and the world can be represented by the generalized forces F_i introducing the new term

$$H_{\text{int}} = -F_i(t)X_i(t) \tag{3.8}$$

in the Hamiltonian of the system. In this case the equation (3.2) becomes

$$\widetilde{F}_i(\omega) = Z_{ij}(\omega)\widetilde{\dot{X}}_j(\omega) \ , \tag{3.9}$$

where now the impedance Z_{ij} is a matrix. Defining the admittance as the inverse matrix of the impedance

$$Y_{ij} \doteqdot Z_{ij}^{-1} \ , \tag{3.10}$$

the FDT in the form of the equation (3.5) is now written as

$$S_{X_iX_j}(\omega) = \frac{4k_BT}{\omega^2}\mathcal{R}e[Y_{ij}] \ , \tag{3.11}$$

where $S_{X_iX_j}$ is the cross spectrum density, i.e. the Fourier transform of the cross correlation function between X_i and X_j; the cross spectrum for $i=j$ is identical to the power spectrum density of X_i. Equation (3.6) becomes

$$S_{F_iF_j}(\omega) = 4k_BT\mathcal{R}e[Z_{ij}(\omega)] \ , \tag{3.12}$$

where $S_{F_iF_j}$ is the cross spectrum density between F_i and F_j.

3.1.2 FDT for a linear combination of coordinates

In many practical situations it is necessary to evaluate the behavior of a coordinate that is not a natural mode of the system but is easily measurable. This can be the case of the surface of a mirror as seen by a laser beam profile. A new coordinate X_{new} of the n-dimensional system can be defined as

$$X_{\text{new}} = P_iX_i \ , \tag{3.13}$$

where P_i are arbitrary real constants. In this paragraph it is shown that the power spectrum of X_{new} can be derived using the FDT with no particular effort, obtaining a formula of the same kind of (3.5), also in the case of a continuous combination of coordinates. To allow the presence of a force F_{new} that drives only the momentum conjugate to X_{new} the term to add in the interaction Hamiltonian shall be of the form

$$H_{\text{int}} = -F_{\text{new}}X_{\text{new}} = -F_{\text{new}}P_iX_i = -(P_iF_{\text{new}})X_i \tag{3.14}$$

and, comparing this equation with (3.8), it is evident that the Hamiltonian of the interaction of the 1-dimensional system described by X_{new} can be reinterpreted as a Hamiltonian of a n-dimensional system where $P_i F_{\mathrm{new}}$ plays the role of F_i; so, from the definition of Y_{ij},

$$\widetilde{\dot{X}}_i = Y_{ij} \widetilde{F}_j = Y_{ij} P_j \widetilde{F}_{\mathrm{new}} \ . \tag{3.15}$$

It is straightforward to define the admittance Y_{new} of the system w.r.t. the new coordinate as

$$Y_{\mathrm{new}} \doteqdot \frac{\widetilde{\dot{X}}_{\mathrm{new}}}{\widetilde{F}_{\mathrm{new}}} = \frac{P_i \widetilde{\dot{X}}_i}{\widetilde{F}_{\mathrm{new}}} = \frac{P_i Y_{ij} P_j \widetilde{F}_{\mathrm{new}}}{\widetilde{F}_{\mathrm{new}}} = P_i P_j Y_{ij} \ , \tag{3.16}$$

where equations (3.13) and (3.15) were used. From equations (3.11) and (3.13) it is possible to calculate the power spectrum density $S_{X_{\mathrm{new}}}$ of the new coordinate X_{new},

$$S_{X_{\mathrm{new}}}(\omega) = P_i P_j S_{X_i X_j}(\omega) = \frac{4 k_B T}{\omega^2} \mathcal{R}e[P_i P_j Y_{ij}(\omega)] \tag{3.17}$$

and, using equation (3.16),

$$S_{X_{\mathrm{new}}}(\omega) = \frac{4 k_B T}{\omega^2} \mathcal{R}e[Y_{\mathrm{new}}(\omega)] \ , \tag{3.18}$$

that has the same form of equation (3.5) for the thermal noise of a 1-d system. In a similar manner it is possible to derive the power spectrum of the force fluctuation

$$S_{F_{\mathrm{new}}}(\omega) = 4 k_B T \mathcal{R}e[Z_{\mathrm{new}}(\omega)] \ , \tag{3.19}$$

where $Z_{\mathrm{new}} \doteqdot \widetilde{F}_{\mathrm{new}} / \widetilde{\dot{X}}_{\mathrm{new}}$.

If X is a function of a continuous parameter r, i.e.

$$X_{\mathrm{new}} = \int P(\boldsymbol{r}) X(\boldsymbol{r}) d^3 r \ , \tag{3.20}$$

all the previous calculations are still valid: the Hamiltonian of the interaction is rewritten as

$$H_{\mathrm{int}} = - \int F_{\mathrm{new}} P(\boldsymbol{r}) X(\boldsymbol{r}) d^3 r \tag{3.21}$$

and, comparing with the Hamiltonian of a generic system with a continuous set of coordinates

$$H_{\mathrm{int}} = -\int F(\boldsymbol{r})X(\boldsymbol{r})d^3r \ , \tag{3.22}$$

it is evident that $F_{\mathrm{new}}P(\boldsymbol{r})$ plays the role of $F(\boldsymbol{r})$, so

$$\widetilde{\dot{X}}(\boldsymbol{r}') = \int Y(\boldsymbol{r},\boldsymbol{r}')\widetilde{F}(\boldsymbol{r}) = \int Y(\boldsymbol{r},\boldsymbol{r}')P(\boldsymbol{r}')\widetilde{F}_{\mathrm{new}}(\boldsymbol{r}) \tag{3.23}$$

and equation (3.16) becomes

$$Y_{\mathrm{new}} \doteqdot \frac{\widetilde{\dot{X}}_{\mathrm{new}}}{\widetilde{F}_{\mathrm{new}}} = \frac{\int P(\boldsymbol{r}')\widetilde{\dot{X}}(\boldsymbol{r}')d^3r'}{\widetilde{F}_{\mathrm{new}}} = \int P(\boldsymbol{r}')P(\boldsymbol{r}'')Y(\boldsymbol{r}',\boldsymbol{r}'')d^3r'd^3r'' \ . \tag{3.24}$$

Therefore the spectrum of the thermal fluctuation is still equation (3.18), with Y_{new} given by (3.24).

3.1.3 The harmonic oscillator and the loss angle

The equation of motion of a harmonic oscillator of mass m is

$$m\ddot{x} + m\omega_0^2 x = F(t) \ , \tag{3.25}$$

where $F(t)$ is the force acting on the mass and ω_0 is the resonance of the system. Passing in the frequency domain, the transfer function $H(\omega)$ defined in (3.4) results to be

$$H(\omega) = \frac{1}{m(\omega_0^2 - \omega^2)} \ . \tag{3.26}$$

There is no dissipation involved and the response of the system diverges when $\omega = \omega_0$.

In a real system the elastic response to the external force $F(t)$ is not immediate and the elongation x is shifted in time w.r.t. the forcing term, causing a deviation from the Hooke's law that is called *anelasticity*. The effect of this anelasticity is that a dissipation and a damping can occur, so that the resonance peak becomes finite. To introduce the anelasticity in the model of the harmonic oscillator Hooke's law is generalized. Hooke's law says that the stress σ needed to produce a relative displacement ϵ is proportional to the latter through a constant E, called Young's modulus. A possible extension of this law to the anelastic case is to assume that the proportionality constant can be a complex number and can depend on frequency:

$$\sigma(\omega) = E(\omega)\epsilon(\omega) \ , \tag{3.27}$$

where the coefficient $E(\omega)$ can be written as

$$E(\omega) = E_1(\omega) + iE_2(\omega) = |E|e^{i\phi(\omega)} \ . \tag{3.28}$$

The phase angle ϕ takes the name of *loss angle*. If the deformation ϵ is

$$\epsilon(\omega) = \epsilon_0 e^{i\omega t} \ , \tag{3.29}$$

the relative stress is phase shifted of an angle ϕ w.r.t. deformation of the anelastic body:

$$\sigma(\omega) = |E|\epsilon_0 e^{i(\omega t + \phi(\omega))} \ . \tag{3.30}$$

If the effects of anelasticity are small, equation (3.30) reduces to

$$\sigma(\omega) \simeq |E|\big(1 + i\phi(\omega)\big)\epsilon(\omega) \ . \tag{3.31}$$

From the previous formula it is evident that the introduction of anelasticity in the harmonic oscillator is the same as defining a generalized elastic constant with an imaginary part:

$$k = m\omega_0^2 \rightarrow \ m\omega_0^2(1 + i\phi) \tag{3.32}$$

and the transfer function of equation (3.26) becomes

$$H(\omega) = \frac{1}{m(\omega_0^2 - \omega^2 + i\phi\omega_0^2)} \ . \tag{3.33}$$

It is possible to show that the loss angle at the resonance frequency is related to the ratio between the dissipated energy in a cycle and the stored energy in the oscillation. In fact, the maximum energy of the oscillator is [30]

$$\mathcal{E}_{\text{stor}} = \frac{1}{2}\mathcal{R}e[\sigma]\mathcal{R}e[\epsilon] \tag{3.34}$$

and, for a deformation of the kind $\epsilon = \epsilon_0 e^{i\omega t}$, in the limit of low dissipation ($E_2 \ll E_1$), the maximum stored energy is

$$\mathcal{E}^{\text{max}}_{\text{stor}} = \frac{1}{2}\epsilon_0^2 E_1 \ . \tag{3.35}$$

The dissipated power is

$$W_{\text{diss}} = F\dot{x} = \mathcal{R}e[\sigma]\mathcal{R}e[\dot{\epsilon}] = \omega\mathcal{R}e[\sigma]\mathcal{I}m[\epsilon] \tag{3.36}$$

and, making the integral over a period, the dissipated energy is

$$\mathcal{E}^{T}_{\text{diss}} \doteq \left| \int_0^T W_{\text{diss}} dt \right| = \pi\epsilon_0^2 E_2 \ . \tag{3.37}$$

The relation between the loss angle and the introduced quantities is then

$$\phi^{-1}(\omega_0) \simeq (\tan\phi)^{-1} = \frac{E_1}{E_2} = 2\pi\frac{\mathcal{E}^{\text{max}}_{\text{stor}}}{\mathcal{E}^{T}_{\text{diss}}} \ . \tag{3.38}$$

It is usual to define a new parameter, the *quality factor* Q as

$$Q \doteq 2\pi\frac{\mathcal{E}^{\text{max}}_{\text{stor}}}{\mathcal{E}^{T}_{\text{diss}}} \ , \tag{3.39}$$

so that at the resonance $Q = \phi^{-1}(\omega_0)$.

As an example it is worthwhile to apply the anelastic model and the FDT to the harmonic oscillator. The most simple case is the damped harmonic oscillator with one degree of freedom; the damping is modeled by a loss angle ϕ that is comprehensive of all the loss sources:

$$\phi(\omega) = \sum_i \phi_i(\omega) \ . \tag{3.40}$$

The mechanical impedance of the system is

$$Z = \frac{m}{\omega}\big(\phi\omega_0^2 + i(\omega^2 - \omega_0^2)\big) \tag{3.41}$$

and the FDT (3.5) allows to calculate the power spectrum of the thermal noise

$$\tilde{x}_{\rm th}^2 = \frac{4k_BT}{m\omega}\frac{\phi\omega_0^2}{(\omega^2-\omega_0^2)^2+\phi^2\omega_0^4} \ . \tag{3.42}$$

Note that if there is no dissipation ($\phi = 0$) there is no fluctuation. In the limit of far higher or lower frequencies w.r.t. the resonance frequency, equation (3.42) reduces to

$$\tilde{x}_{\rm th}^2 = \frac{4k_BT}{m\omega}\frac{\phi(\omega)}{\omega_0^2+\omega_0^2\phi(\omega)^2} \ , \quad \text{for} \ \ \omega \ll \omega_0 \ , \tag{3.43}$$

$$\tilde{x}_{\rm th}^2 = \frac{4k_BT}{m\omega^5}\,\omega_0^2\phi(\omega) \ , \qquad\qquad \text{for} \ \ \omega \gg \omega_0 \ . \tag{3.44}$$

3.2 Dissipation models

Anelasticity can be described by a mechanical model [31] in which the system is treated as the parallel between a spring of restoring constant k on one side and a series of another spring with constant Δk and a dash-pot with damping constant c on the other side. The ideal body constructed in such a way is called *Debye's solid*. To calculate the effective restoring constant $k_{\rm eff}$ of the solid it is possible to use a method based on a parallelism between mechanical systems and electric circuits. In this way

$$k_{\rm eff} \simeq k\left(1 + i\frac{\Delta k}{k}\frac{\omega\tau}{1+\omega^2\tau^2}\right) \ , \tag{3.45}$$

where $\tau = c/\Delta k$ is the time constant that characterizes the response to the solicitation. Comparing with (3.32)

$$\phi(\omega) = \frac{\Delta k}{k}\frac{\omega\tau}{1+\omega^2\tau^2} \ . \tag{3.46}$$

This dependency of the loss angle w.r.t. frequency is called *Debye's peak*. Debye's peak reproduces the effects of many kinds of irreversible processes that happen in real bodies. The most important ones are examined in the following paragraphs.

Internal losses

Consider a solid body with an internal structure. Anelastic dissipations of acoustic energy in the lattice can occur in presence of dishomogeneities of temperature field (see on page 43); also processes that involve lattice phonons interaction can subtract energy [32]. In conductive solids it is not negligible the presence of dissipative processes, due to phonon-electron interactions, that occur also at very low temperature [33]. In the real lattice, rich of impurities and dislocations, imperfections play the role of dissipation sources. Irreversible processes due to defects in the lattice structure are various and not completely understood. They can involve point-like impurities, wide dislocations (parallel or not to the crystallographic axes) and effects of dislocation-impurity interactions [33].

3.2.1 Structural damping

Consider acoustic vibrations of an imperfect lattice. If it is vibrationally excited, the lattice can change its geometry toward more stable configurations. Also local vibrations of the impurities can be energetically preferred. These deformations and vibrations absorb acoustic energy from the mechanical vibrations causing their damping. For all these *structural* processes in the body it can be imagined an activation energy ΔU. Therefore the time constant of these anelastic processes depends on temperature and on activation energy following an Arrehnius' exponential law:

$$\tau_r = \tau_0 e^{\frac{\Delta U}{k_B T}} \ . \tag{3.47}$$

With this value for τ, the loss angle ϕ follows a Debye's peak:

$$\phi(\omega) = \frac{\Delta k}{k} \frac{\omega \tau_r}{1 + \omega^2 \tau_r^2} \ . \tag{3.48}$$

The experimental data do not agree with the previous formula. In a wide range of frequencies the loss angle for structural damping is almost constant. To model this experimental behavior a dominant relaxation process with a unique τ_0 is imagined, but with activation energies distributed with a density $f(u)$ almost constant over a great interval. It follows that:

$$\begin{aligned} \phi(\omega) &= \frac{\Delta k}{k} \int_{u_1}^{u_2} \frac{\omega \tau_r}{1 + \omega^2 \tau_r^2} f(u) du \\ &\simeq \frac{\Delta k}{k} f(\bar{u}) \int_{u_1}^{u_2} \frac{\omega \tau_r}{1 + \omega^2 \tau_r^2} \\ &= \frac{\Delta k}{k} f(\bar{u}) k_B T \big(\arctan(\omega \tau_1 - \arctan(\omega \tau_2) \big) \ , \end{aligned} \tag{3.49}$$

where

$$\tau_{1,2} = \tau_0 e^{\frac{u_{1,2}}{k_B T}} \ . \tag{3.50}$$

The loss angle $\phi(\omega)$ obtained is poorly dependent on frequency, and the flatness of the behavior increases with the widening of the interval $[u_1, u_2]$.

3.2.2 Thermoelastic damping

If the distribution of the temperature field of a vibrating body is not homogeneous, dissipation can occur. A mechanical vibration creates periodic contractions and stretching in some regions; in the compressed parts temperature increases and in the stretched ones it decreases. Under certain conditions a heat flux can be originated between two regions at a different temperature; the reaching of the equilibrium requires a characteristic time in which part of the vibrational energy is absorbed. Such a process is called *thermoelastic effect* [34, 35].

The importance of the thermoelastic effect w.r.t. other energy-absorption processes depends in a critical way on the geometric configuration of the vibrating body and on the particular kind of vibration. In fact, if the two regions with a different temperature are far away from each other, the time necessary for the thermalization is great and compressions and expansions occur in an adiabatic way. On the other hand if the two regions are near, the thermalization is almost instantaneous and the vibration is isothermal.

The typical heat-migration time τ_{th} between two regions at a distance d can be estimated starting from the equation of the heat diffusion [36]:

$$\frac{\partial T}{\partial t} = \frac{\kappa}{c_V}\nabla^2 T - \frac{E\alpha T_0}{c_V(1-2\sigma)}\frac{\partial(\nabla\cdot\boldsymbol{u})}{\partial t} \ , \tag{3.51}$$

where c_V is the specific heat per unit volume[3], κ the thermal conductivity, E Young's modulus, T the temperature, α the coefficient of linear thermal expansion and $\boldsymbol{u}$ the elastic deformation. It results that

$$\tau_{\rm th} \simeq d^2\frac{c_V}{\kappa} \ . \tag{3.52}$$

Defining $\omega_{\rm th} = 2\pi/\tau_{\rm th}$, if the vibrating angular frequency is $\omega \gg \omega_{\rm th}$ compression and expansion occur adiabatically; on the other hand, if $\omega \ll \omega_{\rm th}$ the process it isothermal. The thermoelastic effect will be maximum if ω and $\omega_{\rm th}$ are of the same order. Therefore Debye's peak is centered in $\omega_{\rm th}$ and has the form

$$\phi(\omega) = \phi_0\frac{\omega\omega_{\rm th}}{\omega^2+\omega_{\rm th}^2} \ , \tag{3.53}$$

---

[3] It is measured in $\frac{J}{m^3K}$.

where the constant coefficient ϕ_0 is

$$\phi_0 = TE\frac{\alpha^2}{c_V} \ . \tag{3.54}$$

Vibrating objects with a small section w.r.t. their length, as fibers and strings, typically show important thermoelastic peaks at the first resonance modes. This effect, vice versa, is not observable in thick objects for which ω_{th} is small w.r.t. the modal frequencies.

3.2.3 Superficial losses

Lattice defects and impurity are not distributed in a uniform way in the volume of the body. The region near the surface of the body is continually exposed to damages due to chemical or mechanical contacts: it is reasonable to think that most of the dissipation occurs in the external shell. In fact, in particular geometric configurations, materials with very low values of bulk loss angle appear to have greater losses because of superficial effects. The loss angle ϕ_{tot} including also these effects can be introduced as

$$\phi_{\text{tot}} = \frac{\Delta\mathcal{E}_{\text{bulk}} + \Delta\mathcal{E}_{\text{surf}}}{\mathcal{E}_{\text{tot}}} \ , \tag{3.55}$$

being $\mathcal{E}_{\text{tot}}$ the total energy stored in an oscillation, $\Delta\mathcal{E}_{\text{bulk}}$ and $\Delta\mathcal{E}_{\text{surf}}$ the absorbed energy in the volume and in the surface respectively. To describe the dependency of the superficial loss on the the geometry of the body it suffices [37] to assume that $\Delta\mathcal{E}_{\text{surf}}$ is proportional to the surface of the body and $\Delta\mathcal{E}_{\text{bulk}}$ to the volume. In this case it is possible to write:

$$\frac{\Delta\mathcal{E}_{\text{surf}}}{\Delta\mathcal{E}_{\text{bulk}}} = \mu d_s \frac{S}{V} \ . \tag{3.56}$$

The coefficient μ takes into account the relative amount of elastic deformation occurring at the surface — depending on the system geometry and oscillation mode-shape — and d_s, called dissipation deepness, has the dimension of a length and measures the entity of the surface dissipation. Because $\mathcal{E}_{\text{tot}}\simeq\mathcal{E}_{\text{bulk}}$, defining $\phi_{\text{bulk}} = \Delta\mathcal{E}_{\text{bulk}}/\mathcal{E}_{\text{bulk}}$, it follows

$$\phi_{\text{tot}} = \frac{\Delta\mathcal{E}_{\text{bulk}}}{\mathcal{E}_{\text{tot}}} + \frac{\Delta\mathcal{E}_{\text{surf}}}{\mathcal{E}_{\text{tot}}} = \phi_{\text{bulk}}\big(1 + \mu d_s \frac{S}{V}\big) \ . \tag{3.57}$$

For cylindrical fibers of diameter d, oscillating transversally to the axis of the fiber, $\mu = 2$ and

$$\phi_{\text{tot}} = \phi_{\text{bulk}}\big(1 + 8\frac{d_s}{d}\big) \ . \tag{3.58}$$

The superficial effects are relevant when $d_s \lesssim d$. The deepness d_s can be theoretically calculated [38] and, if Young's modulus is constant in the body,

$$d_s = \frac{1}{\phi_{\text{bulk}}} \int_0^h \phi(n) dn \ , \tag{3.59}$$

where h is the thickness of the superficial zone of dissipation. If the loss angle is constant w.r.t. the deepness it follows that

$$\phi_{\text{surf}} \simeq \frac{d_s}{h} \phi_{\text{bulk}} \ . \tag{3.60}$$

External losses

The three processes examined above take place inside the body determining its intrinsic anelasticity. On the other hand, energy losses can involve the ambient in which the body is settled. In the following the attention is focused on these external sources of losses.

3.2.4 Recoil losses

A vibrating body tends to transmit its oscillation to the supporting frame. In the ideal case the frame is infinitely massive and rigid, but, in reality, it is flexible and its mass is finite and so its vibration can be a dissipation source. It is possible to modelize this situation as in figure 3.1. Let m be the mass of the oscillating body connected with the supporting frame of mass M through

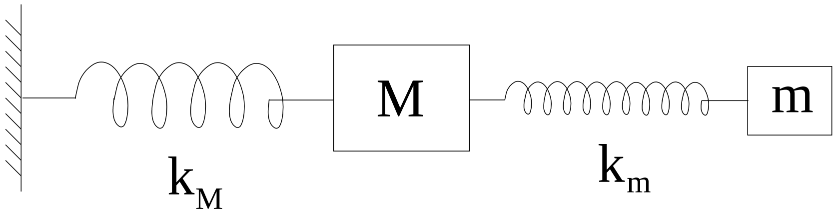

Figure 3.1: Schematization of the model done for calculating recoil losses.

a spring of elastic constant k_m. The frame is also joined to a perfectly rigid environment through another spring of elastic constant k_M. The dissipations on the masses m and M are included by means of ϕ_m and ϕ_M respectively. The elastic constants to use in the model become

$$k_m = m\omega_m^2(1 + i\phi_m) \qquad \text{and} \qquad k_M = M\omega_M^2(1 + i\phi_M) \; , \tag{3.61}$$

where ω_m and ω_M are the proper vibration frequencies of the body and of the frame. If the mass m is acted by a force F, from the equations of motion it follows

$$\frac{F}{x_m} = -m\omega_m^2 \left(-1 + \frac{\omega^2}{\omega_m^2} - i\phi_m + \frac{(1 + i\phi_m)^2}{\mu\frac{\omega_M^2}{\omega_m^2}(1 + i\phi_M) + 1 + i\phi_m - \mu\frac{\omega^2}{\omega_m^2}} \right) \; , \tag{3.62}$$

where $\mu = M/m$. After little manipulation the last expression can be written as

$$\frac{F}{x_m} = k_{\text{eff}} + im\omega_m^2\phi_{\text{eff}} \tag{3.63}$$

and the total dissipation is determined by the effective loss angle

$$\phi_{\text{eff}} = \phi_m + \phi_M \frac{\omega_m^2\omega_M^2}{\mu(\omega_M^2 - \omega_m^2)^2} \; . \tag{3.64}$$

Therefore this kind of loss has a tiny effect if $\mu \ll 1$; on the other hand, near the resonance of the system, the recoil losses are not negligible.

3.2.5 Air losses

If a body is vibrating in a fluid, it undergoes viscous friction causing dissipation. This loss source can be easily reduced keeping the oscillation under vacuum. The friction in a rarefied gas is well modeled by a force proportional to the velocity of the body:

$$F = -b\dot{x} \ . \tag{3.65}$$

In this case the transfer function defined in (3.4) is

$$H(\omega) = \frac{1}{m(\omega_0^2 - \omega^2 + i\frac{\omega b}{m})} \ , \tag{3.66}$$

from which, by comparison with (3.33), the expression for the loss angle due to gas friction can be derived:

$$\phi_{\text{gas}}(\omega) = \frac{b}{m\omega_0^2}\,\omega \ . \tag{3.67}$$

If the pressure is sufficiently low the mean free path of molecules is larger than the typical dimensions of the oscillator and the dissipation caused by the momentum transfer between the oscillator and the molecules is larger than that caused by the viscosity of the gas. In this case, calling ρ_{gas} the gas density and $\bar{v}$ the mean velocity of the gas molecules, it can be shown that [15, 40]:

$$b = \frac{1}{4}\rho_{\text{gas}}A\bar{v} \ , \tag{3.68}$$

where A is the surface of the body in which the friction occurs; therefore, in general[4]

$$\phi_{\text{gas}} = \frac{\rho_{\text{gas}}A\bar{v}}{4m\omega_0^2}\,\omega \ . \tag{3.70}$$

---

[4] For example, in the case of a cylindric vibrating fiber of diameter d, (3.70) leads to

$$\phi_{\text{gas}}(\omega) = \frac{\bar{v}\rho_{\text{gas}}}{2\rho d\omega_0^2}\,\omega \ . \tag{3.69}$$

For example, a lower limit on the Q-value limited by the air damping on a cylinder is expressed as

$$Q_{\mathrm{gas}} = d\frac{\rho\omega_0}{n\sqrt{m_{\mathrm{mol}}k_B T}} \ , \tag{3.71}$$

where d, ρ and ω_0 are the size, the density and the angular resonant frequency of the oscillator respectively. The values n and m_{mol} are the numerical density and mass of the gas molecules.

3.2.6 Dislocation propagation

In a mono-crystal lattice there can be a lot of defects: holes in the periodic structure, impurities, dislocations. Mechanical vibrations or thermal excitation can cause irreversible movements or vibrations of the dislocation lines connecting the impurities. In this way a part of the acoustic energy of the vibration can be absorbed. The Granato-Lücke theory [41] predicts a loss angle for the ultrasounds band according to the following law:

$$\phi(\omega) \propto \Omega L^4 \omega \ , \tag{3.72}$$

where Ω is the dislocation density, and L the mean length of a dislocation. In the low frequency region a vibration of a dislocation of a certain length L generates a Debye's peak. Experiments have found that ϕ has an almost constant behavior w.r.t. frequency and therefore it is necessary to suppose a continuous distribution of length L that makes the theory fit the experimental data as explained at the end of § 3.2.1.

Therefore the acoustic waves dissipation theories for dislocation propagation are still in progress. At the moment the theoretical formulas include hardly measurable parameters (e.g. density of dislocation and Burger's vector) or arbitrary relaxation-time distributions. One thing is definitely sure: the dislocation losses are proportional to the dislocation density and can be reduced with processes such as the baking of the material.

3.2.7 Impedance coupling

In the case of longitudinal acoustic waves in a bar the impedance can be written as

$$Z = S\sqrt{\rho E}\ , \tag{3.73}$$

where S is the section of the bar, ρ its density and E its Young's modulus. To avoid acoustic wave radiation at the contact surface of two connected bars, the impedances shall be chosen to be very different from each other. In the case of contacts between solids of an arbitrary shape it is very difficult to quantify the impedances of the two bodies but the material choices that give very different values for $\sqrt{\rho E}$ seem to give good results.

To limit the acoustic wave radiation, it seems reasonable to reduce the contact surface. For example in the case of contact between a cylinder of length L and radius r, and a plane parallel to its axis the surface is given by:

$$S = \sqrt{\frac{4Flr}{\pi}\left(\frac{1-\nu_1^2}{E_1} + \frac{1-\nu_2^2}{E_2}\right)}\ , \tag{3.74}$$

where E_1 and ν_1 are Young's modulus and Poisson's ratio of the cylinder, E_2 and ν_2 the ones of the solid plane and F the force exerted on the surface. Typically the material choice does not allow a great variation of Young's modulus and so it is the cylinder radius reduction that minimizes the contact surface.

3.3 Thermal noise calculation methods

To apply the FDT (3.18) in calculating the thermal noise power spectrum, it is necessary to know the real part of the admittance of the system in a broad frequency band. This is usually hard work because the imaginary part is much bigger than the real one [42, 43, 44]. Thus, to calculate $\mathcal{R}e[Y(\omega)]$ there are different methods that try to overcome this difficulty. Chronologically, the first one used was the so called "normal-mode expansion" that derives $\mathcal{R}e[Y(\omega)]$ from the measured Q-values of each mode of the resonator, supposing homogeneity of the losses. A natural extension of this method is the so called "advanced mode expansion" introduced recently to take into account the inhomogeneous losses on the resonator [45]. This method gives a clear physical interpretation of the losses processes and it's substantially in agreement with the nowadays used techniques called "direct approaches" that do not require any mode decomposition [46, 16, 12, 18].

3.3.1 Normal mode expansion

In the following it will be described how to derive the thermal noise of an oscillator through the method of the normal-mode expansion. An observable physical quantity X of a system is

$$X(t) = \int \boldsymbol{u}(\boldsymbol{r}, t) \cdot \boldsymbol{P}(\boldsymbol{r}) dV \ , \tag{3.75}$$

where $\boldsymbol{u}(\boldsymbol{r}, t)$ is the displacement vector of the system at the location $\boldsymbol{r}$ at time t and $\boldsymbol{P}(\boldsymbol{r})$ is a vector weighting function defining the physical quantity to be observed. For example, for thermal noise fluctuation of the internal modes of interferometers' mirrors, $\boldsymbol{r}$ is a 2-dimensional vector on the surface of the mirror and $\boldsymbol{P}(\boldsymbol{r})$ is the laser beam profile. The power spectrum density of X, S_X, is obtained from the equation (3.18). In order to calculate the admittance in (3.18), the generalized force $F(t)\boldsymbol{P}(\boldsymbol{r})$ is applied on the system, leading, for the system without dissipation, to the following equation of motion:

$$\rho \frac{\partial^2 \boldsymbol{u}}{\partial t^2} + \mathcal{L}(\boldsymbol{u}) = F(t)\boldsymbol{P}(\boldsymbol{r}) \ , \tag{3.76}$$

where ρ is the density and $\mathcal{L}(\boldsymbol{u})$ a linear operator representing the elastic response of the system. The solution of (3.76) can be viewed as a superposition of basis functions $\boldsymbol{w}(\boldsymbol{r})$:

$$\boldsymbol{u}(\boldsymbol{r},t)=\sum_n \boldsymbol{w}_n(\boldsymbol{r})q_n(t) \ , \tag{3.77}$$

where $\boldsymbol{w}_n$ satisfy the eigenvalues problem

$$\mathcal{L}\big(\boldsymbol{w}_n(\boldsymbol{r})\big)=\rho\omega_n^2\boldsymbol{w}_n(\boldsymbol{r}) \ , \tag{3.78}$$

ω_n being the angular resonant frequency of the n-th resonant mode of the system. The $\boldsymbol{w}_n(\boldsymbol{r})$ are orthogonal:

$$\int \rho(\boldsymbol{r})\boldsymbol{w}_i(\boldsymbol{r})\cdot\boldsymbol{w}_j(\boldsymbol{r})dV=m_i\delta_{ij} \ , \tag{3.79}$$

and can be normalized imposing

$$\int \boldsymbol{w}_n(\boldsymbol{r})\cdot\boldsymbol{P}(\boldsymbol{r})dV=1 \ . \tag{3.80}$$

The parameter m_n is called effective mass of the n-th mode and δ_{ij} is Kroneker's symbol. The function $q_n(t)$ in (3.77) represents the time evolution of the n-th mode. To derive the equation of motion for q_n, the expression (3.77) for $\boldsymbol{u}$ is substituted in (3.76). Multiplying (3.76) by $\boldsymbol{w}_n$ and using (3.79) and (3.80), it follows

$$m_n\ddot{q}_n(t)+m_n\omega_n^2q_n(t)=F(t) \ . \tag{3.81}$$

Therefore, the time evolution of the n-th mode is the same as that of a harmonic oscillator of mass m_n and angular resonant frequency ω_n with an external force $F(t)$ acting on it. Putting (3.77) in (3.75) and using (3.80) it follows

$$X(t)=\sum_n q_n(t) \ , \tag{3.82}$$

showing that the observable coordinate X can be simply described as a superposition of the motions of the harmonic oscillators q_n. Moreover, the kinetic energy of the system E_{kin} is expressed as

$$E_{\text{kin}}=\int\frac{1}{2}\rho|\dot{\boldsymbol{u}}(\boldsymbol{r},t)|^2dV=\sum_n\frac{1}{2}m_n|\dot{q}_n|^2 \ , \tag{3.83}$$

showing that it is the sum over all the harmonic oscillators energies $m_n|\dot{q_n}|/2$. To evaluate the admittance function $Y(\omega)$, the equation of motion (3.81) is rewritten in the frequency domain, including the dissipation:

$$-m_n\omega^2\tilde{q_n} + m_n\omega_n^2\big(1 + i\phi_n(\omega)\big)\tilde{q_n} = \tilde{F}\ , \tag{3.84}$$

where $\phi(\omega)$ is the loss angle. From the previous equation and (3.82), $Y(\omega)$ is described as

$$Y(\omega) \div \frac{\widetilde{\dot{X}}(\omega)}{\widetilde{F}(\omega)} = i\omega\frac{\sum_n \tilde{q}_n}{\widetilde{F}(\omega)} = i\omega\sum_n \frac{1}{-m_n\omega^2 + m_n\omega_n^2\big(1 + i\phi_n(\omega)\big)}\ . \tag{3.85}$$

The power spectrum density of X, S_X can now be derived using (3.18) and (3.85):

$$S_X(\omega) = \frac{4k_BT}{\omega}\sum_n \frac{\omega_n^2\phi_n(\omega)}{m_n\big((\omega^2-\omega_n^2)^2 + \omega_n^4\phi_n^2(\omega)\big)}\ . \tag{3.86}$$

Therefore the thermal motion of the system is the sum of the harmonic oscillators of the normal-mode expansion. Equation (3.86) allows to calculate the thermal noise from the angular resonant frequency ω_n, the effective mass m_n and the loss angle $\phi_n(\omega)$ of each mode. The angular resonant frequency and the displacement of the mode $\boldsymbol{w}_n$ are obtained from the eigenvector problem (3.78). The effective mass m_n is calculated from the $\boldsymbol{w}_n$ found and equation (3.79). The loss angle is derived from the experiments but its measurement in a wide frequency range is commonly difficult; thus, it is usual to estimate it from the Q-value on the resonant frequencies according to the following relation:

$$Q_n = \frac{1}{\phi_n(\omega_n)}\ ; \tag{3.87}$$

this formula is frequently used to estimate the thermal noise of interferometers through the structural damping model.

3.3.2 Advanced mode expansion

Theoretical researches of the nineties [47, 48, 49, 46] have shown that the predictions on thermal noise made by the normal-mode expansion were wrong in the case of oscillators with inhomogeneous losses. The reasons of this disagreement come clear if one considers the more accurate mode expansion called "advanced mode expansion" [45]. The difference between this expansion and the traditional one relies on the introduction of the dissipation term in the equation of motion from the very beginning and not after the mode decomposition.

In the case of viscous damping the equation (3.76) becomes now

$$\rho\frac{\partial^2 \boldsymbol{u}}{\partial t^2} + \rho\Gamma(\boldsymbol{r})\frac{\partial \boldsymbol{u}}{\partial t} + \mathcal{L}(\boldsymbol{u}) = F(t)\boldsymbol{P}(\boldsymbol{r}) \; , \tag{3.88}$$

$\Gamma(\boldsymbol{r})$ being the coefficients of the friction forces. Following the same procedure as in the previous section and considering the dissipation term as a perturbation, the derived equation for the n-th mode is

$$-m_n\omega^2\tilde{q_n} + m_n\omega_n^2\big(1 + i\phi_n(\omega)\big)\tilde{q}_n + \sum_{k\neq n} i\alpha_{nk}(\omega)\tilde{q}_k = \tilde{F} \; , \tag{3.89}$$

where α_{nk} is defined by

$$\alpha_{nk} = \omega \int \rho(\boldsymbol{r})\Gamma(\boldsymbol{r})\boldsymbol{w}_i(\boldsymbol{r}) \cdot \boldsymbol{w}_j(\boldsymbol{r})dV = \alpha_{kn} \tag{3.90}$$

and

$$\phi_n(\omega) = \frac{\alpha_{nn}(\omega)}{m_n\omega_n^2} \; . \tag{3.91}$$

The last term of the left-hand side of (3.89) does not exist in the formula obtained from the traditional mode expansion. It contains the contributions to one mode due to the coordinates of all the others, i.e., it accounts for the coupling between modes. The normal mode expansion gives results consistent with the advanced mode expansion only if all the $\alpha_{nk}(n \neq k)$ vanish. The comparison between (3.90) and (3.79) tells that this happens if

$$\Gamma(\boldsymbol{r}) = \Gamma \ , \tag{3.92}$$

that is, if the losses are homogeneously distributed over the oscillator.

It is possible to apply the advanced mode expansion to a body with inhomogeneous structural damping. The equation of motion for an elastic isotropic body is

$$\rho \frac{\partial^2 u_i}{\partial t^2} - \frac{\partial \sigma_{ij}}{\partial x_j} = F(t) P_i(\boldsymbol{r}) \tag{3.93}$$

where u_i and P_i are the i-th components of the displacement $\boldsymbol{u}$ and of the weighting function $\boldsymbol{P}$, and the stress tensor is

$$\sigma_{ij} = \frac{E_0}{1+\sigma}\left(u_{ij} + \frac{\sigma}{1-2\sigma} u_{ll}\delta_{ij}\right) \ , \tag{3.94}$$

where E_0 is Young's modulus, σ Poisson's ratio and u_{ij} the strain tensor. To take into account the structural damping the stress tensor is rewritten in the frequency domain as

$$\sigma_{ij} = \frac{E_0\big(1 + i\phi(\omega, \boldsymbol{r})\big)}{1+\sigma}\left(u_{ij} + \frac{\sigma}{1-2\sigma} u_{ll}\delta_{ij}\right) \ , \tag{3.95}$$

where ϕ is the loss angle. Following the same procedure as in the case of viscous damping, the derived equation for the n-th mode is exactly equation (3.89), with ϕ as in (3.91) and α_{nk} now defined by

$$\alpha_{nk} \doteqdot \int \frac{E_0 \phi(\omega \boldsymbol{r})}{1+\sigma}\left(w_{n,ij} w_{k,ij} + \frac{\sigma}{1-2\sigma} w_{n,ll} w_{k,ll}\right) dV = \alpha_{kn} \ , \tag{3.96}$$

where $w_{n,ij}$ is the strain tensor of the n-th mode. The condition of not having coupling terms between the modes now becomes

$$\phi(\omega, \boldsymbol{r}) = \phi(\omega) \ . \tag{3.97}$$

This implies that the traditional mode expansion is valid when the damping is homogeneous.

The advanced mode expansion relies on the approximation that the dissipation could be treated as a perturbation. This happens if the following condition on the distance between the resonant peaks is satisfied:

$$|\alpha|^2_{nk} \ll \frac{m_n m_k}{4}|\omega_n^2 - \omega_k^2|^2 \; . \tag{3.98}$$

It is worthwhile to think about the physical reason for which an inhomogeneous distributed loss can cause mode coupling. Consider the decay of a single resonant mode. When the loss is homogeneous the phase of its decay does not depend on the position and so the displacement shape does not change w.r.t. time. If the loss is concentrated in some regions, a phase lag will appear in those places and, as a consequence, the shape of the displacement will change, i.e., other modes will be excited.

3.3.3 Direct approach

Nowadays the most used technique to calculate the thermal noise is the direct method. Its difference from the previous ones relies on a computation that leaves aside a modal decomposition. There are many different ways of implementing this computation. In the following the main analytical one, by Levin [46] will be reviewed, together with the numerical dynamic approach firstly used by Numata [18].

Levin's method

In 1997 Y. Levin [46] proposed a new technique in calculating mirror thermal noise. The novelty of his approach consists essentially in restating the FDT for a continuous combination of coordinates (3.18) in an easier to calculate form. Consider the surface of the mirror invested by the laser beam which has a profile given by the weighting function $P(\boldsymbol{r})$. The read-out variable will be

$$X_{\text{new}}(t) = \int P(\boldsymbol{r})u(\boldsymbol{r},t)d^2r \ , \tag{3.99}$$

where $u(\boldsymbol{r})$ is the displacement of the mirror surface in the direction of the beam propagation axis. At the end of § 3.1.2 it was shown that, if we have to deal with a coordinate X_{new} that is a continuous combination of coordinates, the thermal noise power spectrum will take the form

$$S_{X_{\text{new}}}(\omega) = \frac{4k_BT}{\omega^2}\mathcal{R}e[Y_{\text{new}}(\omega)] \ , \tag{3.100}$$

where Y_{new} is the admittance associated with the new coordinate as defined in (3.24). Therefore, the calculus of the thermal noise reduces to the calculus of the real part of the admittance. Levin suggested an easy way to calculate $\mathcal{R}e[Y_{\text{new}}]$. Suppose to apply on the mirror surface an oscillatory continuous force $F(\boldsymbol{r},t)$ that mocks the profile $P(\boldsymbol{r})$ of the laser beam:

$$F(\boldsymbol{r},t) = F_0\cos(\omega t)P(\boldsymbol{r}) \ ; \tag{3.101}$$

this force, as explained in § 3.1.2, corresponds to a generalized force

$$F_{\text{new}}(t) = F_0\cos(\omega t) \ , \tag{3.102}$$

that drives only the momentum conjugate to the X_{new} defined in (3.99); therefore, using the definition of Y_{new}, it is possible to calculate the mean dissipated power

$$\begin{aligned}\langle W_{\text{diss}}\rangle &= \langle \mathcal{R}e[\widetilde{F}_{\text{new}}\widetilde{\dot{X}}_{\text{new}}]\rangle = \\ &= \langle \mathcal{R}e[\widetilde{F}^2_{\text{new}}Y_{\text{new}}]\rangle = \\ &= F_0\langle \mathcal{R}e[\cos^2(\omega t)Y_{\text{new}}]\rangle = \\ &= \frac{1}{2}F_0^2\mathcal{R}e[Y_{\text{new}}]\end{aligned} \tag{3.103}$$

and to rewrite the fluctuation dissipation theorem (3.18) in the form

$$S_X(\omega) = \frac{8k_BT}{\omega^2}\frac{\langle W_{\text{diss}}\rangle}{F_0^2} \ . \tag{3.104}$$

Also Nakagawa [16] solved the same Levin's problem in a different formalism, using Green's function, but arriving at exactly the same result. It is worth to mention that Tsubono [45] developed an interesting method based on matrix formalism, that is quite simple to apply but is limited to analyze system that extends mainly in only one dimension.

Numerical dynamic approach

This method was firstly introduced by Numata [18]. To avoid all the problems related to an analytical calculation, he decided to perform a finite element analysis of the system. In this way he could solve the equation of motion numerically and then apply the FDT theorem in the form of (3.104). He was not forced to do any static approximation and so the problem of finding the mirror thermal noise was solved even in the frequency region near mirror resonances. Moreover, in his analysis, he could use models of the mirror including *separately* the magnets and the coating, performing calculations that would have been difficult to do with the analytical method. Basically, the steps of the method are the following:

- do a geometric model of the complete system and mesh[5] it, in order to have a model with not too many elements but with a good mesh definition in the smallest and in the most solicited parts,
- apply boundary constraints and an oscillatory force on the mirror surface mocking the laser beam profile,
- perform a harmonic analysis at the desired frequency,
- extract from the solved model the dissipated energy multiplying, element by element, the stored strain energy by the loss angle,

---

[5] The meaning of the words "mesh" and "elements" will be clarified in chapter 5.

- apply equation (3.104) in order to extract the thermal noise for the system at the chosen frequency,
- redo the last three steps for all the desired frequencies.

In chapter 5 it is shown that the potential of finite element analysis is highly enhanced if the model is performed with a particular care in driving the mesh and applying the pressure profile: this allows to perform harmonic analyses on a *complete* model of the actual mirror (never done before) and opens the field to faster and more precise parametric analyses.

Chapter 4

Thermal noise of interferometers and some relevant problems for Virgo

In this chapter, after a theoretical review of the various sources of thermal noise for interferometers, just listed in § 2.2, a discussion is presented on the relevant problems a Virgo-like interferometer has to deal with, especially looking at future developments towards a better sensitivity. A review of the studies performed in the past years for minimizing the loss angle in mirrors, mirror coatings and suspensions is then presented, identifying the most relevant causes of loss, trying to modelize the dissipation processes and to measure the losses on bulk, membrane and fibre samples.

The thermal noise limits the interferometer sensitivity in a frequency band that ranges from few Hertz to about 1 kHz.

This noise is intimately related to the mechanics of the suspension system used for the mirrors and to the geometry and constitution of the mirror itself. In interferometer detectors the mirrors are suspended at the end of a chain of oscillators for damping as much as possible the horizontal and the vertical motion of the ground together with the thermal noise coming from the upper stages. In fact, over the lower characteristic frequency of the resonators, oscillations are filtered and suppressed. Therefore, the main sources of thermal noise are the components of the mirror-suspension *last* stage. Firstly our attention will be focused on the mirror and its behaving under the impinging laser beam and then on the suspension-system resonator.

4.1 Mirror-bulk thermal noise

In this section the theoretical model of the bulk contributions to the mirror thermal noise will be reviewed. The theoretical efforts done in the last decade can be referred to three main branches: Brownian thermal noise, thermoelastic noise and thermal lensing.

Brownian thermal noise can be interpreted as a fluctuation of the mirror surface position coming from the mirror recoil from its internal phonons or, using the FDT, as fluctuations induced by a structural damping.

Thermoelastic noise is intended as a noise that comes from the coupling of thermal fluctuations with displacement fluctuations thanks to a non-null coefficient of thermal expansion.

Finally, thermal lensing is caused by the coupling of thermal fluctuation to phase fluctuations of the light (and therefore to measured displacement) thanks to a non-null coefficient $\beta = dn/dT$, where n is the refraction index and T is the temperature.

4.1.1 Brownian thermal noise

Normal mode expansion

This section is a short review of the results of the modal-expansion analysis (presented in § 3.3.1), in the approximation of a free mirror with an impinging laser beam with a Gaussian profile. A detailed calculation for the Virgo mirrors with this procedure was done by Bondu and Vinet [50]. The basic idea is to solve with a harmonic analysis the equation of the acoustic-wave propagation in the continuous media:

$$\rho \partial_t^2 \boldsymbol{u} = \mu \nabla^2 \boldsymbol{u} + (\lambda + \mu) \nabla (\nabla \cdot \boldsymbol{u}) \ , \tag{4.1}$$

where $\boldsymbol{u}$ is the displacement of each point of the solid and λ and μ are the Lamé coefficients. Passing to cylindric coordinates, A.E.H. Love [51] found three independent solutions (two transversal and one longitudinal) that can be mixed as proposed by J.R. Hutchinson [52] to satisfy all the constraints to be imposed on the external surfaces of the mirror, that is considered free. It results that all the constraints can be satisfied only for a set of particular frequencies. Three numbers, n, ξ and m, identify the various solutions (one for each frequency): n represents the number of nodal diameters of the mode under consideration (it enters through the Bessel functions J_n of which the solutions are a superposition), ξ is a boolean variable representing the parity (1 or 0 depending on if the opposed mirror faces oscillate on phase or not) and m is the order number (that plays a role very similar to n but in the radial direction instead of the azimuthal one).

If a Gaussian beam of waist $w_0 = \sqrt{2} r_0$ is impinging on the center of the mirror, it sees a displacement equal to

$$\Delta z = \int_S u_z(r, \phi, z = 0) \frac{1}{\pi r_0^2} e^{-\frac{r^2}{r_0^2}} r dr d\phi \ , \tag{4.2}$$

where S is the surface of the mirror, located at $z = 0$. It can be shown that $n \geqslant 1$ implies $\Delta z = 0$. Therefore, only the modes with $n = 0$ (that are axisymmetric and referred to as *“drum modes”*) are a source of noise. Given a certain displacement Δz the effective mass m_i can be defined through the relation

$$\frac{1}{2} m_i \omega_i^2 \Delta z^2 \doteqdot \mathcal{E} \ , \tag{4.3}$$

where i is the index of the mode (the set n, ξ, m) and $\mathcal{E}$ is the energy of the mode, calculated from

$$\mathcal{E} = \int_V \Big(\frac{\lambda}{2} u_{ii}^2(\boldsymbol{r}) + \mu u_{ik}^2(\boldsymbol{r})\Big) dr^3 \tag{4.4}$$

where the integral is intended over the whole mirror volume V and $u_{ik}(\boldsymbol{r})$ are the components of the strain matrix. The thermal noise can be calculated using (3.86), where the summation has to be done over a number of modes that assures a good convergence of the series. This is a critical point of this method, because it can happen that there is not such a frequency and, moreover, even if the series converges, it can bring to a wrong result due to the coupling between the various modes produced by the presence of inhomogeneous losses (that are not included in the model as explained in § 3.3.2). For the Virgo mirrors, supposing a bulk loss angle ϕ_B not depending on frequency, they calculated the Brownian thermal noise for the bulk to be

$$S_{x,\mathrm{B}}^{\mathrm{Brown}} = 3 \times 10^{-38} \frac{T}{300\ \mathrm{K}} \frac{100\ \mathrm{Hz}}{f} \frac{\phi_\mathrm{B}}{10^{-6}} \frac{\mathrm{m}^2}{\mathrm{Hz}}\ . \tag{4.5}$$

Advanced mode expansion

Unfortunately there are no calculations done on mirrors using this method (see § 3.3.2) and Yamamoto himself, in his work on it [45], says that the analysis is not performed with this method because it would be necessary to take into account too many modes for having a good convergence of the series.

Levin's method

Following the idea presented in § 3.3.3 Levin [46] calculated the thermal noise for a mirror with homogeneously distributed losses, so that Young's modulus $E' = E\big(1 + i\phi(\omega)\big)$ can be used. If this is the case, using (3.38) it is straightforward to calculate the average dissipated power $\langle W_{\mathrm{diss}} \rangle$ under the application of an oscillatory force:

$$\langle W_{\mathrm{diss}} \rangle = \mathcal{E}_{\mathrm{stor}}^{\mathrm{max}} \omega \phi(\omega) \ , \tag{4.6}$$

where $\mathcal{E}_{\mathrm{stor}}^{\mathrm{max}}$ is the energy of the elastic deformation of the mirror at the moment of maximal strain configuration. Levin supposed that the mirror is an infinite half-space and that the force F_0 is a static one (a reasonable hypothesis because the first resonance mode of the mirror is far higher than the region of interest). With these assumptions he obtained

$$\mathcal{E}_{\mathrm{stor}}^{\mathrm{max}} = \frac{1-\sigma^2}{2\sqrt{2\pi} E r_0} F_0^2 \ , \tag{4.7}$$

where σ is Poisson's ratio of the material. Assuming $\phi(\omega) = \phi_{\mathrm{B}}$, from (3.104) it follows:

$$S_{x,\mathrm{B}}^{\mathrm{Brown}}(\omega) = \frac{4k_B T}{\omega} \frac{1-\sigma^2}{\sqrt{2\pi} E r_0} \phi_{\mathrm{B}} \ . \tag{4.8}$$

As for the homogeneous case an identical result was reported by Braginsky [53], calculating the real part of the admittance of the system and using (3.18). The calculation was also made by Bondu et al. [54], Nakagawa et al. [55] and reviewed by Liu and Thorne [56] in the case of a finite size mirror. Their result is

$$S_{x,\mathrm{B}}^{\mathrm{Brown}}(\omega) = \frac{8k_B T}{\omega} \phi_{\mathrm{B}}(\omega)(U_0 + \Delta U) \ , \tag{4.9}$$

where U_0 and ΔU are infinite series of Bessel function with coefficients depending on the material properties and on mirror and beam-spot size dimensions. If compared with the result in the approximation of infinite mirror mass, this calculation gives a correction that, e.g. in the case of the new LIGO-II mirrors, starts to be greater than 10% for beam spot sizes greater than 2.5 cm. Considering that there is the project to use flat beams, this correction becomes crucial in estimating the Brownian thermal noise correctly.

Numerical dynamic approach

Following the method described in § 3.3.3 Numata calculated the thermal noise using a finite element analysis. He performed the simulation [18] for the BK7 mirror used in his experiment (7 cm in diameter, 6 cm thick) in three separate cases: homogeneous losses, losses coming only from the coating, losses coming only from the magnets. His results are in good agreement with analytical approximated calculations [57]. He showed that the relative error is about 3% in the case of coating loss and that the magnets contribution can be neglected.

4.1.2 Thermoelastic noise

The thermoelastic noise is generated by temperature fluctuations that couple with displacement thanks to the non-null coefficient of thermal expansion α. Energy is dissipated because of the thermal flux induced by the generated temperature field.

Temperature fluctuations can be originated either by intrinsic thermodynamical fluctuation, or by laser-photon absorption.

By thermodynamical fluctuations

In the field of the thermoelastic noises, thermodynamical fluctuations are the FDT-counterpart of the thermoelastic damping process. The mechanism of this kind of dissipation was explained in § 3.2.2. To calculate this noise for the mirror it is necessary to solve the equation of elasticity [30] for a field of deformation $\boldsymbol{u}$

$$\frac{1-\sigma}{1+\sigma}\nabla(\nabla\cdot\boldsymbol{u}) - \frac{1-2\sigma}{2(1+\sigma)}\nabla\times\nabla\times\boldsymbol{u} = \alpha\nabla\delta T \ , \tag{4.10}$$

together with the thermal conductivity equation for the temperature dishomogeneity δT

$$\frac{\partial \delta T}{\partial t} - \frac{\kappa}{c_V}\nabla^2 \delta T = -\frac{\alpha E T}{c_V(1-2\sigma)}\frac{\partial(\nabla \cdot \boldsymbol{u})}{\partial t} \ , \tag{4.11}$$

where E, σ, α, κ and c_V are Young's modulus, Poisson's ratio, the coefficient of linear thermal expansion, the thermal conductivity and the specific heat per unit volume of the mirror.

Braginsky et al. [53] solved the problem using the fluctuation-dissipation theorem in the form (3.18), approximating the mirror with an infinite half-space and considering that the frequency ω is far higher w.r.t. the typical frequency of the heat flow

$$\omega_c = \frac{1}{\tau_{th}} = \frac{\kappa}{r_0^2 c_V} \ , \tag{4.12}$$

where r_0 is the beam radius and τ_{th} was defined in (3.52). This is the so called *adiabatic limit* in which the second term on the right hand side of (4.11) is neglected. They found that the displacement power spectrum is

$$S_{x,\mathrm{B}}^{\mathrm{th\text{-}d}_\alpha} = \frac{8k_B}{\sqrt{2\pi}}(1+\sigma)^2\kappa\left(\frac{\alpha T}{c_V}\right)^2\frac{1}{r_0^3\omega^2} \ . \tag{4.13}$$

Moreover they solved the same system of coupled equations directly calculating the displacement fluctuations and using the Langevin approach (without using the FDT). On the mirror they applied a heat source — the right side of (4.11) — coming from the temperature fluctuations satisfying the following thermodynamical relation:

$$\langle \delta T^2 \rangle = \frac{k_B T^2}{V c_V} \ . \tag{4.14}$$

The solution they found is exactly the same as (4.13), therefore he demonstrated that thermodynamical fluctuations of temperature are the physical source of fluctuations deduced by FDT based on thermoelastic damping.

Liu and Thorne [56] solved the same problem with the same approximations applying the FDT in Levin's form (3.104) and using

$$W_{\text{diss}} = \left\langle \frac{TdS}{dt} \right\rangle = \left\langle \int \frac{k_T}{T} (\nabla \delta T)^2 dV \right\rangle , \tag{4.15}$$

where S is the entropy of the system and the temperature perturbation δT comes from the law of adiabatic temperature change [30]

$$\delta T = -\frac{\alpha E T \nabla \cdot \boldsymbol{u}}{c_V (1 - 2\sigma)} . \tag{4.16}$$

They achieved the same solution (4.13). They also made the calculations for a finite cylindrical test mass finding the correction factor w.r.t. the infinite test mass solution. It is worth noting that the correction for a wide range of beam-spot size is not greater than 10% if the ratio between the radius and the thickness of the cylinder is near unity.

Cerdonio et al. [58] extended the Liu analysis releasing the assumption of the adiabatic limit, i.e. performing the analysis that is valid also at low temperatures and/or small beam spot size. Equation (4.13) has to be multiplied by a correction factor $\Omega^2 J(\Omega)$ with[1]

$$\Omega \doteqdot \frac{\omega}{\omega_c} , \tag{4.17}$$

$$J(\Omega) = \sqrt{\frac{2}{\pi^3}} \int_0^\infty du \int_{-\infty}^\infty dv \frac{u^3 e^{-u^2/2}}{(u^2 + v^2)\big((u^2 + v^2)^2 + \Omega^2\big)} \tag{4.18}$$

and ω_c as defined in (4.12). For $\omega \gg \omega_c$ this factor is equal to unity but for $\omega \ll \omega_c$ goes as $\omega^{3/2}$ and then $S_{x,\mathrm{B}}^{\text{th-d}_\alpha} \propto \omega^{-1/2}$.

By photothermal fluctuations

This effect is called dynamic photo-thermal noise[2] and it is due to the temperature fluctuation induced by random absorption of optical photons in

---

[1] Formula (4.18) in [58] had a wrong factor as noted by Numata [18].

[2] It is also referred to as photo-thermal shot noise.

the surface layer of the mirror. Thanks to a non-null coefficient of thermal expansion these fluctuations couple with displacement fluctuations.

Braginsky et al. [53] assumed that the coating thickness of the mirror is much smaller than the beam radius, and, in the adiabatic limit, found the following expression for the power spectral displacement noise:

$$S_{x,\mathrm{B}}^{\text{ph-th}_\alpha} = \frac{2}{\pi^2}(1+\sigma)^2\left(\frac{\alpha}{c_V r_0^2}\right)^2 \hbar\omega_0 \langle W_{\mathrm{abs}}\rangle \frac{1}{\omega^2} \ , \tag{4.19}$$

where the mean of the absorbed power W_{abs} is intended over a period π/ω_{gw} and $\hbar\omega_0$ is the typical energy of the absorbed photons.

Cerdonio et al. [58] extended the calculation releasing the assumption of the adiabatic limit finding:

$$S_{x,\mathrm{B}}^{\text{ph-th}_\alpha} = \frac{2}{\pi^2}(1+\sigma)^2\left(\frac{\alpha}{\kappa}\right)^2 \hbar\omega_0 \langle W_{\mathrm{abs}}\rangle K(\Omega) \ , \tag{4.20}$$

with

$$K(\Omega) = \left| \frac{1}{\pi}\int_0^\infty du \int_{-\infty}^\infty dv \frac{u^2 e^{-u^2/2}}{(u^2+v^2)(u^2+v^2+i\Omega)} \right| . \tag{4.21}$$

Equation (4.20) reduces to (4.19) for $\omega \gg \omega_c$ but for low frequencies it gives lower values w.r.t. the adiabatic prediction and it displays a behavior almost independent of frequency.

4.2 Mirror-coating thermal noise

As done in the mirror-bulk thermal noise section the review is logically divided into three parts: Brownian thermal noise, thermoelastic noise and thermorefractive noise.

4.2.1 Brownian thermal noise

Following their formalism [16], Nakagawa et al. [57] calculated the dissipation induced by an inhomogeneous loss distribution on a half-infinite mirror due to the fact that loss angle in the bulk material ϕ_{B} is different from loss angle in the coating ϕ_{C}:

$$S_{x,\mathrm{C}}^{\mathrm{Brown}} = \frac{4k_B T}{\omega} \frac{(1+\sigma_{\mathrm{B}})(1-2\sigma_{\mathrm{B}})}{\pi E_{\mathrm{B}}} \frac{d_{\mathrm{C}}}{r_0^2} \phi_{\mathrm{C}} \,, \tag{4.22}$$

where E_{B}, σ_{B} and d_{C} are the bulk Young's modulus, the bulk Poisson's ratio and the coating thickness respectively. It is worth noting that there is a linear dependence on $1/r_0^2$ as predicted by the scaling argumentation done by Levin [46] and that the result is exactly the same if performed using Levin's method [46, 57].

Harry et al. [38], using Levin's method, generalized this result for a non-isotropic coating loss ϕ_{C}

$$\phi_{\mathrm{C}} = \left(\frac{\delta U_{\parallel} d_{\mathrm{C}}}{U} \phi_{\parallel} + \frac{\delta U_{\perp} d_{\mathrm{C}}}{U} \phi_{\perp} \right) \,, \tag{4.23}$$

where $\delta U_{\parallel}$ and $\delta U_{\perp}$ are the surface integrals of the coating energy-density components along the parallel and perpendicular direction w.r.t. the surface, $\phi_{\parallel}$ and $\phi_{\perp}$ are the associated coating loss angles and U is the total energy stored in the bulk. For a thin coating, provided that $\sigma_{\mathrm{C}} \simeq \sigma_{\mathrm{B}}$, $E_{\mathrm{C}} \doteqdot E_{\mathrm{C}\parallel} \simeq E_{\mathrm{C}\perp}$ and $\sigma_{\mathrm{C}} \doteqdot \sigma_{\mathrm{C}\parallel} \simeq \sigma_{\mathrm{C}\perp}$, they found[3]

$$\phi_{\mathrm{C}} = \frac{1}{\sqrt{2\pi}} \frac{d_{\mathrm{C}}}{r_0} \left(\frac{E_{\mathrm{C}}(1+\sigma_{\mathrm{B}})(1-2\sigma_{\mathrm{B}})^2 + E_{\mathrm{B}}\sigma_{\mathrm{C}}(1+\sigma_{\mathrm{C}})(1-2\sigma_{\mathrm{B}})}{E_{\mathrm{B}}(1+\sigma_{\mathrm{C}})(1-\sigma_{\mathrm{C}})(1-\sigma_{\mathrm{B}})} \phi_{\parallel} + \right.$$

$$\left. \frac{E_{\mathrm{B}}(1+\sigma_{\mathrm{C}})(1-2\sigma_{\mathrm{C}}) - E_{\mathrm{C}}\sigma_{\mathrm{C}}(1+\sigma_{\mathrm{B}})(1-2\sigma_{\mathrm{B}})}{E_{\mathrm{C}}(1-\sigma_{\mathrm{C}})(1+\sigma_{\mathrm{B}})(1-\sigma_{\mathrm{B}})} \phi_{\perp} \right) \tag{4.24}$$

and therefore

$$S_{x,\mathrm{C}}^{\mathrm{Brown}} = \frac{4k_B T}{\omega} \frac{(1-\sigma_{\mathrm{B}})^2}{\sqrt{2\pi} E_{\mathrm{B}} r_0} \phi_{\mathrm{C}} \,. \tag{4.25}$$

Equation (4.25) is valid provided that the coating loss occurs in the coating materials themselves and not for rubbing in the bulk/coating or layer/layer

---

[3] It is worth to note that Harry [59] recently performed some calculations to account for eventual anisotropies in Young's modulus and Poisson's ratio of the coating.

interfaces. At the first order in σ_{B} and σ_{C} formula (4.25) reduces to

$$S_{x,\mathrm{C}}^{\mathrm{Brown}} = \frac{2k_BT}{\omega}\frac{d_{\mathrm{C}}}{\pi E_{\mathrm{B}} r_0^2}\left(\frac{E_{\mathrm{C}}}{E_{\mathrm{B}}}(1-2\sigma_{\mathrm{B}})\phi_{\parallel} + \sigma_{\mathrm{C}}(\phi_{\parallel}-\phi_{\perp}) + \frac{E_{\mathrm{B}}}{E_{\mathrm{C}}}\phi_{\perp}\right) . \tag{4.26}$$

If $\phi_{\parallel} \simeq \phi_{\perp}$, then the lowest coating-induced thermal noise occurs when Young's modulus of the coating is matched to that of the substrate.

4.2.2 Thermoelastic noise

Temperature fluctuations (that couple with displacement thanks to $\alpha_{\mathrm{C}} \neq 0$) can be originated either by intrinsic thermodynamical fluctuation, or by laser-photon absorption.

By thermodynamical fluctuations

The problem was extensively treated by Braginsky and Vyatchanin [60].

Firstly, using the Langevin approach, they solved the problem for a half-infinite mirror with an expansion coefficient $\alpha'_{\mathrm{C}} \doteqdot \alpha_{\mathrm{C}} - \alpha_{\mathrm{B}}$ for the coating and $\alpha'_{\mathrm{B}} = 0$ for the bulk; the bulk and the coating are treated as if they had the same elastic constants. Taking into account only stresses produced by the coating due to non-uniform temperature distribution, they obtained

$$S_{x,\mathrm{C}}^{\mathrm{th\text{-}d}_\alpha} = \frac{4\sqrt{2}}{\pi}(1+\sigma_{\mathrm{B}})^2 \frac{{\alpha'_{\mathrm{C}}}^2 k_B T^2}{\sqrt{\kappa_{\mathrm{B}} c_{V_{\mathrm{B}}}}}\left(\frac{d_{\mathrm{C}}}{r_0}\right)^2 \frac{1}{\sqrt{\omega}} . \tag{4.27}$$

Secondly, using the FDT theorem, they calculated a formula for the case of different elastic parameters between the bulk and the coating: it suffices to use the same formula (4.27) with[4]

$$\alpha'_{\mathrm{C}} = \frac{\alpha_{\mathrm{C}}}{2\alpha_{\mathrm{B}}}\left(\frac{1+\sigma_{\mathrm{C}}}{(1-\sigma_{\mathrm{C}})(1+\sigma_{\mathrm{B}})} + \frac{E_{\mathrm{C}}(1-2\sigma_{\mathrm{B}})}{E_{\mathrm{B}}(1-\sigma_{\mathrm{C}})}\right) - \frac{c_{V_{\mathrm{C}}}}{c_{V_{\mathrm{B}}}} , \tag{4.28}$$

They generalized formula (4.27) and (4.28) for multilayer coating [60] also. Thirdly, using the FDT approach developed by Liu and Thorne [56], they

---

[4] The formula in [60] has an error, successively corrected by [61] as reported.

calculated the finite test mass correction factor that, e.g., is about 1.6 in the case of LIGO-II.

Recently Fejer et al. [61] performed the same calculation in the case of different thermoelastic properties of coating and substrate (other than thermal expansion) and out of the low-frequency region.

By photothermal fluctuations

In literature this effect was not given so much attention because of its smallness. An estimate of the behaving of the effect was made by Rao [62]. He studied two different cases depending on the values assumed by the thermal conductivity in the bulk $\kappa_{\rm B}$ and in the coating $\kappa_{\rm C}$.

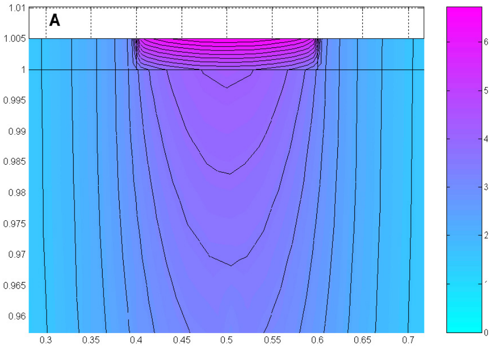

Figure 4.1: Heat flow simulation on a coated mirror with a highly conductive bulk.

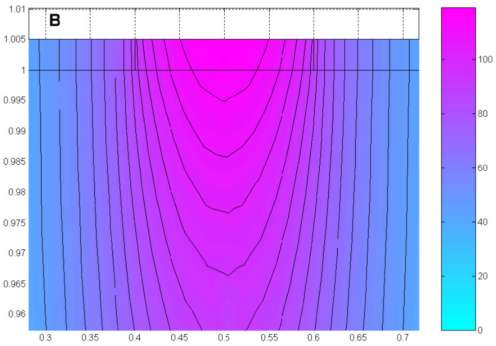

Figure 4.2: Heat flow simulation on a coated mirror with a low conductive bulk.

If $\kappa_{\rm B} \gg \kappa_{\rm C}$, the heat generated by photons absorption flows in the coating essentially in one dimension (see figure 4.1). Following the same approach of Braginsky et al.[53] he found that

$$S_{x,\rm C}^{\text{ph-th}_\alpha} = \frac{2}{\pi^2}\left(\frac{\alpha_{\rm C}}{c_{V_{\rm C}} r_0^2}\right)^2 \hbar\omega_0 \langle W_{\rm abs}\rangle \frac{1}{\omega^2}\left(1 - e^{-d_{\rm C}\sqrt{i\omega c_{V_{\rm C}}/\kappa_{\rm C}}}\right)^4 , \qquad (4.29)$$

where

$$\alpha_C = \frac{1}{d}(\alpha_1 d_1 + \alpha_2 d_2) , \qquad (4.30)$$

calling α_1, α_2 and d_1, d_2 the coefficients of thermal expansion and the total thickness for the two coating materials. At high frequencies equation (4.29) takes the same dependency form as (4.19) and at low frequencies approaches zero.

If $\kappa_{\rm B} \ll \kappa_{\rm C}$ the heat flow behaves like shown in figure 4.2. Following a technique similar to [60], he solved the heat flow in a uniform half-space, computing the average temperature for a layer near the surface with a frequency-dependent scale height determined by $r_t = \sqrt{\kappa/(\rho c_V \omega)}$. He found

$$S_{x,\rm C}^{\text{ph-th}_\alpha} = \frac{1}{\pi^2}\left(\frac{\alpha_{\rm C} d_{\rm C}}{r_0^2}\right)^2 \frac{\hbar\omega_0 \langle W_{\rm abs}\rangle}{c_{V_{\rm C}}\kappa_{\rm C}} \frac{1}{\omega} \ , \tag{4.31}$$

that shows a behavior like $1/\omega$.

4.2.3 Thermorefractive noise

The thermorefractive noise is generated by temperature fluctuations that couple with phase fluctuations of the laser (and therefore with measured displacement) thanks to the non-null coefficient $\beta = dn/dT$, where n is the refraction index. Temperature fluctuations can be originated either by intrinsic thermodynamical fluctuation, or by laser-photon absorption.

By thermodynamical fluctuations

Following the same approach as in [53], Braginsky et al. [63] calculated the thermorefractive noise induced by thermodynamical fluctuation of temperature. Considering the frequency range (that is typical for the ground interferometer) in which the detection frequency ω satisfies

$$d_{\rm C} \ll \frac{\sqrt{\kappa_{\rm C}/c_{V_{\rm C}}}}{\sqrt{\omega}} \ll r_0 \ , \tag{4.32}$$

where $d_{\rm C}$ is the coating thickness and r_0 the beam radius, they calculated

$$S_{x,\rm C}^{\text{th-d}_\beta} = \frac{\sqrt{2}}{\pi} \frac{k_B}{\sqrt{c_{V_{\rm C}}\kappa_{\rm C}}} \left(\frac{\beta_{\rm eff}\lambda T}{r_0}\right)^2 \frac{1}{\sqrt{\omega}} \ , \tag{4.33}$$

where[5]

$$\beta_{\text{eff}} = \frac{n_1 n_2(\beta_1 + \beta_2)}{4(n_1^2 - n_2^2)} \tag{4.34}$$

and $\beta_1 = dn_1/dT$, $\beta_2 = dn_2/dT$, the indexes referring to the two materials alternating in the coating layers.

By photothermal fluctuations

This effect is numerically much smaller than the other thermorefractive noise, just discussed here before, and it will not be reviewed (see, e.g., [64] for details).

4.3 Suspension thermal noise

Usually the horizontal damping of the test mass is obtained through simple pendula and the vertical one through springs or blades. These kinds of filters introduce noise in each degree of freedom of the whole structure they enter, according to the fluctuation dissipation theorem. This problem has been theoretically dealt with since the early nineties [65, 66, 67] and can be divided into four separate contributions: the pendulum thermal noise, the vertical thermal noise, the violin-modes thermal noise and the tilt/rotational mode thermal noise.

4.3.1 Pendulum thermal noise

The suspension wires, together with the suspended mass, constitute a pendulum with a proper resonance frequency determined by the restoring elastic force of constant $k_e(1 + i\phi_e)$ and by the gravity force acting as a spring of constant $k_g = mg/l$, that is lossless. The viscous damping of the air is made negligible by the low pressure involved (10^{-9} mbar) and so the equation of

---

[5] The formula reported in [63] was wrong and was successively corrected [60] as it is reported.

motion can be written as

$$m\ddot{x} = -k_g x - k_e(1 + i\phi_e)x \ , \tag{4.35}$$

which is equivalent to

$$m\ddot{x} = -(k_g + k_e)\big(1 + i\frac{k_e}{k_g + k_e}\phi_e\big)x \ ; \tag{4.36}$$

therefore the effective loss angle is equal to

$$\phi_{\text{eff}} = \phi_e \frac{k_e}{k_g + k_e} \simeq \phi_e \frac{k_e}{k_g} \ , \tag{4.37}$$

being usually $k_e \ll k_g$. The factor k_e/k_g is called "dilution factor" and it is evident that, thanks to it, the effective losses of the pendulum system are much lower than the internal ϕ_e. The elastic constant k_e of a wire is given by [39]

$$k_e = \frac{1}{2l^2}\sqrt{TEI} \ , \tag{4.38}$$

where l is the wire length, T is the tension applied on the wire, E is Young's modulus of the material and I is the superficial moment of inertia of a wire cross-section. In the last-stage suspension different solutions can be adopted in the way the test mass is suspended, depending on how many wires are used. To reduce the dilution factor it is convenient to have T and I as low as possible. Usually the wires are loaded at a defined ratio c ($c \simeq 0.3 \div 0.4$) of their breaking stress σ_b. Therefore, if the mirror is suspended with a certain load in a multi-wire configuration, the tension on each wire is reduced and the radius of the wire can be reduced accordingly. If there are N wires for a mirror of mass m, the requirement for being at the working tension is

$$\frac{mg}{N\pi r^2} = c\sigma_b \tag{4.39}$$

and so the elastic constant is

$$k_e = \frac{N}{2l^2}\sqrt{TEI} = \frac{N}{2l^2}\sqrt{\frac{mg}{N}E\frac{\pi r^4}{4}} = \frac{1}{4l^2 c\sigma_b}\sqrt{\frac{m^3 g^3 E}{N\pi}} \ , \tag{4.40}$$

where (4.39) was used to explicitly show the dependence on m and N. The loss angle is then

$$\phi_{\text{eff}} = \phi_e \frac{1}{4lc\sigma_b}\sqrt{\frac{mgE}{N\pi}} \tag{4.41}$$

and this value can be used to evaluate the pendulum thermal noise using formula (3.42) with $\omega_0 = \sqrt{g/l}$:

$$S_x^{\text{pend}} = \frac{4k_BT}{m\omega}\frac{\phi_{\text{eff}}\omega_0^2}{(\omega^2-\omega_0^2)^2+\phi_{\text{eff}}^2\omega_0^4}\ . \tag{4.42}$$

Since the band of interest is over the resonance frequency (from a few Hertz to few a hundred Hertz) the approximated formula (3.44) can be used, showing that the pendulum thermal noise scales as $m^{-1/2}$ and $N^{-1/2}$.

4.3.2 Vertical mode thermal noise

Owing to the non uniform gravitational field generated by the earth, local vertical directions at both ends of the arms are not parallel to each other. Therefore, a vertical motion of the mirrors gives a change in the cavity length that can mock a gravitational wave signal. The coupling between the vertical motion and the horizontal one is exactly equal to the angle under which an arc of length $L_{\text{arm}}/2$ is seen from the center of the earth (figure 4.3). For this

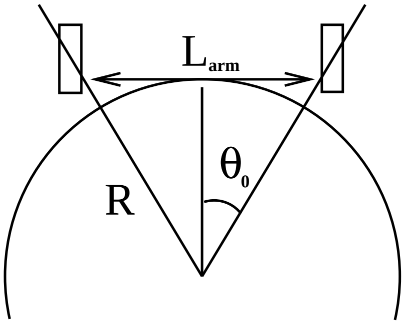

Figure 4.3: The vertical directions at the ends of the arm are not parallel and give origin to a coupling between the vertical and the horizontal displacements of the mirrors.

reason a part of the thermal noise associated with the vertical oscillation is seen on the horizontal direction according to the following formula:

$$S_x^{\text{vert}} = \theta_0 \frac{4k_BT}{m\omega} \frac{\phi\omega_v^2}{(\omega^2-\omega_v^2)^2+\phi^2\omega_v^4} \ , \tag{4.43}$$

in which ω_v is the resonance frequency of the vertical motion of the system whose value is given by

$$\omega_v^2 = \frac{\pi r^2 E/l}{m/N} = \frac{gE}{c\sigma_b l} \ , \tag{4.44}$$

where l is the wire length, E and σ_b are Young's modulus and the breaking stress of the material and (4.39) was used to show explicitly that there is no dependence on the mass m of the mirror and on the number N of suspension wires.

4.3.3 Violin modes thermal noise

The wires suspending the mirror present numerous resonances relative to the normal modes of oscillation called violin modes. These oscillations show up each time a wire is under a certain tension. If there are N wires of density ρ, Young's modulus E, radius r and length l, cross-sectional inertia momentum I, holding a mirror of mass m, considering that the load on each wire is $T = mg/N$ and the linear density of the wire is $\rho_{lin} = \pi r^2\rho$, the resonance angular frequencies will be [39]

$$\omega_n = \frac{n\pi}{l}\sqrt{\frac{T}{\rho_{lin}}}(1+a) = \frac{n\pi}{l}\sqrt{\frac{mg/N}{\pi r^2\rho}}(1+a) \ , \tag{4.45}$$

where

$$a = \frac{2}{l}\sqrt{\frac{EI}{T}} = \frac{2}{l}\sqrt{\frac{E\pi r^4/4}{mg/N}} \ , \tag{4.46}$$

and n is the mode number under consideration. The violin mode contributions to thermal noise can be evaluated using [39]:

$$S_x^{\text{viol}} = N\frac{4k_BT}{\omega}\frac{2\rho r^2 l}{\pi m^2}\sum \frac{1}{n^2}\frac{\omega_n^2\phi_n}{(\omega^2-\omega_n^2)^2+\phi_n^2\omega_n^4} \ , \tag{4.47}$$

where the loss angle ϕ_n of each mode is given by

$$\phi_n = \frac{a\phi(\omega_n)}{1 + \frac{a}{4}n^2\phi^2(\omega_n)} \ . \tag{4.48}$$

Therefore, the contribution of this noise to the sensitivity curve is limited to the various resonance frequencies of the suspension system.

4.3.4 Tilt and rotational modes thermal noise

The term "tilt mode" is referred to the oscillation of the suspended mirror around a horizontal axis perpendicular to the laser beam, while "rotational mode" is referred to the oscillation around a vertical axis.

The angular displacements θ induced by these modes are expressed by formulas similar to (4.42) where the appropriate angular frequency and loss angle should be used. These modes have no effect on the sensitivity at the first order in θ because the induced optical path difference is $\delta L \sim \theta^2$.

4.4 The problem of new materials for Virgo

Having a look at figure 4.4, it is possible to make some considerations on the perspective to improve Virgo sensitivity fighting the various noise floors in the relative frequency bands. As already said in § 2.5.2, the main contributions limiting the sensitivity from higher to lower frequencies are the shot noise, the mirror thermal noise and the suspension noise. As regards the seismic noise, Virgo can already be considered an advanced gravitational detector, because of the superattenuator system (see § 2.5.1).

4.4.1 Lowering the shot noise

Shot noise limits the sensitivity for frequencies over 500 Hz.

Looking at (2.4) it is evident that a direct way of lowering the shot noise floor is to use a higher power laser. In a provisional draft about an advanced

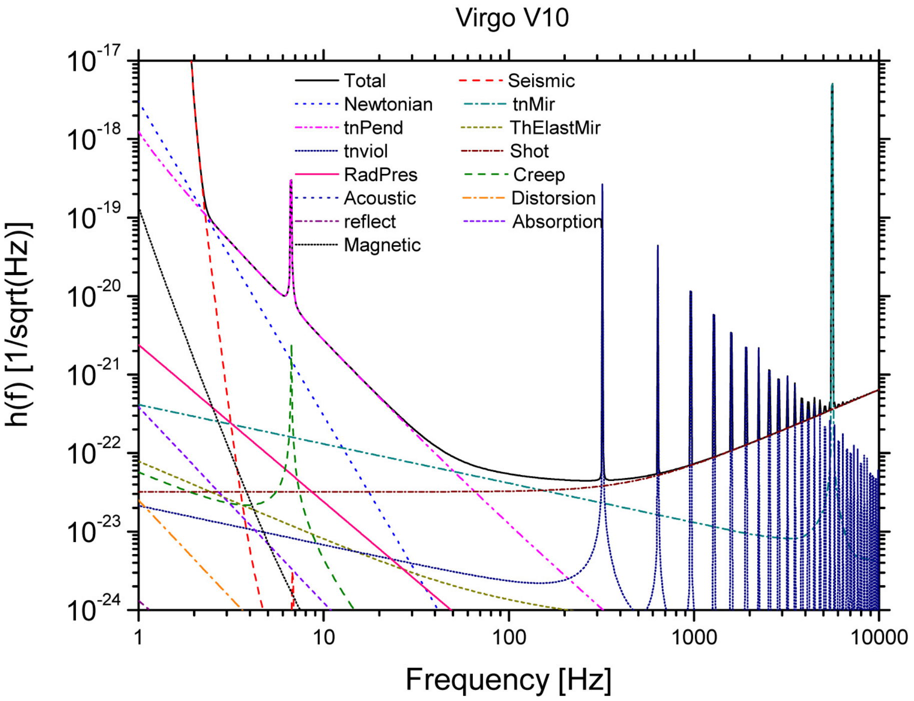

Figure 4.4: The Virgo sensitivity curve with all its main noise contributions (taken from [23]).

Virgo [64] a laser of 100 W is foreseen, gaining a factor $\sqrt{5}$ in sensitivity. Apart from the technical problems of going to further higher powers, there is a limitation imposed by the radiation pressure noise. According to equation (2.8) this noise increases as the square root of the power impinging on the beam splitter. Fortunately it has a dependence on the inverse of the suspended mass also, so that it can be convenient to go toward higher loads.

4.4.2 Lowering mirror-bulk thermal noise

In the frequency region between 50 Hz and 500 Hz the dominating noise is the Brownian thermal noise of the mirror substrate (see § 4.1.1).

According to (4.5) or (4.9) this noise is proportional to the loss angle ϕ_B of the mirror substrate. This is why during the last years a lot of efforts have been done in order to measure losses in various substrates and trying to estimate the intrinsic loss in the frequency region of interest. Hereafter a short list of recent results is furnished.

Rowan et al. [68], using metal-wire single-loop suspensions, have measured a loss factor of 3.7×10^{-9} for HEM sapphire, grown by a method suitable for producing test masses of the required size and quality.

Numata et al. [69, 70, 71] performed accurate series of measurements on fused-silica bulk-samples using a nodal support system (a horizontal mirror on a ruby ball touching the center of the mirror face). They found values for ϕ_B ranging from 2.5×10^{-8} to 1.5×10^{-6}, demonstrating that the nodal technique is a valid one in this kind of high precision measurements and that annealing helps to increase the quality factor. They also verified that the losses have a behavior that is roughly proportional to frequency. The understanding of this phenomenon is crucial in estimating the quality factor in the 50÷500 Hz band, which usually is some orders of magnitude lower than the frequency-region of measurements on samples. Willems and Busby [72] suspended sapphire and fused silica samples with the same method as [68]; the wires were mechanically polished and greased with lard. They obtained phi down to 4×10^{-9} for sapphire and 8.3×10^{-9} for fused silica.

Smith et al. [73] measured bulk loss angles on fused silica masses attached to fused silica suspensions in a configuration adopted in the last 2 stages of GEO 600 finding loss angles down to 2.6×10^{-7}.

Penn et al. [74], relying on measurements performed on several fused silica samples of various shapes, proposed a heuristic model of the loss angle ϕ as a function of both frequency and volume to surface ratio:

$$\begin{aligned}\phi(f,V/S) &= \phi_\mathrm{surf}+\phi_\mathrm{bulk}+\phi_\mathrm{th-el} = \\ &= C_1(V/S)^{-1}+C_2 f^{C_3}+C_4\phi_\mathrm{Debye}(f)\ ,\end{aligned} \tag{4.49}$$

where $\phi_\mathrm{Debye}(f)$ is a function embedding the typical Debye peak described by equation (3.53). The best fit for the four parameters gave, in the case of

Suprasil 2 and Suprasil 312, the results shown in table 4.1. It is worth to note

Type	C_1	C_2	C_3	C_4
2	8.6×10^{-9}	7.1×10^{-12}	0.8	1.0
312	7.1×10^{-9}	4.6×10^{-12}	0.8	—

Table 4.1: Best fit values of the four parameters of the function described in (4.49) for Suprasil 2 and Suprasil 312 samples.

that the exponent of the explicit frequency dependency is 0.8, which gives a strong frequency dependence of the loss angle. This value is in agreement with the value found by Wiedersich et al.($\simeq 0.78$ [75]) with light scattering experiments on silica glass. A plot of $\phi(f, V/S)$ is shown in figure 4.5. For

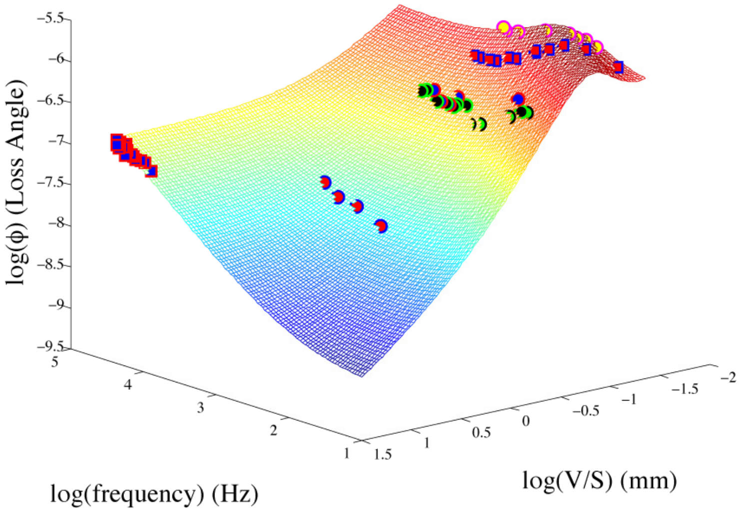

Figure 4.5: A plot of the best fit to data for the 2-d function described by (4.49), modeling with 4 parameters the loss as a superposition of bulk, surface and thermoelastic losses.

frequencies around 200 Hz and for volume-to-surface ratio of the order of 1 cm (for a mirror this number can be up to 10 cm) the estimated loss angle is further lower w.r.t. all the available measurements.

Penn et al. [76] and Ageev et al. [77], following an experimental setup of the same kind of Gretarsson et al. [37], performed some measurements on annealed fused silica rods, finding values down to 5×10^{-9} for the loss angle.

4.4.3 Lowering mirror-coating thermal noise

The problem of treating thermal noise in the coating is not trivial because it requires the knowledge of modeling the effects of non-homogeneously distributed losses (coating loss angles are usually higher than bulk loss angles). Yamamoto [45] clarified definitely the unreliability of the normal-mode expansion method (see § 3.3.1) in this kind of problems and proposed an advanced modal expansion method (see § 3.3.2) as a solid theoretical tool. By the way, from the practical point of view, it was two years before, with Levin [46] and his direct method, (see § 3.3.3) that actual calculations started to be possible.

The first ones who demonstrated the invalidity of the normal-mode expansion experimentally were Yamamoto et al. [79] with measurements on an inhomogeneous slab. Their theoretical predictions [80] for mirror thermal noise with inhomogeneous losses (performed using Levin's method) were confirmed by their experimental work [81, 82] on an aluminum hollow cylinder to which they could apply an arbitrary loss distribution through eddy currents induced by strong magnets. They studied two distinct cases (also with the help of FEA): losses concentrated in the front face of the mirror (the laser side) and losses in the back face, demonstrating the importance of the loss distribution w.r.t. the position of the impinging laser beam.

The results reviewed in the previous paragraph are extremely encouraging, in the frame of lowering the mirror-bulk thermal noise, but they immediately open the field to other battles, this time against the noise induced by Brownian and thermodynamical fluctuations in the coating.

By Brownian fluctuations

Calculating the ratio of the Brownian thermal noise for the bulk, equation (4.8), to the one for the coating, equation (4.22), it follows

$$\frac{S_{x,\mathrm{B}}^{\mathrm{Brown}}}{S_{x,\mathrm{C}}^{\mathrm{Brown}}} = \sqrt{\frac{\pi}{2}}\frac{1-\sigma_{\mathrm{B}}^2}{(1+\sigma_{\mathrm{B}})(1-2\sigma_{\mathrm{B}})}\frac{\phi_{\mathrm{B}} r_0}{\phi_{\mathrm{C}} d_{\mathrm{C}}} \simeq \sqrt{\frac{\pi}{2}}\frac{\phi_{\mathrm{B}} r_0}{\phi_{\mathrm{C}} d_{\mathrm{C}}} \simeq \frac{5\times 10^{-5}}{\phi_{\mathrm{C}}}\,, \tag{4.50}$$

where, in the last passage, the values $\phi_B \simeq 5\times 10^{-9}$, $r_0 \simeq 5\times 10^{-2}$ m, $d_{\mathrm{C}} \simeq 5\times 10^{-6}$ m have been used. It is evident that, if ϕ_{C} is higher than 5×10^{-5}, the Brownian thermal noise of the coating starts to be a serious problem. This is why a lot of researchers focused their efforts on measuring the intrinsic loss of the coatings.

The effect of optical coating deposition on fused silica slabs was studied by Gretarsson et al. [83]. In their work they stressed the importance of keeping under control dissipations due to surface losses (see § 3.2.3). They showed that a variety of surface treatments (washing with detergent, acetone, KOH, or HF etching) produced no change in the condition of the surface or made it a little worse. They found that the intrinsic loss angle of the standard SiO_2/Ta_2O_5 coating was $\phi_{\mathrm{C}} \simeq 4\times 10^{-4}$.

Crooks et al. [84] performed measurements on Al_2O_3/Ta_2O_5 coatings deposited on two fused silica mirrors. They found an excess loss of unknown source: it was neither due to the inhomogeneity of the coating, nor due to the possible difference among $\phi_{\|}$ and $\phi_{\perp}$ in the coating (see § 4.2.1), nor due to the friction in the mirror suspension points. By the way, with a multivariate regression analysis they got $\phi_{\mathrm{C}} = (6.4\pm 0.6)\times 10^{-5}$.

In a companion paper Harry et al. [38], following the model reviewed in § 4.2.1, tried to measure $\phi_{\|}$ of SiO_2/Ta_2O_5 coating on three fused silica samples. They found $\phi_{\|} = (4.2\pm 0.3)\times 10^{-4}$ for coatings deposited on commercially polished slides and $\phi_{\|} = (1.0\pm 0.3)\times 10^{-4}$ for coating deposited on a superpolished disk.

Penn et al. [85] investigated the sources of loss in SiO_2/Ta_2O_5 coatings on polished and annealed fused silica samples of various thickness. Their series of measurements give strong evidence that losses due to coating/bulk and layer/layer interfaces are negligible w.r.t. losses associated to the intrinsic ϕ of the material constituting the coating.

By thermodynamical fluctuations

As for the thermal noise induced by thermodynamical fluctuations on the coatings, the situation can be even more critical. Equations (4.33) and (4.27) do not depend on the intrinsic loss of the coating and so the research should move on quite a new field, exploring the possibility of using different materials in order to achieve the aimed sensitivities.

To have an idea of the relative weight of the thermorefractive contribution and the thermoelastic one in the coating losses, the square root of the ratio between (4.33) and (4.27) can be used:

$$\sqrt{\frac{S_{x,\mathrm{C}}^{\text{th-d}_\beta}}{S_{x,\mathrm{C}}^{\text{th-d}_\alpha}}} \simeq \sqrt{\frac{\beta_{\text{eff}}^2\lambda^2}{4(1+\sigma_{\mathrm{B}})\alpha'^2_{\mathrm{C}}d^2}} \simeq \frac{\beta_{\text{eff}}\lambda}{2\alpha' d_{\mathrm{C}}} \, , \tag{4.51}$$

which, in the case of SiO_2/Ta_2O_5 coatings on a fused silica substrate, is around[6] 2÷3. It is evident that relative weight strongly depends on the thermoelastic characteristic of the materials involved. From a theoretical point of view, good models trying to take into account the differences among the thermoelastic coefficients of the bulk and the various layer materials are being developed (see § 4.2). To have an idea of the variety of the out-coming effects, figure 4.6 can be considered: following thermoelastic predictions by Fejer et al. [61], it is evident how different the effect of the same type of coating (e.g. Al_2O_3/Ta_2O_5) can be in dependence of the substrate it is applied

---

[6] This factor was initially found to be about 7 time smaller because of the used value $\alpha_{Ta_2O_5} = -4\times10^{-5}$ [86] instead of $\alpha_{Ta_2O_5} = 4\times10^{-6}$ [87, 88].

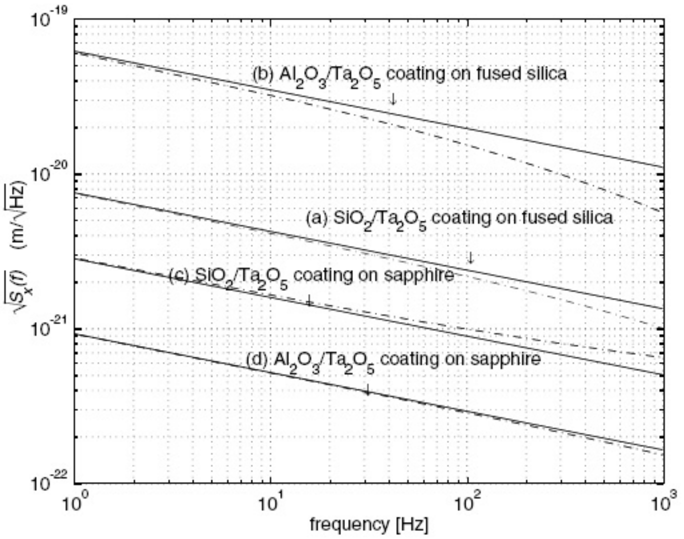

Figure 4.6: Calculated thermoelastic noise [61] of coatings of Al_2O_3/Ta_2O_5 or SiO_2/Ta_2O_5, applied to silica or sapphire samples. Dashed lines are from the complete model, solid lines from the low-frequency approximation.

to.

On this research line there is the work by Baker et al. [89] about the dependence of hardness on density of Ta_2O_5 layers, through Rutherford backscattering spectroscopy and nanoindentation studies. Tien et al. [87] performed simultaneous measurements of $\alpha_{Ta_2O_5}$ and $E_{Ta_2O_5}$ and Braginsky et al. [88] performed measurement of $\alpha_{Ta_2O_5}$, both groups using phase shifting interferometry.

There is a clear need to carry out a series of experiments, in which coating parameters are systematically varied as this will allow the source of the coating losses to be investigated.

4.4.4 Lowering suspension thermal noise

In the frequency region up to 50 Hz the dominating noise is the thermal noise of the suspension (see § 4.3). Among the various suspension thermal noise contributions, pendulum thermal noise is by far the main important one.

Looking at (4.42) and (4.41) it is evident that it is convenient to suspend heavy masses in a multiple-wire configuration using materials with a high breaking stress and low internal loss angle. Researches on materials with good properties in the past years proceeded together with the studies on the clamping and on the identification of possible excess losses.

The first measurements testing the theoretical models were performed by Gillespie and Raab [90, 91], giving encouraging results.

Cagnoli et al. [92] focused the attention on the geometry of the clamp for the suspensions. They obtained a significant decrease of losses due to the stick-and-slip mechanism on the clamp surfaces by increasing and localizing the clamping pressure on the heads of the suspension wires. Their work gave a strong impulse to investigate suspension techniques different from clamping, like welding [93] and silicate bonding [94].

Ageev et al. [95, 96] studied excess losses connected with loaded suspension wires made of steel and tungsten. They found that spurious increases of the noise floor and isolated noise peaks (which could not be explained by a mechanical shot noise model [92]) are much less present in steel wires than in tungsten wires. A recent study by Gretarsson and Saulson on tungsten and silica fibres [97] demonstrated that such kind of effects are negligible.

Cagnoli et al. [98] performed internal friction measurements for the normal modes of circular fibres of different materials demonstrating that the loss angle in fused silica is 2 orders of magnitude better than the one in metallic wires.

Gretarsson and Harry [37] performed accurate measurements on fused silica fibres reducing clamp losses thanks to the introduction of an isolation bob between the sample and the clamp. They noted that surface losses dominated at diameter values less than about 1 mm.

Experiments on all fused-silica massive pendula [99, 100] gave values for the total loss angle around 10^{-8}.

Ribbons seem to be a good alternative to fibres [101] and recently [102] it has been shown that, with the correct aspect-ratio choice (to minimize thermoelastic damping) they can perform even better than fibres.

4.4.5 Guidelines for new materials

To summarize, there are a number of constraints which affect the selection of materials for test masses, coatings and suspensions of long baseline gravitational wave detectors. In addition to the common feature of having a very low loss angle at room temperature,

the materials for the bulk should:

- have very low optical loss at the wavelength of the laser light to minimize the heat deposited,
- have high thermal conductivity and low thermal expansion to minimize mechanical distortion when heat is deposited in it by the laser beam,
- have a low rate of change of refractive index with temperature to minimize thermal lensing effects for transmitted laser beams,
- be suitable for polishing and coating to sub-angstrom surface roughness,
- be capable of being produced in suitable size, to reduce radiation pressure noise,
- have oxidised aluminum or silicon in their makeup so that they can be hanged to suspension through silicate bondings;

the materials for the coating should:

  - have thermoelastic properties that match with the substrate ones, to minimize mechanical distortion when heat is deposited in it by the laser beam,
  - have a low value of change of refractive index w.r.t. temperature to minimize thermorefractive noise,
  - be capable of being deposited in quarter-wavelength layers;

- the materials for the suspension should:
  - have high thermal conductivity and low thermal expansion to minimize the thermoelastic damping,
  - be capable of being produced in suitable shapes (ribbons or fibres),
  - have oxidised aluminum or silicon in their makeup so that they can be attached to test masses through silicate bondings.

Good candidate materials for mirror bulks can be very pure glasses such as fused quartz and fused silica or single-crystal materials such as sapphire and silicon. For the coating there are researches on Al_2O_3/Ta_2O_5, SiO_2/Ta_2O_5 and SiO_2/TiO_2-doped Ta_2O_5.

In this complex research context, finite element analysis can be a very useful tool in various steps of the modelization as it will be shown in chapter 5 through the work done by the candidate.

As far as suspensions are concerned, fused silica can be a good material: a lot of work has been done on it, and presently there is already a planning for bringing Virgo to an upgraded detector, called Virgo+, in which C85 steel wires will be replaced by fused silica fibres.

Silicon also is a very promising candidate: in chapter 6 its interesting features will be described, together with the experiments performed by the candidate in order to measure the loss angle of crystalline fibres, aiming at the possibility of using this new material for the suspensions of future 3rd generation GW interferometric detectors.

Chapter 5

Using finite element analysis

In the general framework of calculating thermal noise in composite system, the finite element analysis (FEA) can play a central role. The power of FEA resides on the possibility of facing many different problems connected with the behavior of complex systems. In many steps of the calculations that are necessary toward a complete thermal noise evaluation, FEA can give its support and, in some cases, it can allow to undertake problems otherwise impossible to solve.

In this chapter, first of all the FEA basis is introduced examining strong points and limitations of this approach. Then it will be discussed the application of FEA to an actual model of a Virgo mirror for calculating thermal noise with a direct method.

5.1 The basis of finite element analysis

The finite element method is a discretization process that, through the use of a mathematical model and numerical calculus techniques, allows the study of particularly complex problems. A solution is sought on the basis of fundamental equations governing the phenomena under investigation and through apposite approximations of the variables involved. The basic idea of FEA is quite simple and two separate steps can be identified:

- the *discretization* in which the structure is divided into *finite elements* with dimensions that bring to approximate the stress and strain fields within a certain error;
- the *building of the structure* in which all the single elements are assembled together, to solve the complete system so that
  - the stress and strain fields satisfy the continuity requirements on elements interfaces,
  - the internal stresses are in equilibrium, considering the applied loads and the boundary conditions.

In mechanical analyses of structures FEA can be used to face many different problems: linear and non-linear elastic, plastic, viscoplastic either static or stationary or dynamic. For a generic structural problem — whatever the geometry, the loads and the materials involved— three main conditions are always present:

- equilibrium condition:
  it relates the stress to itself and the applied forces. If the displacements are small, the equilibrium equations are linear;
- compatibility:
  it relates the strain to the displacements, in a geometric way. If the displacements are small the compatibility equations are linear;
- constitutive relation:
  it is an empirical law, as the elastic or the thermal one, that defines the constitutive equation of the system.

The software looks for a displacement field satisfying the above conditions. The found solution is not an exact one, but it gives a good approximation of the real one[1], in the analysis of problems for which obtaining the solution with the classical methods in an analytic way is, when possible, very difficult.

5.1.1 The principle of virtual displacements

The method adopted inside the FEA for solving the equilibrium equations is based on the principle of virtual displacements (PVD). The PVD states that if the system is subjected to a displacement field (arbitrary but compatible with the vincula) w.r.t. the equilibrium configuration, the work done by the internal forces equals the work done by the external ones. For a generic solid, subjected to the volume force F_i and to the surface force P_i, this means

$$\int_V \sigma_{ij} u_{ij} dV = \int_V F_i u_i dV + \int_S P_i u_i ds \ , \tag{5.1}$$

where u_i, σ_{ij} and u_{ij} are the displacements, the stress matrix and the strain matrix of the system respectively. Introducing in the previous equation the compatibility relation between the strain u_{ij} and the displacements u_i

$$u_{ij} = \frac{1}{2}(\partial_i u_j + \partial_j u_i) \tag{5.2}$$

and using the Gauss theorem in the form[2]

$$\int_V \big(\sigma_{ij}\partial_i u_j + u_j \partial_i \sigma_{ij}\big) dV = \int_S \sigma_{ij} u_j n_i ds \ , \tag{5.3}$$

it follows

$$\int_V u_i \big(\partial_j \sigma_{ij} + F_i\big) dV - \int_S u_i \big(\sigma_{ij} n_j - P_i\big) dS = 0 \ , \tag{5.4}$$

where n_i are the components of the unit vector normal to the surface of integration. Assuming $\boldsymbol{u}(\boldsymbol{r})$ is an arbitrary everywhere-continuous function, its

---

[1] The accuracy of such an approximation depends on the refinement of the mesh as it will be explained in § 5.1.4.

[2] An important requirement for the theorem to hold is that $\partial_i u_j$ and $\partial_i \sigma_{ij}$ are finite inside the volume V of integration, i.e. the fields σ and u are continuous.

coefficients must vanish in V and S to satisfy the previous relation, bringing to the equilibrium equations

$$\partial_i \sigma_{ij} + F_j = 0 \quad \text{in V and} \tag{5.5}$$

$$n_i \sigma_{ij} = P_j \quad \text{in S.} \tag{5.6}$$

The same equations can be obtained also imposing the system to be in a minimum of the potential energy. However, especially in the context of FEA, the PVD method reveals its power.

5.1.2 The elements

It is simple to solve integrals of known functions if an approximated method is used. This is the knot of the finite element method when it is used in a structure on which the displacements field is characterized by continuous but unknown quantities; the first step is to divide the structure into parts — *finite elements* — so tiny that they can suitably mock the real variation of the involved quantities.

The integral necessary to solve the structural problem can be substituted by a sum over functions evaluated on the elements. Therefore the finite element method can be simply viewed as a strategy to numerically solve integrals otherwise too complex — if not even impossible — to solve in a closed form. Moreover, for solving the integral, it is necessary to hypothesize the form of the displacements in the interior of each element: form functions are used to interpolate these values to obtain an everywhere defined solution to be used in the algorithm. Generally a simple kind of form function is used (linear or quadratic) and the precision of the solution is assured by the refinement of the mesh.

Element types

There are many types of elements that can be used, depending on the geometry of the system and on the kind of analysis that has to be performed.

The first thing characterizing an element is the dimensionality of the space in which it is immersed: it can be a 2-D or a 3-D space.

A 2-dimensional element is useful in problems in which the structure extends essentially on a plane and there are no stresses in the orthogonal direction. It can also be used for modeling structures in which there is a rotational or translational symmetry along one axis. In these kinds of model the analysis is performed on one section only, introducing *ad hoc* boundary conditions to take into account the actual behavior of the whole structure.

In all the other cases — and this also happens in the work performed in this thesis — elements in 3 dimensions are used. They divide into various categories depending on the dimensionality of the internal structure of the element itself:

- **line** elements. They are used to model strings, bolts, preloaded bolts, tubular members or any long, slender members where only membrane and bending stresses are needed. They have 2 or 3 nodes.

- **shell** elements. They are used to model thin panels or curved surfaces. The definition of thin depends on the application but, as a general guideline, the major dimension of the shell structure should be at least 10 times its thickness. They have a rectangular shape — with 4 or 8 nodes —, that can degenerate to a triangular one.

- **solid** elements. They are used for structures which — because of geometry, materials, loading or detail of required results — cannot be modeled with simpler elements. They are also used when the model

> geometry is transferred from a 3-D CAD system and a large amount of time and effort is required to convert it to a 2-D or shell form. They have a brick shape — with 8 or 20 nodes —, possibly degenerating into tetrahedrons, pyramids and prisms, or a tetrahedral shape — with 8 nodes —.

Each element is associated with a set of values that defines the degrees of freedom w.r.t. which the FEA has to be solved. A thermal element type, for example, has one d.o.f., which is the temperature, whereas a structural element type may have up to six d.o.f., i.e. three translations and three rotations. The most commonly used element types of the finite element software `ANSYS`®`8.1` [103] are reported in table 5.1. All the reported elements are good for describing the behavior of linear materials; element types with a star must be used for non-linear analysis. Elements PLANE2 and SOLID92 have a triangular and a tetrahedral shape respectively. Element SHELL99 is designed for shells composed of a great number of layers (up to 250).

	2-D Solid	3-D Line	3-D Shell	3-D Solid
Linear	PLANE42*	BEAM4 BEAM188	SHELL63 SHELL181*	SOLID45 SOLID185*
Quadratic	PLANE82* PLANE2	BEAM189	SHELL93 SHELL99	SOLID95 SOLID92 SOLID186*

Table 5.1: Commonly used structural element types of `ANSYS`® software. Stars indicate elements suitable for non-linear analyses.

5.1.3 The mesh

Half of the efforts in doing a FEA concerns the realization of a good finite element model.

After choosing the various element types and after defining the actual properties of the involved materials, the model has to be divided into a sort of grid, called *mesh*: each element is assigned a definite part of space and close elements are related to each other in the required way. In the last years a lot of improvements have been done in order to supply routines that automatize as much as possible this step of the modeling. The program has a specific engine, the mesher, that decides on an optimal disposition for the elements.

It is up to the user to pilot the mesh toward the desired configuration. If the mesher is run without any particular setting, it will generally construct a mesh of nearly identical in volume elements by using tetrahedral ones for the volumes and triangular ones for the areas. The user has many ways of modifying the building of the mesh, in order to optimize the extraction of the needed quantities, to simplify the application of boundary conditions and to reach the required level of precision for output results. He can choose that elements volumes are in a particular range and that lines or areas are divided into elements only in a certain number of parts or following a defined scheme. He can also modify the mesh after its constitution choosing to refine it at some locations.

5.1.4 Checking the FEA results

The hypothesized form functions introduced in § 5.1.2 could not represent what is happening really and approximation errors can occur, independently of what kind of element has been chosen for the FEA. Out of balance forces can appear among the applied loads and the reaction of the elements. This is why it is necessary to do ”sanity check” to make sure the solution is acceptable.

Generally it is very useful to verify if the results agree with hand calculation or experimental data, especially for the displacement solution, from which all the other results are derived. If this kind of calculation is not possible on the actual structure, it is possible to perform it on a model that embeds all the physical phenomena under consideration but that is simplified in the geometry (fewer objects of simpler shape).

The reaction forces should balance the applied loads and the mesh should be adequately refined. Criteria for understanding if the mesh is correct are described in the following.

Mesh error

The residual error can be physically interpreted as a continuous and artificial load — or constraint — that forces the element to maintain, e.g. in a structural analysis, the approximate deflection. If it is imagined to gradually remove this constraint and to leave the system moving toward the true equilibrium position, a positive work would be exerted by the applied forces. Therefore the elastic potential energy of the system increases releasing the constraints: the deformation energy of a structure, when it is an approximate solution obtained using the PVD, is less than the real deformation energy. The solution is called a *lower bound* solution and the structure can appear more rigid than the real one. By increasing the degrees of freedom, a convergence of the results toward the real value occurs. That phenomenon is referred to as *mesh convergence*. It is important to notice that the limit of the real value is on the mean of the total energy and not on the tension and displacements in a point; locally the tension could be higher than the real one.

The usual assumptions in FEA lead to a displacement field that is continuous on the elements and a stress field that is discontinuous. The element stress $\hat{\sigma}$ are obtained using the value inside the chosen element; the nodal stress σ^* are obtained as a mean among all the values of the elements concurring at the chosen node. The difference

$$\Delta\sigma = \sigma^* - \hat{\sigma} \ , \tag{5.7}$$

among element and nodal stresses is a value that can be easily computed in the post-processing and it gives a good indication of the suitability of the current mesh refinement. To define an error e_i of the mesh on the i-th element[3] it is possible to integrate the deformation work done by $\Delta\sigma$ on the i-th element volume V_i:

$$\|e_i\|^2 \doteqdot \frac{1}{2}\int_{V_i} \Delta\sigma_{ij} {E^{-1}}_{ik} \Delta\sigma_{kj} dV \ , \tag{5.8}$$

where E_{ij} is the elasticity matrix of the material. Therefore an estimation of the percentage error e_{tot} on a series of selected elements is given by[4]

$$e_{\mathrm{tot}} = 100\% \left(\frac{\sum_i \|e_i\|^2}{\sum_i \|u_i\|^2 + \sum_i \|e_i\|^2} \right)^{\frac{1}{2}} \ , \tag{5.9}$$

where $\|u_i\|^2$ is the deformation energy of the i-th element. As a general rule of thumb, e_{tot} should be under 10%. The elements of the structure where this threshold is overtaken are good candidates for a mesh refinement[5].

Another way to check mesh adequacy is to plot the element stresses and look for elements with high stress gradients.

5.2 FEA as a general tool in thermal noise studies

Finite element analysis is a very useful tool in solving several theoretical and experimental problems in the framework of thermal noise studies. A list of various cases in which FEA can be used is here shown.

---

[3] This value in `ANSYS`® is called SERR.

[4] This value in `ANSYS`® is called SEPC.

[5] Since the quantity e_{tot} is always highest at stress singularities, it is necessary to unselect the relative elements before investigating the error distribution.

5.2.1 Resonance modes extraction

Frequency and shape of resonance modes of a system can be extracted performing a modal analysis on its finite element model. There are many practical situations in which such kind of analysis can be very useful.

Ring-down experiments

In a class of experiments aiming at measuring quality factors of materials, the ring-down technique is used. The quality factors Q are extracted using $Q = \omega_r \tau / 2$, performing measurements on the time decaying constant τ in ring-down of oscillations at the various resonance frequencies ω_r of the system.

Therefore, especially for quite complex systems, for which the analytical calculation is not straightforward, it is useful to know the exact values of the resonances in order to excite them without losing time in looking for them. In fact, if the quality factor of the resonator is very high the spectral amplitude of its resonances is very sharp and it can be difficult finding them with a white noise or a swept-sine excitation.

The strain energy $\mathcal{E}$ of each mode can be expressed as [30]

$$\mathcal{E} = \mu \int_V (u_{ik} - \frac{1}{3}\delta_{ik}u_{ll})^2 d^3r + \frac{1}{2}K \int_V u_{ll}^2 d^3r = \mathcal{E}_{\text{sh.}} + \mathcal{E}_{\text{h.c.}} \,, \tag{5.10}$$

where the integrals have to be performed on volume V of the sample. The first addendum of (5.10) is due to a pure shear (distortion without volume change) and the second to hydrostatic compression (volume change without shape modification). The quantities K and μ are called modulus of hydrostatic compression and modulus of rigidity respectively and they are related to Young's modulus E and Poisson's ratio σ by

$$\mu = \frac{E}{2(1+\sigma)} \,, \tag{5.11}$$

$$K = \frac{E}{3(1-2\sigma)} \,. \tag{5.12}$$

It can happen that the quality factor is related to whether the energy is stored in compression or shear. With a FEA it is possible to compute, from the strain distribution of each mode, the compression part and shear part of the strain energy.

Interferometer read-out

In interferometer mirrors like the ones used in Virgo only certain modes give a non-zero contribution to the effective displacement read through the laser beam. The gaussianity of the laser-beam profile makes the interferometer almost insensible to mirror surface movements relative to modes that have radial node-lines: during an oscillation the shortening of the light path happening on one side of the nodal line is exactly compensated by the lengthening happening on the other. Therefore it is important to identify the modes that can represent, with their excitation, a noise for the interferometer.

In § 5.4.1 there will be shown the analysis done with a FEA on the resonances of a mirror like the one used in Virgo.

5.2.2 Shape parameter extraction

As explained in § 3.2.3, superficial losses could be dominant in ring-down experiments and they depend on geometries and mode shapes. The size of the effect is described by (3.57), in which a correct calculation of μ becomes crucial for a precise estimate of the superficial losses. According to [37]

$$\mu = \frac{V}{S}\frac{\int_S u_{ik}^2(\boldsymbol{r})d^2r}{\int_V u_{ik}^2(\boldsymbol{r})d^3r}\,, \tag{5.13}$$

where S, V and $u_{ik}(\boldsymbol{r})$ are the surface on which the dissipation occurs, the volume of the sample and the strain induced by the considered mode at the position $\boldsymbol{r}$ on the sample. This calculation, especially for higher modes and for complex sample shapes, can be hard to perform. In § 5.4.2 FEA will be used to calculate the parameter μ in the case of a mirror like the one used in Virgo.

5.2.3 Brownian thermal noise in complex systems

Nowadays, as it was explained in § 3.3.3, the most used technique for thermal noise calculation is Levin's direct approach. Numata [18] was the first to use this approach in combination with a FEA performed to calculate the mean dissipated energy to be used in Levin's formula (3.104). He did the analysis for an axisymmetric mirror including the loss of a 1-layer coating and, separately, of the magnets. In § 5.4.3 there will be shown how to perform a complete analysis of the mirror as a whole, including the presence of a multilayer coating, magnets, spacers and markers. The result obtained for the north-input (NI) and the north-end (NE) mirrors of the Virgo interferometer will be shown. It is the first time that such an analysis has been performed.

5.2.4 Parametric analyses

Thanks to detailed finite element models like the one developed hereafter for the mirror, it is possible to perform calculations previously impossible, investigating behaviors of the thermal noise budget w.r.t. arbitrarily chosen variables. That is very important because, on following the same scheme of finite element model creation, it will be possible, during the design phase of the future mirror, to chose the most suitable configuration for minimizing thermal noise contributions.

As an example, in § 5.4.4 there will be analyzed the effect of markers position on the thermal noise of the silicate bonding layer used to attach markers on the mirror surface.

5.2.5 Analysis on thermoelastic noise

In § 3.2.2 the thermoelastic damping process has been introduced and in § 4.1.2 and § 4.2.2 its effect on the bulk and the coating thermal noise has been reviewed. Following the method introduced by Liu and Thorne [56] and described in § 4.1.2 on page 67, the thermoelastic noise can be evaluated once the average dissipated power W_{diss} is known. It is possible to calculate W_{diss} through a finite element analysis using thermal elements associated with the structural ones but, because of the complexity of the problem and the lack of a specific `ANSYS`® element type, an actual calculation on realistic mirrors has not been performed yet.

In chapter 6 it is shown how a FEA can enter the study of thermoelastic noise in crystalline silicon fibres.

5.3 Finite element model of a Virgo mirror

The first step of a FEA on a Virgo mirror is the construction of a finite element model. The `ANSYS`®`8.1` [103] finite element software was used and the analysis is performed on the mirrors of the north-arm Fabry-Perot cavity which will be referred to as north input (NI) and north end (NE). For a complete modelization, all the components of the mirror used in the actual interferometer should be implemented: bulk , coating, magnets, markers and spacers.

5.3.1 The bulk

It consists of a single fused silica cylinder 350 mm in diameter and 96 mm thick for both NE and NI mirrors. NI mirror is made of Suprasil and NE of Herasil. The lateral surface is filed in order to obtain rectangular flat areas for spacer settlement. The volume is modelized with tetrahedral SOLID92 elements created with a free-mesh after the mesh of all the other components. In this way the mesher is forced to create transition zones between the high-definition regions and the low-definition ones.

5.3.2 The coating

It consists of alternating layers of Ta_2O_5 and SiO_2, materials with high and low refractive indexes respectively. On the NI the coating diameter is 100 mm and on the NE it is 280 mm because the transversal dimension of the resonant mode increases along the Fabry-Perot cavity reaching its maximum at the NE mirror. The composition of the two coatings for the mirrors are reported in table 5.2. The NI has four extra layers on the surface; their specifications are reported in table 5.3. The mesh is driven in a particular shape in order to simplify and optimize the application of a pressure with a Gaussian profile. First of all a series of circular lines is created with a definite spacing factor,

Type	Thickness	# of layers	
		NI	NE
High	130.4 nm	17	4
Low	182.2 nm	18	4

Table 5.2: Coating layer constitution for the two mirrors.

NI extra layers		
Type	Thickness	# of layers
High	100.8 nm	1
Low	252.7 nm	1
High	121.0 nm	1
Low	539.1 nm	1

Table 5.3: Characteristics of the four extra layers of the NI mirror.

in order to have a better spatial resolution in the central area. These lines, together with 4 other radial straight lines, identify a set of areas (figure 5.1 a). Secondly the mesher is forced to follow a definite pattern of line division for the node creation (figure 5.1 b). Finally the mesh is created using SHELL99 elements (figure 5.1 c). In the central part of the coating the mesh is simply completed with triangular elements in order to have only 7 extra nodes (see figure 5.2).

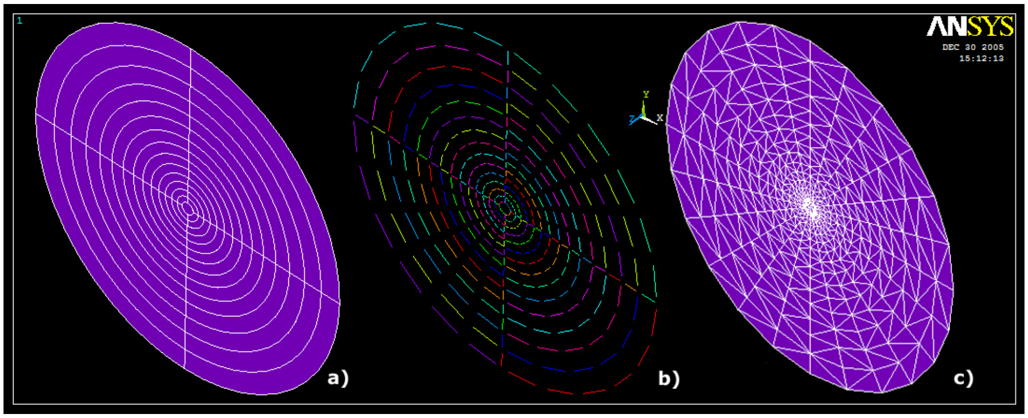

Figure 5.1: Steps of the mesh-driving procedure followed for creating the shell element of the coating on the mirrors. Area creation (a), lines division forcing (b), mesh with SHELL99 elements (c).

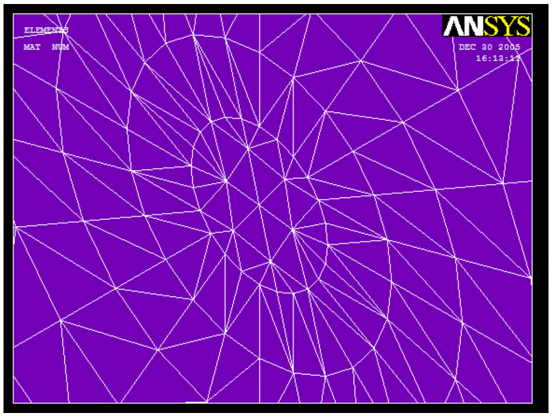

Figure 5.2: A magnification of the central part of the coating mesh. Only 7 nodes are added to complete the coating model.

5.3.3 Magnets, markers and spacers

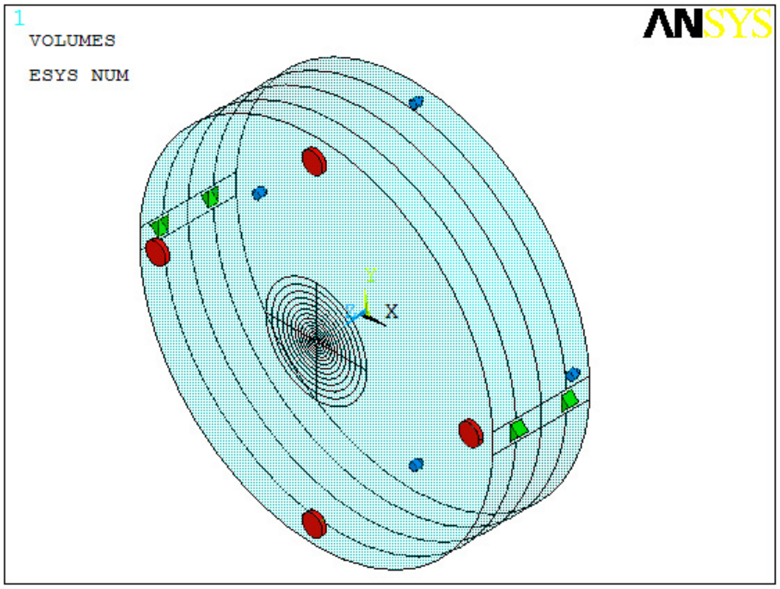

Figure 5.3: A view of the various components on the mirror: magnets (in blue), markers (in red) and spacers (in green).

Magnets: they are four elements (blue colored in figure 5.3) attached to the backside of the mirror and they consist of two parts: a cylindric support made of SiO_2 and a cylindrical magnet (simulated with a material with the same properties as C85 steel). A view of a meshed magnet is shown in figure 5.4a.

Markers: they are located on the front-side of the mirror, external to the coating and they are four simple cylinders made of SiO_2 (red colored in figure 5.3). A view of a meshed marker is shown in figure 5.4b.

Spacers: they are four prisms (green colored in figure 5.3) with a triangular base, attached along a lateral face on the flattened area of the mirror lateral side. A view of a meshed spacer is shown in figure 5.4c.

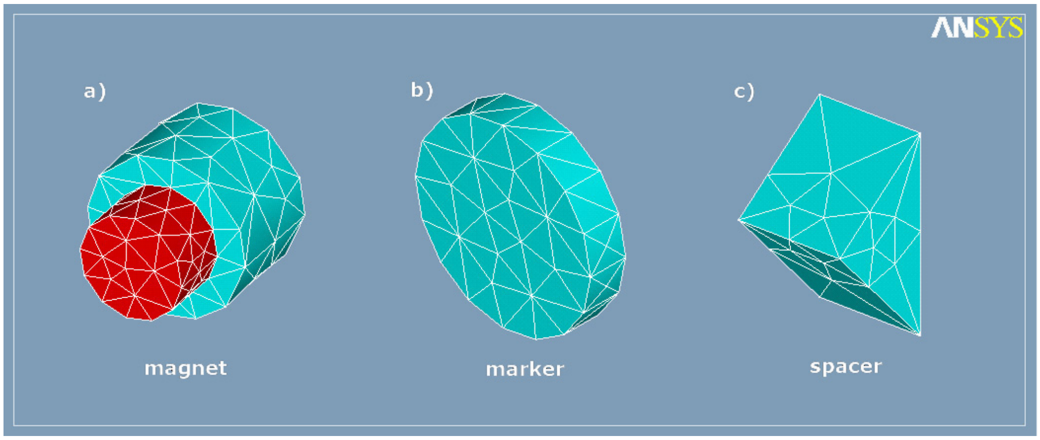

Figure 5.4: A view of a meshed magnet (a), marker (b) and spacer (c).

Silicate bonding areas: magnets, markers and spacers are attached to the bulk by means of the silicate bonding process. The interface region is modeled with SHELL99 elements formed by a 100 nm thick layer of SiO_2.

The characteristics of the materials used are reported in table 5.4 A view of the complete NI mirror is shown in figure 5.5.

Material	ρ [kg/m^3]	E [GPa]	σ
SiO_2	2202	73.2	0.164
Ta_2O_5	8316	140	0.23
C85	7900	200	0.3

Table 5.4: Characteristics of the materials used in the simulation: density ρ, Young's modulus E and Poisson's ration σ.

5.4 Application of FEA to a Virgo mirror

Hereafter, using the model of the Virgo mirror described in § 5.3, there will be a review of the FEA's performed by the candidate in the various research

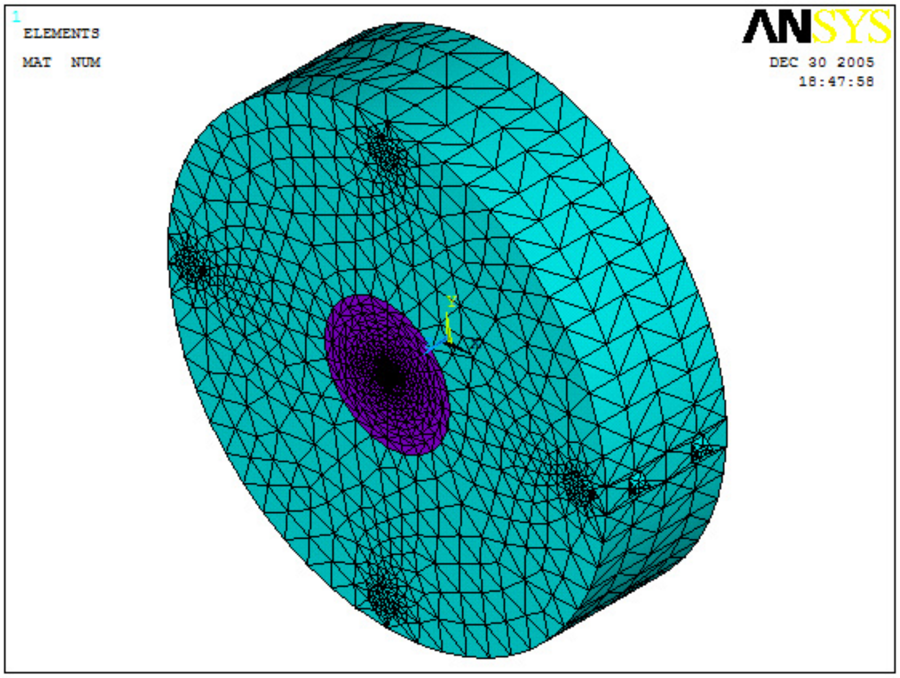

Figure 5.5: A view of the complete finite element model of the NI mirror.

areas anticipated in § 5.2.

5.4.1 Resonance modes extraction

A modal analysis has been performed on the finite element model of the mirror described in § 5.3. A plot of the found resonances w.r.t. the sequential mode number is shown in figure 5.6 to give an idea of the plethora of modes that characterizes this system. It is interesting to analyze the shape of the resonance modes.

The modes can be catalogued depending on oscillation-directions of the system points (along $\hat{x}$, $\hat{y}$, $\hat{z}$ working in Cartesian coordinates or $\hat{r}$, $\hat{\vartheta}$, $\hat{z}$ in cylindric ones or $\hat{r}$, $\hat{\vartheta}$, $\hat{\varphi}$ in spherical ones). The choice of the coordinate system depends on the easiness of the mode-pattern description. If not specified otherwise, the cylindric coordinate system will be used. Each pure mode is

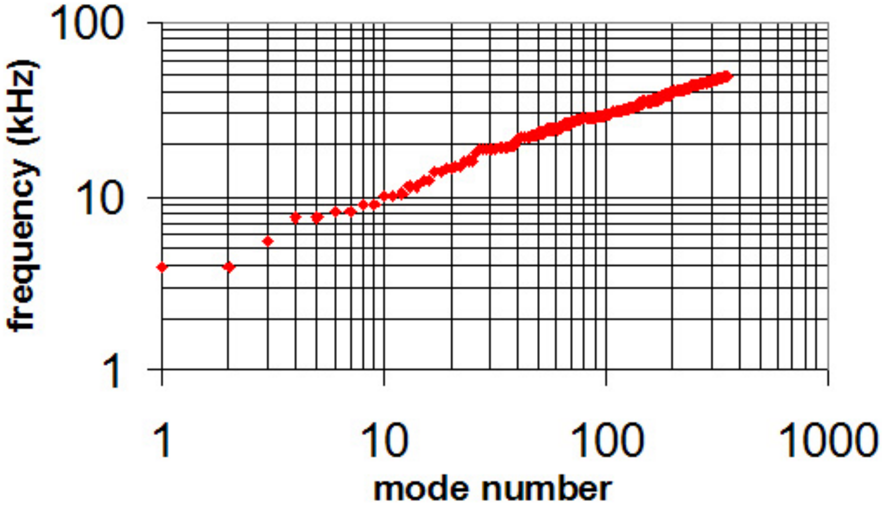

Figure 5.6: Resonance mode frequency of the NI mirror versus the sequential mode number, plotted for the first 356 modes.

labeled with a capital letter, indicating the oscillation direction, and by a set of three numbers indicating the behavior of the oscillation (which is simply related to the number of the nodal planes) along the three coordinate directions. For example, $Z_{r,\vartheta,z}$ refers to a mode along $\hat{z}$ with r nodal cylindric surfaces $\perp \hat{r}$, with ϑ nodal radial half-planes[6] $(\perp \hat{\vartheta})$ and z nodal planes $\perp \hat{z}$.

In 2-D and 3-D, objects generally do not produce pure modes, because they couple with modes along orthogonal directions having other kinds of symmetry. For example (see figure 5.7), consider the first mode of the mirror in cylindrical coordinates called butterfly mode: it is practically a pure $Z_{0,2,0}$ but it is slightly coupled with $R_{0,2,1}$ and $\Theta_{0,2,1}$ modes, which are along orthogonal directions w.r.t. $\hat{z}$ and with a $(r = 0, \vartheta = 2, z = 1)$ symmetry. Sometimes the coupling is very high and all the pure concurring modes are

---

[6] The nodal surfaces for $R_{r,\vartheta,z}$ and $\Theta_{r,\vartheta,z}$ are the same as for $Z_{r,\vartheta,z}$ with the exception of r label of Θ, which corresponds to $r/2$ cylindrical surfaces for r even and to $(r-1)/2$ cylindrical surfaces for r odd.

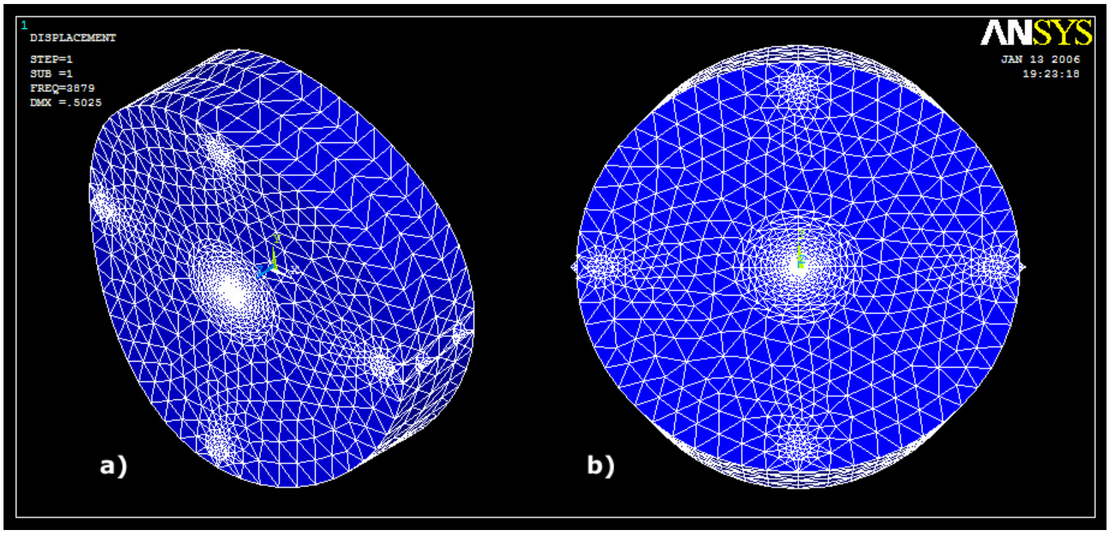

Figure 5.7: The first mode of the NI mirror in a three-quarter view (a) and in a front view (b). It is evident that the motion is mainly along $\hat{z}$ but that it slightly couples with movements along $\hat{r}$ and $\hat{\vartheta}$.

strongly present. See, e.g., the 6th mode (figure 5.8): the two pure modes $R_{0,2,0}$ and $\varTheta_{1,2,0}$ are both present as shown in the diagram of figure 5.9 a.

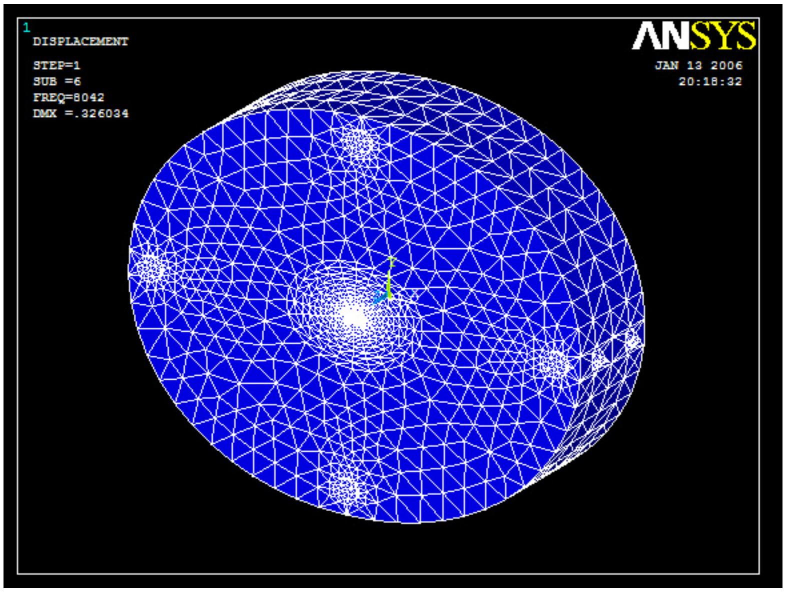

Figure 5.8: Three-quarter view of the 6th mode of the NI mirror.

Whatever the coupling is, the resulting symmetry is the composition of

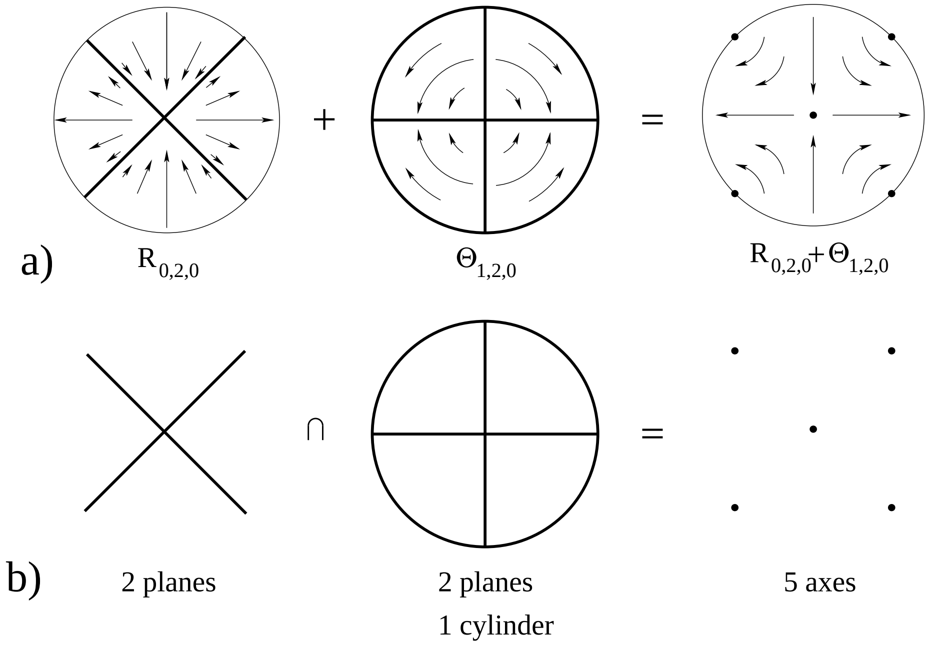

Figure 5.9: Diagram of the superimposition of the $R_{0,2,0}$ and $\Theta_{1,2,0}$ pure modes forming the 6th mode. Nodal surfaces are indicated with thick lines, nodal axes with thick points (a). The composition of the nodal surfaces is shown, giving birth to 5 nodal axes (b).

the pure-mode symmetries. In figure 5.9 b the composition of the 2 pure-modes symmetries is shown for the 6th mode. The intersection among the mode nodal-surfaces is taken, resulting in 5 nodal axes.

In table 5.5 the pure modes constituting the first 41 modes of the FEA mirror are reported (the bold font indicates the dominant ones). Some modes appear on the same row because they go into each other[7] with a rotation along $\hat{z}$.

---

[7] This is not strictly true because of the presence of magnets, markers and spacers that break this symmetry. By the way, the the modes are so slightly different from each other that the two frequencies are nearly equal and it makes sense to consider them part of the same doublet.

Mode number	Pure modes			Frequency	$\frac{\mathcal{E}_{\text{h.c.}}}{\mathcal{E}_{\text{tot}}}$	z_{out}	Name
1,2	$R_{0,2,1}$	$\Theta_{1,2,1}$	$\boldsymbol{Z_{0,2,0}}$	3879, 3883	.106	7×10^{-4}	aB2
3	$R_{0,0,1}$	—	$\boldsymbol{Z_{1,0,0}}$	5544	.736	1	aD1
4,5	$R_{0,3,1}$	$\Theta_{1,3,1}$	$\boldsymbol{Z_{0,3,0}}$	7549, 7552	.197	1×10^{-6}	aB3
6,7	$\boldsymbol{R_{0,2,0}}$	$\boldsymbol{\Theta_{2,2,0}}$	$Z_{0,2,1}$	8042, 8048	.019	3×10^{-5}	sB2
8,9	$\boldsymbol{X_{1,1,0}}$	$\boldsymbol{Y_{2,0,0}}$	$Z_{0,1,1}$	9021, 9023	.458	5×10^{-8}	
10,11	$X_{2,4,1}$	$Y_{1,1,1}$	$\boldsymbol{Z^{r,\vartheta,z}_{1,1,0}}$	10121, 10124	.673	2×10^{-5}	
12	$\boldsymbol{R_{0,0,0}}$	—	$Z_{1,0,1}$	10379	.737	7×10^{-2}	sD1
13,14	$R_{0,4,1}$	$\Theta_{1,4,1}$	$\boldsymbol{Z_{0,4,0}}$	11308, 11321	.207	2×10^{-3}	aB4
15,16	$\boldsymbol{R_{0,3,0}}$	$\boldsymbol{\Theta_{2,3,0}}$	$Z_{0,3,1}$	12297, 12299	.103	7×10^{-8}	sB3
17,18	$\boldsymbol{R_{0,2,0}}$	$\boldsymbol{\Theta_{3,2,0}}$	$Z_{0,2,1}$	13900, 13926	.566	2×10^{-6}	
19,20	$R_{1,2,1}$	—	$\boldsymbol{Z_{1,2,0}}$	14434, 14465	.594	8×10^{-4}	
21,22	$R_{0,5,1}$	$\Theta_{1,5,1}$	$\boldsymbol{Z_{0,5,0}}$	15072, 15079	.205	2×10^{-5}	aB5
23	$R_{1,0,1}$	—	$\boldsymbol{Z_{2,0,0}}$	15606	.651	5×10^{-1}	aD2
24,25	$\boldsymbol{R_{0,4,0}}$	$\boldsymbol{\Theta_{2,4,0}}$	$Z_{0,4,1}$	15938, 15961	.154	1×10^{-2}	sB4
26	$R_{1,0,0}$	$\boldsymbol{\Theta_{2,0,0}}$	—	17647	.000	4×10^{-6}	
27,28	$R_{1,3,1}$	—	$\boldsymbol{Z_{1,3,0}}$	18412, 18415	.587	3×10^{-5}	
29,30	$\boldsymbol{X_{2,4,0}}$	$\boldsymbol{Y_{1,1,0}}$	$Z^{r,\vartheta,z}_{1,1,1}$	18620, 18622	.546	3×10^{-8}	
31,32	$R_{0,6,1}$	$\Theta_{1,6,1}$	$\boldsymbol{Z_{0,6,0}}$	18788, 18810	.194	6×10^{-4}	aB6
33,34	$\boldsymbol{R_{0,3,0}}$	$\boldsymbol{\Theta_{3,3,0}}$	$Z_{0,3,1}$	19106, 19115	.406	1×10^{-6}	
35,36	$X_{2,2,1}$	$Y_{1,1,1}$	$\boldsymbol{Z^{r,\vartheta,z}_{2,1,0}}$	19172, 19173	.516	3×10^{-5}	
37,38	$\boldsymbol{R_{0,5,0}}$	$\boldsymbol{\Theta_{2,5,0}}$	$Z_{0,5,1}$	19360, 19363	.179	8×10^{-7}	sB5
39	$R_{0,0,1}$	$\boldsymbol{\Theta_{0,0,1}}$	—	19719	.001	2×10^{-6}	aT1
40,41	$\boldsymbol{X_{1,1,1}}$	$\boldsymbol{Y_{2,0,1}}$	$Z^{r,\vartheta,z}_{1,1,1}$	21381, 21389	.285	5×10^{-6}	

Table 5.5: The first 41 mode frequencies of the FEA mirror are listed together with the pure modes forming them (the bold font indicates the dominant ones). The modes appearing in pairs are doublets, connected by simple rotations along $\hat{z}$. The 4th column reports the ratio between hydrostatic compression energy $\mathcal{E}_{\text{h.c.}}$ and total energy $\mathcal{E}_{\text{tot}}$ of the mode. In the 5th column the effective read-out displacement per unit of $\sqrt{\mathcal{E}_{\text{tot}}}$ is shown, referring it to 3rd-mode displacement. The last column indicates the common name of the mode: "B", "D" and "T" stand for "butterfly", "drumhead" and "torsional" respectively; "a" and "s" stand for asymmetric and symmetric.

Ring-down experiments

Frequencies obtained with FEA have to be considered reliable within 1‰; therefore they are very useful as a guide to find the resonances to be excited in a ring-down experiment. In table 5.5 the frequencies of the first 41 modes of the mirror are reported as obtained with a modal analysis performed with `ANSYS`®.

As explained in § 5.2.1, if the damping of the modes can depend on how the energy is distributed between shear and compression, it is relevant to calculate these quantities for each mode. Shear energy $\mathcal{E}_{\text{sh.}}$ and hydrostatic compression energy $\mathcal{E}_{\text{h.c.}}$ are obtained by the integrals over mirror volume defined in (5.10). Obviously in FEA these integrals reduce to a sum of products among volumes V_n and strain components $u_{ij,n}$ of each element:

$$\mathcal{E}_{\text{sh.}} = \mu \sum_n (u_{ik,n} - \frac{1}{3}\delta_{ik} u_{ll,n})^2 V_n = \mu \sum_n (u_{ik,n}^2 - \frac{1}{3} u_{ll,n}^2) V_n \; , \tag{5.14}$$

$$\mathcal{E}_{\text{h.c.}} = \frac{1}{2} K \sum_n u_{ll,n}^2 V_n \; , \tag{5.15}$$

where μ and K are defined in (5.11) and (5.12). These values were calculated from `ANSYS`® output, using `AWK` [104], a pattern-directed scanning and processing language.

In table 5.5 the ratio between $\mathcal{E}_{\text{h.c.}}$ and the total energy of the mode is reported. This value is almost zero (energy completely stored in shear) for the torsional modes (e.g. 26^{th} and 39^{th}), it is below 0.2 for the butterfly modes and it is distributed around 0.6 for the others, with the highest values of over 0.7 for the first drumhead modes, indicating a great hydrostatic compression.

Interferometer read-out

As regards the influence of mirror resonances on interferometer read-out, it is possible to calculate, for each mode, the neat displacement read by the

Gaussian laser beam at the maximum of oscillation. The beam profile is simulated with forces F_n acting on the mirror-coating nodes reproducing a Gaussian pressure-profile as it will be explained in § 5.4.3. The effective displacement z_{out}, normalized to the displacement of the 3rd mode, is obtained for each mode by the coating-nodes displacements z_n using

$$z_{\text{out}} = \frac{\sum z_n F_n}{\sqrt{E_{\text{tot}}}} \frac{\sqrt{E_{\text{tot},3}}}{\sum z_{n,3} F_{n,3}} \, , \tag{5.16}$$

where E_{tot} is the total energy stored in the mode and the index "3" refers to the 3rd mode. The factor $\sqrt{E_{\text{tot}}}$ is necessary to consider modes as having the same stored energy; the square root takes into account that energy is a quadratic form of displacements.

The obtained values, referred to the 3rd-mode displacement, are listed in table 5.5: it is evident that among the first 41 modes the most contributing ones are the three drumhead aD1, sD1, aD2, followed — two orders of magnitude further down — by the butterfly modes.

5.4.2 Shape parameter extraction

In § 5.2.2 the importance of the shape parameter μ defined by (5.13) has been stressed. A FEA has been performed to calculate this parameter from the element strain distribution.

The particular conformation of the actual mirror forces to consider two distinct sources of superficial damping: the coating surface and all the other uncoated surfaces. Therefore (3.56) now becomes

$$\frac{\Delta\mathcal{E}_{\text{surf}}}{\Delta\mathcal{E}_{\text{bulk}}} = \frac{\Delta\mathcal{E}^{c}_{\text{surf}}}{\Delta\mathcal{E}_{\text{bulk}}} + \frac{\Delta\mathcal{E}^{uc}_{\text{surf}}}{\Delta\mathcal{E}_{\text{bulk}}} = \mu^c d^c_s \frac{S^c}{V} + \mu^{uc} d^{uc}_s \frac{S^{uc}}{V} \, . \tag{5.17}$$

where the notation is the same as in (3.56) and the superscripts "c" and "uc" refer to coated and uncoated surfaces respectively. In order to calculate μ^c and μ^{uc} with formula (5.13), superficial strain energy density for coated and uncoated surfaces is needed. `ANSYS`® software does not allow access to superficial densities directly, but for the coated surface the strain is almost constant through the coating SHELL elements, in the direction normal to the surface, so that

$$\frac{\int_{S_c} u_{ik}^2(\boldsymbol{r}) d^2r}{S_c} \simeq \frac{\int_{V_c} u_{ik}^2(\boldsymbol{r}) d^3r}{V_c} = \frac{\sum_n u_{ik,n}^2}{\sum_n V_n} , \tag{5.18}$$

where the integral in the numerator has moved from the coating surface to the coating volume and finally it has become a simple sum over the coating elements. As regards the uncoated surfaces, the finite element model of the mirror has been slightly modified covering them with a layer of fused silica 0.1 μm thick.

In table 5.6 the calculated μ^c and μ^{uc} parameters for the first 41 modes of NI and NE mirrors are reported. The values for μ^c are more variable (from 0.0 to 6.7) w.r.t. the ones for μ^{uc} (from 0.4 to 2.3). This is due to the fact that μ^c is extremely sensitive to modes that, for their particular shape, have a lot of energy in the center of the mirror; on the other side μ^{uc} mediate on a larger surface, with parts either near or far w.r.t. the center of the mirror. Moreover, focusing on μ^c, low values (below 2) for the NI mirror systematically correspond to higher values for the NE one and vice-versa, except for the 10th and 11th modes. This is related to the different coating radius (28 cm for NE and 10 cm for NI) that allows the parameters to be more or less sensitive to the energy stored in the center or the peripheral parts of the mirror.

5.4.3 Brownian thermal noise calculation

Brownian thermal noise calculation for the NI and NE mirror of Virgo experiment has been performed using FEA. The formula (3.104), reported also

Mode number	μ^c		μ^{uc}	
	NI	NE	NI	NE
1,2	6.70	4.68	1.89	1.29
3	10.50	5.26	1.68	1.11
4,5	1.02	3.71	2.06	1.49
6,7	4.46	2.03	0.60	0.37
8,9	0.28	1.22	1.06	0.87
10,11	2.68	4.58	1.55	0.92
12	2.77	1.79	0.70	0.49
13,14	0.16	3.05	2.13	1.65
15,16	1.03	1.94	0.80	0.51
17,18	0.83	0.82	1.26	1.15
19,20	1.49	3.88	1.48	0.93
21,22	0.03	2.57	2.22	1.81
23	5.18	4.13	1.32	0.80
24,25	0.20	1.85	0.98	0.69
26	0.20	1.83	0.66	0.37
27,28	0.55	3.17	1.48	1.01
29,30	0.96	1.64	0.56	0.34
31,32	0.00	2.20	2.32	1.96
33,34	0.26	0.57	1.32	1.23
35,36	3.17	1.99	0.69	0.45
37,38	0.04	1.75	1.16	0.88
39	0.00	0.00	0.73	0.73
40,41	0.34	0.49	1.06	0.99

Table 5.6: Shape parameters for the coated (μ^c) and uncoated (μ^{uc}) surfaces of NI and NE mirror for the first 41 modes.

here for clarity,

$$S_X(\omega) = \frac{8k_BT}{\omega^2}\frac{\langle W_{\text{diss}}\rangle}{F_0^2} \; , \tag{5.19}$$

gives the power spectrum of the Brownian thermal noise $S_X(\omega)$ from the average dissipated power W_{diss} by the mirror subjected to a pressure distribution (of total force F_0) that mocks the laser power profile, as explained in

§ 3.3.3.

Virgo laser has a total power $P_0 = 20$ W, distributed with a Gaussian profile $P(r, \vartheta)$ expressed by

$$P(r, \vartheta) = \frac{P_0}{\pi r_0^2} e^{-\frac{r^2}{r_0^2}} , \tag{5.20}$$

where r_0 is the beam radius related to the beam waist w_0 by $w_0 = \sqrt{2} r_0$ (on the NI $w_0 = 2$ cm, on the NE $w_0 = 5.5$ cm). The coating has been meshed, as explained in § 5.3.2, in order to simplify as much as possible the application of the pressure profile, that is simulated with a set of forces acting on the corner nodes of the SHELL elements constituting the coating itself. These forces are scaled according to the effective area corresponding to each node on which they act. The parameter F_0 is simply obtained by the sum of all the applied forces.

`ANSYS`® software allows a harmonic analysis: all the applied forces are varied periodically with a function $\sin(2\pi f t)$ on a set of defined frequencies f and the solution of the dynamic problem is stored, for each frequency, in a result file. From (3.38) it follows that average the dissipated power $\langle W_{\text{diss}} \rangle$ is

$$\langle W_{\text{diss}} \rangle = \sum_i \langle W_{\text{diss},i} \rangle = 2\pi f \sum_i \mathcal{E}^{\max}_{\text{stor},i} \phi_i , \tag{5.21}$$

where the sum is intended over the various mirror parts (bulk, coating, magnets, markers, spacers) for which $\mathcal{E}^{\max}_{\text{stor},i}$ is the strain energy at maximum oscillation and ϕ_i is the loss angle, reported in table 5.7. Loss angle values for the mirror bulk are taken from [105] and for the coating from [106]. Magnets, markers and spacers dissipate through the silicate bonding layer connecting them to the mirror surface; silicate bonding loss angle is taken from the measurements done in [107]. Formula (5.21), plugged in (5.19), gives the total power spectrum of Brownian thermal noise as a sum of the various mirror-part contributions. In figure 5.10 these quantities are shown

	NI mirror bulk	NE mirror bulk	Coating	Silicate bonding
Material	Suprasil	Herasil	SiO_2/Ta_2O_5	SiO_2
ϕ	9.6×10^{-7}	5.5×10^{-7}	4×10^{-4}	10^{-2}

Table 5.7: Material and loss angle of the various mirror parts contributing to dissipation.

in strain sensitivity units[8]. For comparison it is plotted the prediction of Bondu, Hello and Vinet [54] corrected by Liu and Thorne [56] for an uncoated finite size mirror (see (4.9) on page 65): simulated Brownian thermal noise follows the theoretically predicted trend, being proportional to $\omega^{-1/2}$.

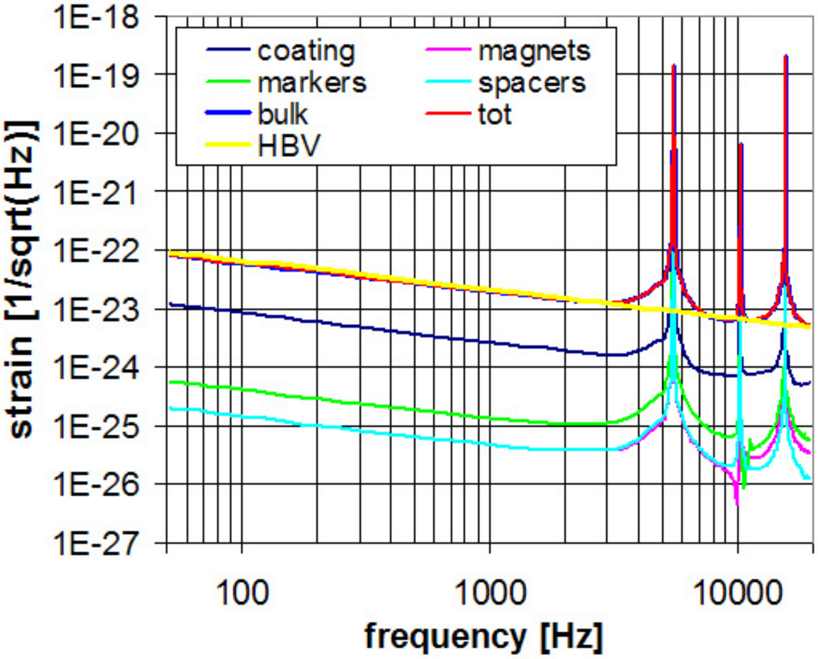

Figure 5.10: Brownian thermal noise for NI mirror. Contributions for the various mirror parts are highlighted by different colors. The yellow line indicates the prediction for and uncoated finite-size mirror made by Bondu, Hello and Vinet (with Liu and Thorne correction).

---

[8] It implies that, for a single-mirror noise, it is plotted the equivalent noise of the interferometer having, in the two Fabry-Perot cavities, 4 mirrors identical to it. For the definition of strain sensitivity units see on page 17.

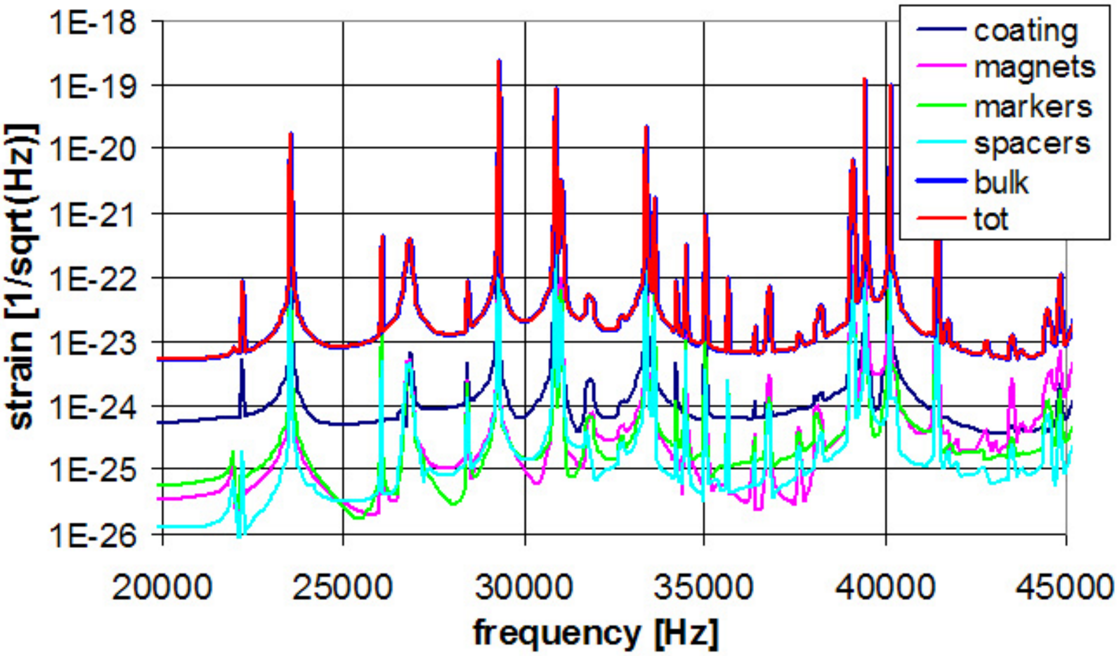

Figure 5.11: Brownian thermal noise for NI mirror in a linear frequency scale from 25 kHz to 45kHz. Contributions for the various mirror parts are evidenced with different colors.

Coating noise is about one order of magnitude lower w.r.t. bulk noise and, among the other contributions, the most relevant is the one due to markers. The big peaks correspond to the three drumhead modes (aD1, sD1 and aD2 with the notation of table 5.5); this is in agreement with the high values calculated on those modes for the read-out displacement z_{out}, listed in table 5.5. An enlargement of the frequency region from 25 kHz to 45 kHz is shown in figure 5.11. It is evident that with this analysis it is possible to compute directly the Brownian thermal noise in near-to-resonance regions, including the coupling effects induced by the inhomogeneous loss distribution.

In figure 5.12 it is shown a comparison among NI and NE mirror thermal noise in interferometer strain units. The factor of about 2 in the bulk contributions is due to the different loss angle of NI w.r.t. NE mirror (see

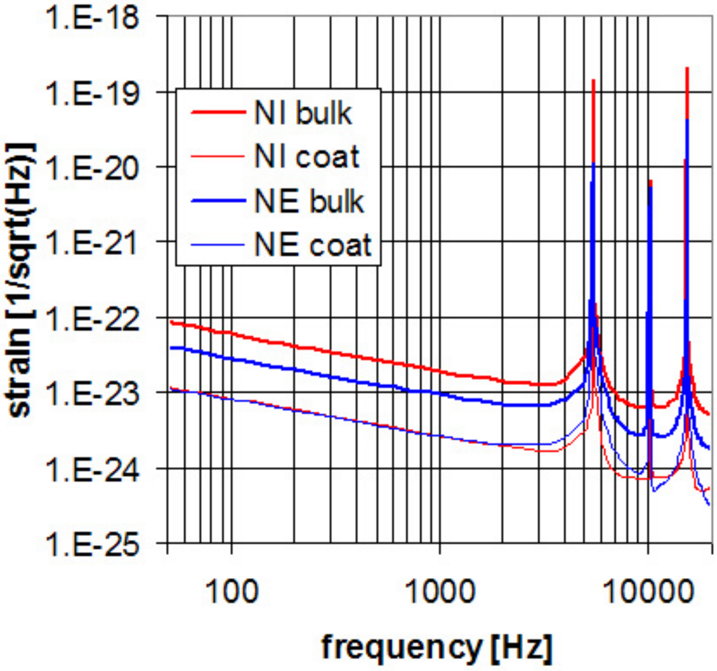

Figure 5.12: Brownian mirror thermal noise comparison among NI and NE mirrors for bulk and coating.

table 5.7). The coatings are contributing similarly with a little difference due mainly to their diameters (10 cm for the NI and 28 cm for the NE).

5.4.4 The effect of the markers

Calculations of the same kind as the ones described in the previous section have been performed on NI mirror in order to see the effect of marker position on Brownian thermal noise.

Markers are settled at a radial distance of 155 mm from the mirror center. This distance d has been varied from 155 mm down to 62 mm (a position in which they are almost touching the coating). A harmonic analysis has been performed in each configuration calculating the contribution of the markers to the Brownian mirror thermal noise at 100 Hz and at 600 Hz.

The results are shown in figure 5.13. It is evident the increment in thermal

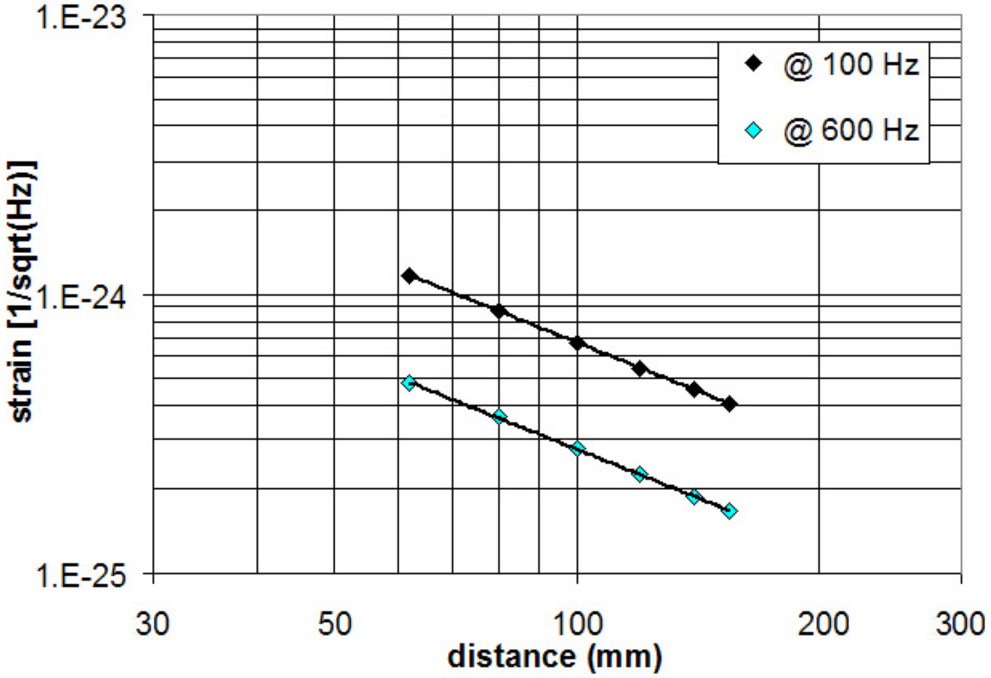

Figure 5.13: Marker contribution to Brownian mirror thermal noise as a function of the distance of the markers from the center. The analysis has been performed for two frequencies inside the Virgo band.

noise budget as the distance of the markers w.r.t. the center of the impinging beam decreases. This is in agreement with what expected because a source of loss nearer to the mirror axis can influence the read-out easier. The dependence is roughly linear in $1/d^{6/5}$ and is not influenced by the inspected frequency.

Chapter 6

Research on new materials for suspensions: characterization of silicon crystalline fibres

This chapter begins with a description of the interesting features of silicon as a material for mirror suspensions in interferometers of the 3$^{\text{rd}}$ generation. Then there will be the description of the experiment performed by the candidate in order to measure the loss angle of crystalline fibres. Finally, there will be an outline of the foreseen work on the same research line.

6.1 Silicon properties

Silicon thermal and mechanical properties are extremely favorable to reduce thermal noise in the optics suspensions of a GW interferometric detector. In the frequency range comprised between the pendulum resonance and the first violin mode of the suspension fibres, the power spectral density of the thermal noise displacement of a suspended mirror S_x^{pend} can be deduced by the formulas (4.42) and (4.41) with the approximation $\omega \gg \omega_0$:

$$S_x^{\text{pend}} = \frac{k_B T}{\omega^5} \frac{g}{l^2 c \sigma_b} \sqrt{\frac{gE}{mN\pi}} \phi(\omega) \ . \tag{6.1}$$

where the loss angle $\phi(\omega)$ represents the sum of all the dissipative processes that occur in the material (structural and thermoelastic losses) plus an effective loss angle for the losses associated with the connecting elements such as clamps, break-off points or chemical bonded pieces. Silicon is expected to have large bulk tensile strength (about 7 GPa, dominated by surface effects that can decrease the value down to about 200 MPa [108]) and comfortably low intrinsic loss angle — $\phi_i(300\text{ K}) \simeq 2.8 \times 10^{-8}$, $\phi_i(77\text{ K}) \simeq 5 \times 10^{-9}$ and $\phi_i(4.2\text{ K}) \simeq 6 \times 10^{-10}$ [36, 109, 110] —. The behavior of the linear thermal expansion coefficient α and of the thermal conductivity κ are peculiar[1] as displayed in figure 6.1.

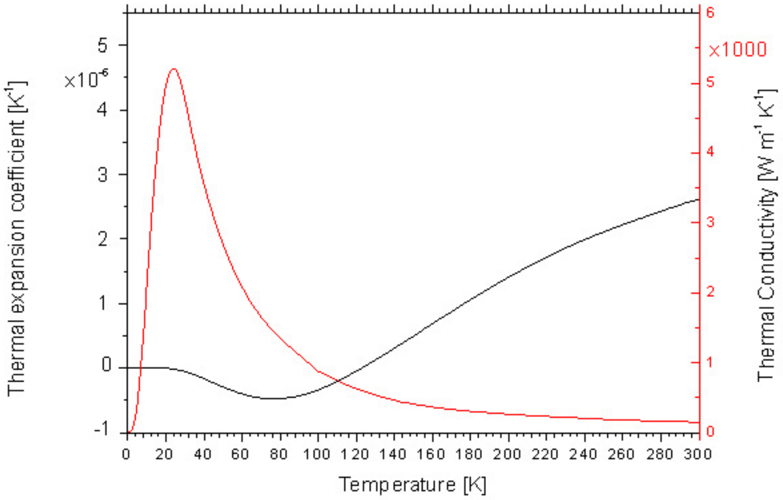

Figure 6.1: Linear thermal expansion coefficient and thermal conductivity of silicon; the two temperatures (about 18 K and 123 K), where the thermal expansion coefficient vanishes, and the peak of the thermal conductivity at low temperature are well evident.

The thermal expansion coefficient decreases with temperature until it vanishes at about 123 K, it is negative in the temperature interval 18÷123 K and almost zero at lower temperatures. This means that the thermoelastic dissipation decreases sharply with temperature and becomes negligible w.r.t.

---

[1] All the thermo-mechanical properties of silicon reported in this paragraph are taken from [111].

the structural losses in the range 120÷130 K and below 20 K as reported in figure 6.2.

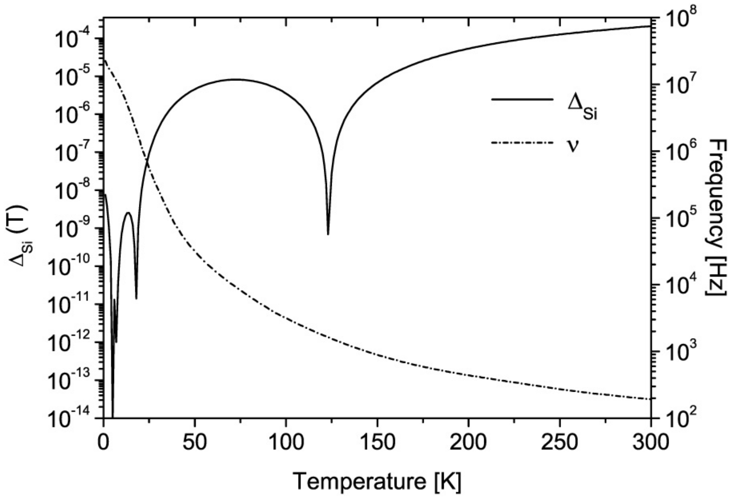

Figure 6.2: The amplitude of the linear thermoelastic loss angle in a silicon fibre, computed using (3.54) and [111] is shown with the solid line. Ideally, at the two temperatures where the thermal expansion coefficient vanishes ϕ_0 is null. The expected temperature dependence of thermoelastic peak frequency $1/\tau_{th}$ in a 560 μm diameter silicon fibre is also shown (dashed line). The increase at low temperatures should contribute to reduce the thermoelastic dissipation in the suspension.

The thermal conductivity κ of silicon increases at low temperatures pushing the thermoelastic peak toward higher frequencies according to equations (3.53) and (3.52). After reaching a maximum, the thermal conductivity drops as the phonon mean free-path becomes larger than the square root of the typical cross-section of the sample (see the red curve in figure 6.1). Note that the thermal conductivity varies greatly with the doping of the material and with the concentration of the lattice defects, so that the red curve of figure 6.1 ought to be taken as a qualitative representation of $\kappa(T)$.

It is worth to compare the thermoelastic losses in different materials. Almost all the present GW interferometric detectors use steel wires to suspend the main optics. This choice provides a convenient solution to keep in position (safely and easily) very expensive optics. In Virgo the wire steel (C85) [98] and the suspension design [112] have been selected to optimize the thermal noise control. The intrinsic loss angle of C85 has been measured to be about 2×10^{-4} at the best, while many crystalline materials (like sapphire or YAG) have intrinsic loss angles well below that value. However, these materials have not been considered for low thermal noise suspensions because of their large thermal expansion coefficient, which enhances their thermoelastic dissipation according to (3.53) and (3.54). The thermoelastic losses of different materials are compared in figure 6.3. For instance the advantage in using sapphire fibres is clearly nullified by the dominant thermoelastic loss angle at low frequency. On the contrary, fused silica has an intrinsic loss

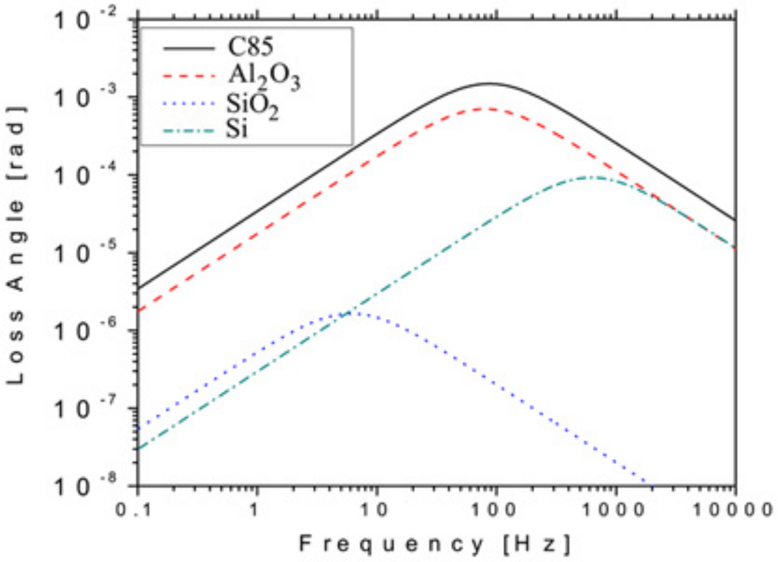

Figure 6.3: Expected thermoelastic peaks at room temperature (T=300 K) in fibres (560 μm in diameter) made of: C85 steel (solid curve) [98], sapphire (dashed curve) [111], fused silica (dotted curve) [98, 111] and silicon (dash-dotted curve) [111].

angle below $10^{-7} \div 10^{-8}$ (depending on the type of fused silica) and, more notably, its thermoelastic dissipation is suppressed by a small thermal expansion coefficient. Finally, figure 6.3 suggests that another material could be selected to realize low thermal noise suspension, namely crystalline silicon. In fact, silicon does have a large thermoelastic peak, but for very high frequencies. This is due to the high thermal conductivity of silicon. As a result, at low frequencies, where thermal noise in the suspensions dominates the noise budget of GW detectors, the thermoelastic dissipation in silicon fibres could be even lower than in fused silica fibres. This effect, together with its low intrinsic loss angle [109], singles out silicon as one of the most promising materials for low thermal noise suspensions in GW detectors.

6.2 Silicon fibres production

Silicon fibres were grown in a dedicated research facility of an INFM Pisa laboratory. There, a crystal growth furnace that uses the so-called micro pulling down technique (μ-PD) was set up. Basically the μ-PD method involves downward pulling of a crystal fibre through a micro nozzle placed at the bottom of the crucible as shown in figure 6.4. The method allows to grow crystals in shape of fibres, rods or ribbons with diameters ranging from 0.15 mm to 5 mm at widely variable pulling rates [113].

The melt is placed in crucibles made of materials stable at temperatures as high as the melting point of the target crystalline material. The crucibles are heated using a radio-frequency (RF) generator. At the first stage a crystal fibre seed, produced from previous experiments or cut from a bulk crystal of the corresponding material, is inserted into the crucible orifice. The seed is then pulled downward using a precise pulling mechanism. Normally the surface forces do not allow the melt to separate from the bulk material.

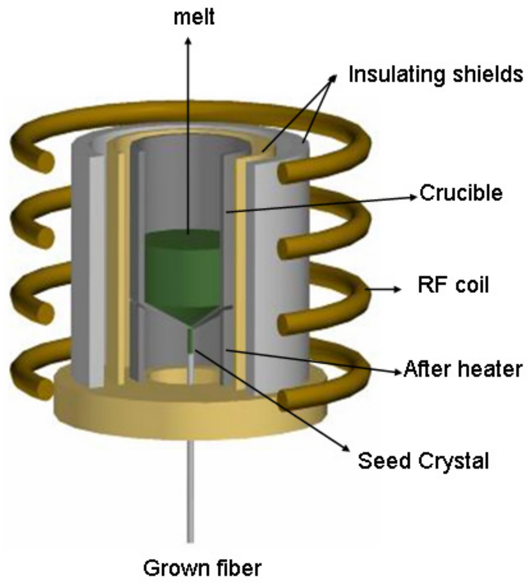

Figure 6.4: Schematic diagram for the μ-PD growth apparatus (hot zone part).

Therefore the melt passes through the nozzle at the bottom of the crucible and the new fibre is grown. Application of an after heater allows adjustment of the appropriate temperature gradients under the crucible and therefore regulation of the position of the solid-liquid interface in the vicinity of the crucible tip.

The shape and location of the growth interface are among the most important parameters determining the quality and uniformity of the resulting crystal. Therefore special attention is normally paid to monitor and detect the spatial distribution of the temperature gradient in the vicinity of the phase boundary. CCD camera and monitor are considered to be very good tools to view the solid-liquid interface and the meniscus region.

The furnace can be evacuated and an inert atmosphere can be inserted. It has been tested with several materials and about 20 silicon fibres have already been grown.

6.2.1 Growth process

The starting material was a 5-N-purity silicon in small pieces of a few millimeters. These pieces were inserted in a vitreous carbon crucible about 27 mm high and 18 mm in diameter; it was placed on an after heater of the same material and everything was held by a zirconate pedestal in a vertical alumina ceramic tube and was heated using a RF generator. Cylindrical heat shields made of alumina or zirconate ceramics were placed around the crucible as shown in figure 6.4.

The calibrated orifice made in the bottom of the crucible was about 0.5 mm in diameter. The crucible temperature was controlled by the power of the RF coil which is about 80 mm long and 70 mm in diameter with 8 windings and the maximum operating furnace temperature is around 2400 K. To avoid the oxidation of the crucible, the fibre was grown in Ar gas of 5-N purity. Visual observation of the meniscus region, solid-liquid interface and crystal growing was made by a CCD camera and monitor.

6.2.2 Seeding and growth procedure

Several Si single crystals with different lengths and diameters were grown. As a first step, a $<100>$ oriented thin cut from a Si disk was used as a seed. The crystals were grown at various pulling rate in the range $0.3\div2$ mm/min and were $0.4\div3$ mm in diameter and $40\div310$ mm in length.

The growth of crystal fibres is affected by vibrations which become especially intense at longer length. It was found that the length of crystal oscillations also depends on the fibre diameter [114]. Disconnections of the fibre growing from the molten zone were never observed, but the growth process was not perfectly stable and some abrupt changes in diameter and/or temperature happened, probably due to instabilities of the RF generator and

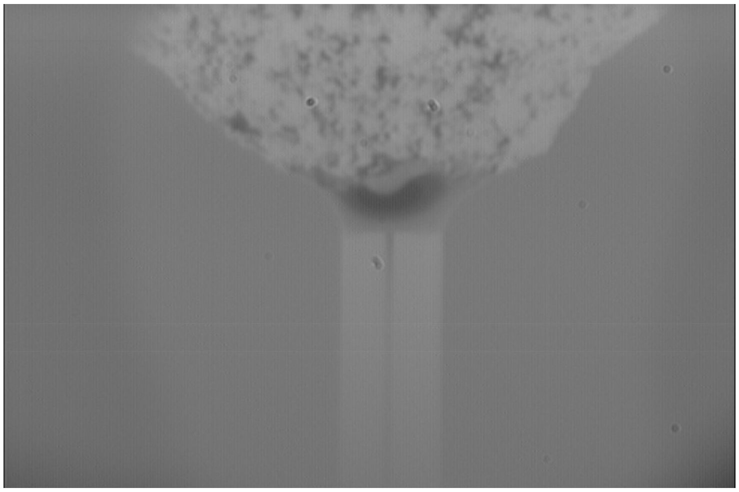

Figure 6.5: Image of the fibre during the growth process.

to reactions between silicon and the crucible that also prevented a good contact between the seed and the melt. Anyway, for most of their length, fibres show good quality. An image of the growth process for a sample is shown in figure 6.5.

Some typical Si crystal fibres, grown with different diameters and lengths, are shown in figure 6.6. The crystal orientation of the fibre was determined using Laue X-ray diffraction method. From this measurement it is possible to say that all the good quality parts of the fibre inspected showed single crystalline character (figure 6.7), but it was found that the orientation

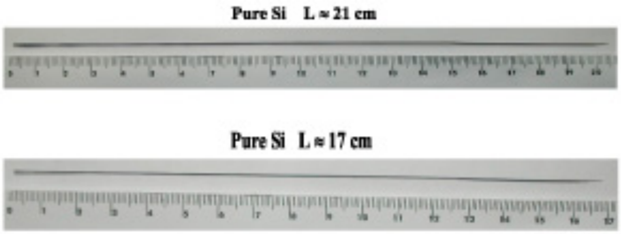

Figure 6.6: Grown Si crystal fibres about 0.4 mm in diameter, 17 cm and 21 cm long.

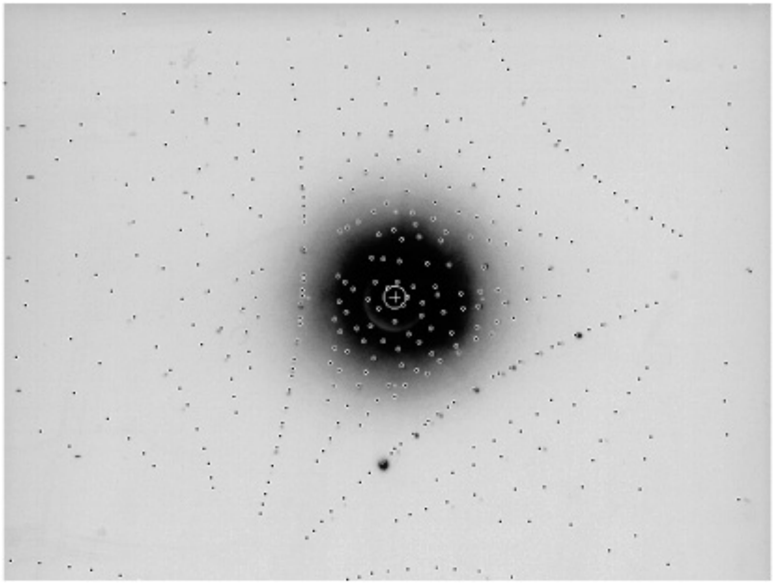

Figure 6.7: Laue simulation for Si.

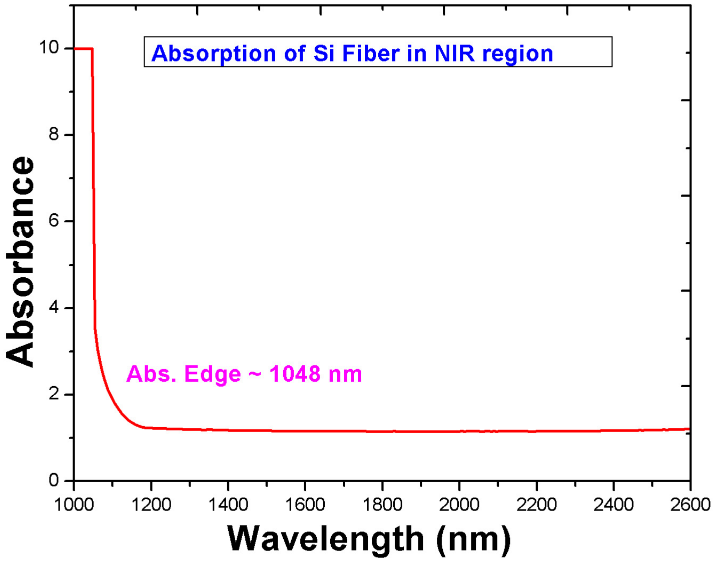

Figure 6.8: Absorption spectrum for Si.

changes along the fibre length in every point in which the diameter is not stable. As a result the fibres are not single crystals along the whole length but they are composed of several single-crystal parts.

Absorption investigations, which did not show the presence of any contaminants within the sensitivity of the apparatus, were also performed (see figure 6.8).

6.3 Experimental setup

In this paragraph there will be a description of the two experimental apparatuses for measuring the loss angle of excited fibres and for taking a profile of their shape to be used in the subsequent stage of data analysis.

6.3.1 Loss angle measurement apparatus

The experimental apparatus for measuring the quality factor of the silicon fibres produced as explained in the previous paragraph, is made of 4 functionally independent parts. The first one allows the clamping in the desired configuration; the vacuum chamber reduces the air damping to acceptable values; the electrostatic actuator and shadow-meter permit to manage the measurement. In figure 6.9 there is a scheme of the whole apparatus. A description of each of these subsystems will follow.

Vacuum system

The measured loss angle can significantly be affected by the presence of air around the fibre. In § 3.2.5 it was explained how the loss angle increases for viscous and molecular air damping. The best way to avoid this effect is to reduce air pressure: the stand with the clamping system of the fibre was put on a bench inside a vacuum chamber equipped with bull's eye and a pass-through connector.

The vacuum is realized through the action of two pumps arranged in cascade. A rotative pump brings the internal pressure (measured by a con-

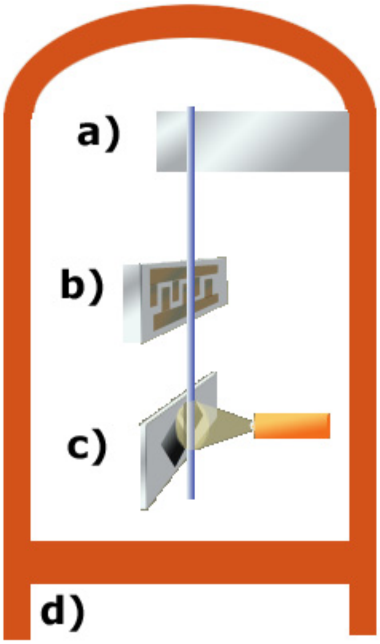

Figure 6.9: A scheme of the phi-measurement apparatus. Inside a vacuum chamber (d) there is a stand supporting the clamp (a), the excitation system (b) and the sensing shadowmeter (c).

duction manometer) to values around $6 \cdot 10^{-2}$ mbar; under this condition of pressure the turbo-molecular pump — whose rotor reaches 600 rpm in about 15 min — can be started up. Thanks to the turbo-molecular pump it is possible to reach a pressure around 10^{-6} mbar in about a day. Under this condition the air friction is negligible (the associated loss angle is less than 10^{-7}).

It is worth to note that the two pumps are linked with the vacuum chamber through semi-rigid tubes; for that reason the vibrations induced by the rotation of their mechanical parts are transferred to the stand: the vibration of the fibre will present noise structures, especially at 600 Hz and 50 Hz, which are the two pumps rotational frequencies.

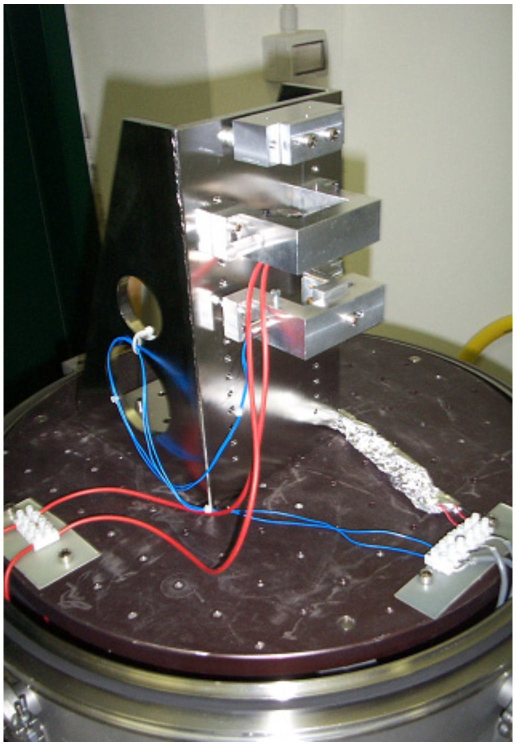

Figure 6.10: The stand of the suspended fibre is shown. In the upper part there is the clamp, in the middle the excitation system and at the bottom the sensing shadowmeter.

The stand and the clamp

During the measurement the fibre is in a vertical position being clamped at the upper end to a rigid stand (figure 6.10).

The excitation and the read-out system can be moved along the fibre axis and fixed to the stand; the fibre is clamped with two aluminum blocks and can be up to 27 cm long out of the clamp.

The fibre clamping is of the utmost importance for a good measurement: if the sample is softly tightened, it can move among the blocks and dissipate energy, if it is tightened too much it can be damaged on the surface, generating other losses. Moreover, as explained in § 3.2.4, even if the clamping system is extremely rigid, energy losses can occur due to the recoil of the whole structure. Although the mass of the stand is considerably greater w.r.t. the fibre mass ($\mu \gg 1$) it is better to avoid measurements near the resonance modes of the structure (of the order of kHz).

The excitation system

The fibre can be excited at the desired frequency; this is useful, both in a preliminary stage to determine the resonance frequencies and in the measurement stage to excite the known modes.

The excitation makes use of the polarization of the dielectric material that forms the fibre; this is dipped into a high-gradient electric-field $\vec{E}$, sinusoidally variable in time:

$$\vec{E}(\vec{x},t) = \vec{E}_0(\vec{x}) \sin \omega t \; . \tag{6.2}$$

The fibre polarizes and, on its surfaces, a density charge σ_p proportional to the polarization $\vec{P}$ is induced :

$$\sigma_p = \vec{P} \cdot \hat{n} = \epsilon_0(\epsilon_r - 1)\vec{E} \cdot \hat{n} \; , \tag{6.3}$$

where $\hat{n}$ is the versor of the fibre surface, ϵ_0 and ϵ_r are the vacuum and relative dielectric constants. The effect of the electric field is to generate a local force per unit surface:

$$\frac{\vec{F}}{\Delta A} = \sigma_p \vec{E} = \epsilon_0(\epsilon_r - 1)E_0^2 \sin^2(\omega t)(\hat{E}_0 \cdot \hat{n})\hat{E}_0 \; . \tag{6.4}$$

The excitation is proportional to the square of $\sin(\omega t)$, and so, having $\sin^2(\omega t)$ a period of π, the effective angular frequency is 2ω. To avoid this discrepancy between the frequency of the field and of the induced excitation, a constant field $\vec{E}_c$ is over-imposed. The exciter is composed by 2 electrodes in shape of compenetrating combs, in a way that two consecutive teeth are linked to opposite poles of the generator. The fibre is put near the plane of the combs (figure 6.11), among two teeth: here the gradient is almost maximum and parallel to the plane itself.

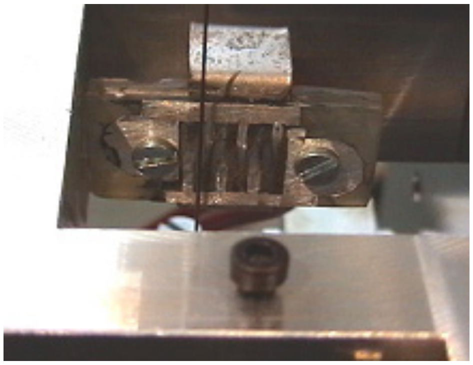

Figure 6.11: Photo of the actuator made by a comb capacitor.

In this way the fibre is forced to oscillate in the direction more convenient for the detection. The signal used for the excitation has a peak-to-peak amplitude of 700 V, to which a continuous voltage of 400 V is over-imposed.

The read-out system

The movements of the excited fibre are detected following the displacements of the fibre shadow, projected by a LED diode on a double photodiode.The photodiode is separated in two elements by an insensitive gap of about 500 μm; each element is about 5 mm wide. The two photodiodes were initially placed as shown in figure 6.12 a with the gap parallel to the direction of the fibre axis. In this configuration the allowed oscillating region for a good detection is restricted to a little slice, about two fibre diameters wide: the detection is made extremely difficult, especially for the low frequency resonance modes for which the oscillating amplitude is quite high. It was decided to tilt the photodiodes of about 45 degrees and thus the detecting region is much bigger as shown in figure 6.12 b. If the fibre is exactly placed at the center of the gap, the difference of the signal from the two elements

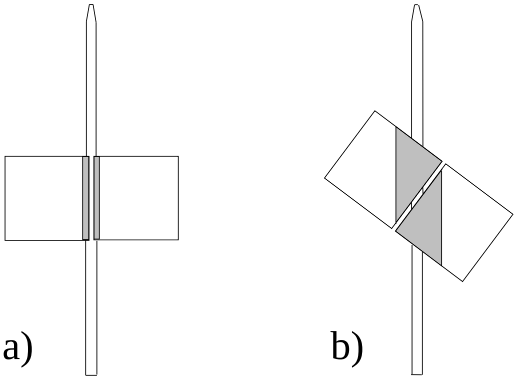

Figure 6.12: Two different configuration for the read-out system are shown with the photodiode gap parallel (a) and tilted (b) w.r.t. the fibre axis. The gray areas highlight the allowed sensitive regions for a good detection.

is zero; it becomes negative or positive if the fibre moves and its amplitude and frequency mock the fibre oscillation.

It is worth to note that the read-out system detects the movements of the fibre at only one point, and gives no information on the whole motion of the fibre. It can happen that, for certain resonance modes, the detection point shows small or even null displacements (if it is a nodal point or if the movements are on the same direction of the LED light); in this case, the relative frequency does not admit a Q-factor measurement.

A sketch of the output line is shown in figure 6.13. The two photodiodes are put in a *push-pull* configuration in order to subtract their signal and the difference is filtered and amplified.

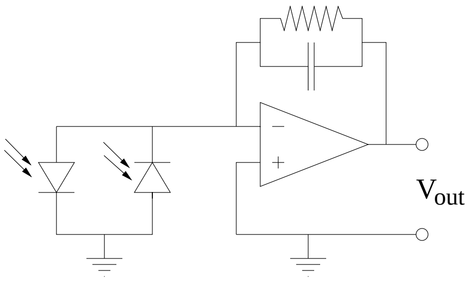

Figure 6.13: Sketch of the acquisition system circuit.

The cables with the output voltage from the photodiodes come out of the vacuum chamber by means of a feed-through; inside the chamber they are bound by aluminum foils put at a reference voltage, to shield them from the electro-magnetic noises induced by the surrounding electric currents (especially the ones in the high voltage cables of the excitation system).

The LED diode is fed from outside; the power supply is stabilized to reduce at minimum the fluctuation introduced in the reading. The power voltage is tunable and it is around 6 V.

Data acquisition

The output of the filter is referred to the ground of the system and goes on a single ended port of the computer acquisition board. The board is driven by a `LabVIEW®6.0` [115] program that samples the signal and converts it with a 16-bit ADC. The program allows to choose the internal clock frequency of the acquisition (number of sample per second); this value has to be chosen high enough to avoid aliasing in the acquired signal.

In order to measure the fibres quality factor, several programs have been realized with `LabVIEW®`. In each of them the basic part is the sampling system and the digitalization of the measurement (DAQ) that acquires N samples at a frequency f_c in a time N/f_c.

In a *centering* program the signal is acquired continuously in time and followed with a real-time plot. This is useful to accurately position the fibre in front of the photodiode and to verify the whole acquisition system.

A *test* program acquires the signal in subsequent sets of N samples and filters them with a digital band-pass filter around a chosen frequency. The signal is followed in the excitation phase at the given frequency ω_r and in the subsequent phase of excitation interruption; the behaving of the oscillation allows to verify the actual presence of a resonance. If this is not the case, when the excitation is suspended, the signal abruptly decreases instead of decaying exponentially.

The program that manages the *standard* measurement enables the DAQ procedure to start as soon as the excitation of the fibre is interrupted.

The acquisition extends for a time at least of the order of the characteristic damping time τ:

$$\tau = \frac{2Q}{\omega_r} \; . \tag{6.5}$$

With the acquired samples vector, the program extracts the Fourier spectrum through the FFT algorithm (*Fast Fourier Transform*), identifies the peak of the excited resonance and calculates the frequency finding the centroid with a Gaussian fit.

The sampled signal is then filtered sharply around the resonance frequency with a digital filter in order to isolate that Fourier component only. This component is shown in a plot and its amplitude shall follow an exponential damping.

To obtain an estimate of the quality factor of the single measurement the program makes a Hilbert transform $\hat{x}$ of the filtered signal $x(t)$:

$$\hat{x}(t) = -\frac{1}{\pi}\int_{-\infty}^{+\infty} \frac{x(s)}{t-s} ds \; . \tag{6.6}$$

If the Fourier transform is referred to with a superscript tilde, the following identity

$$\widetilde{\hat{x}}(\omega) = -i \; \mathrm{sign}(\omega)\tilde{x}(\omega) \tag{6.7}$$

holds. Thus the Hilbert transform yields a dephase of $-\pi/2$ for the positive frequency components of $x(t)$, leaving their amplitude unaltered. Assuming, as it is for the unfiltered signal, that

$$x(t) = Ae^{-\frac{t}{\tau}} \sin(\omega_r t) \; , \tag{6.8}$$

the Hilbert transform is

$$\hat{x}(t) = -Ae^{-\frac{t}{\tau}} \cos(\omega_r t) \ . \tag{6.9}$$

The quantity

$$\mathcal{Z}(t) = x(t) + i\hat{x}(t) \tag{6.10}$$

is defined pre-envelope of $x(t)$. The program, once $\hat{x}(t)$ has been extracted, defines $\mathcal{Z}(t)$ as in (6.10) and gets the envelope of the oscillation calculating the squared modulus of the pre-envelope

$$|\mathcal{Z}(t)|^2 = A^2 e^{-\frac{2t}{\tau}} \big(\cos^2(\omega_r t) + \sin^2(\omega_r t) \big) = A^2 e^{-\frac{2t}{\tau}} \tag{6.11}$$

To determine the quality factor it is necessary to measure τ (see (6.5)); thus it suffices to calculate the logarithm of the envelope:

$$R(t) = \ln(|\mathcal{Z}(t)|^2) = 2\ln(A) - 2\frac{t}{\tau} \ , \tag{6.12}$$

The output signal should be a straight line; the program performs a linear fit, giving the best value for the slope $\gamma = -2/\tau$. This quantity is used to have an estimate of Q:

$$Q = -\frac{\omega_r}{\gamma} \ . \tag{6.13}$$

It is worth to note that the initialization procedure of the filter is not immediate. The filter algorithm proceeds through the computation of the convolution product between the signal and the transfer function in the time domain; the filter shall be filled with a samples vector in order to work properly. The creation of this vector needs a while, depending on the passing band; the beginning of the acquisition is jeopardized and thus a samples set in which $R(t)$ is linear is selected for the fitting procedure.

It can happen that the characteristic decay time τ is of the order of hundreds of seconds, or more. Under those conditions the number of samples can be very high. On the other hand, it is not possible to decrease the acquisition frequency at will, because of aliasing. To solve this problem a lock-in amplifier can be inserted before the acquisition board. The lock-in multiplies the input, at high frequency ω_{in}, by a generated sinusoidal signal at a frequency $\omega_g \simeq \omega_{in}$. The output results to be a superposition of two signals at frequencies $\omega_{low} = |\omega_{in} - \omega_g|$ and $\omega_{high} = \omega_{in} + \omega_g$. The lock-in includes also a low-pass filter that selects the ω_{low} component only. The amplitude decay of this signal has the time constant of the original signal and the Q-factor measurement can proceed as explained before, filtering again around the resonance frequency, if necessary.

This method is valid if τ is high enough. In fact, to see the oscillation damping, several oscillations in the time (τ) are needed. Thus, if τ is short, ω_{low} should be high. This reduces the usefulness of the lock-in and introduces in the output-signal spectrum the input noise, in a band of $2\omega_{low}$ width, centered around the frequency ω_g. Therefore it can happen, especially at high frequencies, that the standard procedure is preferable.

6.3.2 Profile measurement apparatus

The produced silicon fibres do not have a circular-cylindrical shape: the diameter changes along the fibre axis and the section is more similar to an ellipse indeed, that can also have a variable axes orientation. In order to make a more realistic model of the fibres it was decided to construct an apparatus to perform a measurement of the diameter changes. The main axis of the fibres, on the other hand, is straight (this is a consequence of the growing procedure) and there was no need to model its bending. These data are used to reconstruct a 3-D model of the fibre as explained in § 6.4.3.

The fibre to be measured is put on a stand in the same configuration as it is clamped during the ϕ measurements. The stand is settled on a rail to allow sliding along the fibre axis by means of a long rotating screw fixed w.r.t. the optical bench as shown in figure 6.14; the structure provides also the possibility of rotating the fibre of a chosen angle around its axis.

The sensing part of the apparatus consists of a shadowmeter realized with a 635 nm He-Ne laser of 1 mW power and a 5 mm×5 mm photodiode that receives the shadow projected by a little segment of the fibre. The light from the laser is focused to obtain a plane wave front and a sufficiently large beam spot size. The photodiode is shielded and receives the laser light passing through a little fissure only. This allows diameter measurements at a particular chosen position along the fibre axis. Before being shielded the laser light impinges on a beam splitter: a part of it goes towards the fibre and the remaining part is focused on another photodiode. The signal from the latter is used as a reference to compensate for laser power instabilities: the acquired signal is taken as the ratio between the shadowmeter signal and the reference one.

Another shadowmeter system, similar to the previously described one, is used for monitoring the displacement of the fibre. As the stand moves on the rail, a rotating shield alternatively passes on the beam, generating an oscillating signal on the photodiode. This signal is used as a trigger for the acquisition.

The three signals are amplified and sent to an acquisition board on a computer (see figure 6.15). The board is driven by a `LabVIEW`® program that samples the signals at 10 kHz and converts them with a 16-bit ADC. As a first step the signals are modulated using a filter around the modulation frequency of 1360 Hz. The signal coming from the trigger photodiode is analyzed with a program that identifies the peaks due to the rotating shield. In coincidence with the peaks times, a routine performs a mean over 200 samples of the signals coming from the detecting photodiode and from the reference one, and calculates the ratio between them. The results are stored in a file.

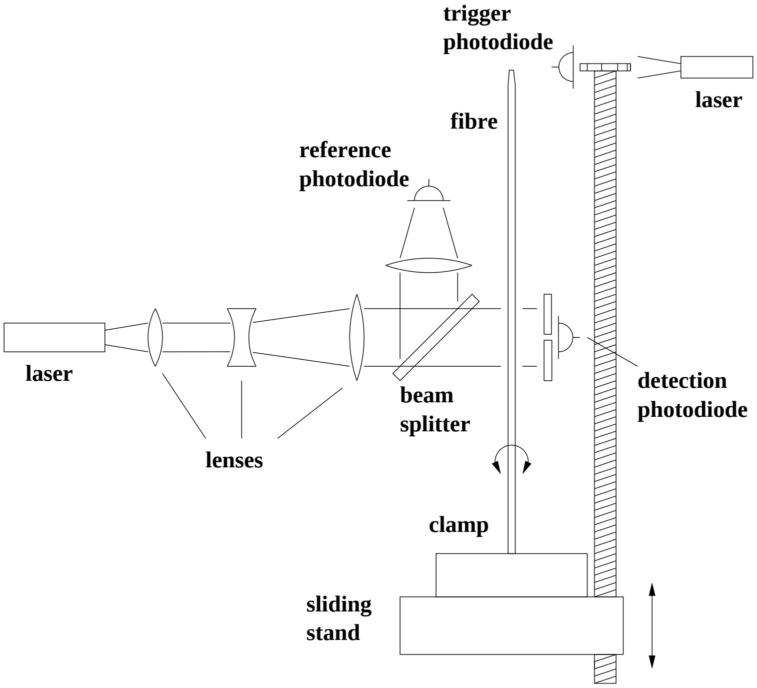

Figure 6.14: Sketch of the profilation system setup.

6.4 Measurement of the thermoelastic peak

6.4.1 Standard measurement procedure

The measurement proceeds following the general scheme as described below. Before starting the thermoelastic peak measurement it is necessary to perform an acquisition of the fibre profile.

A calibration sample, consisting of four wires of well known sections, is clamped on the stand of the profile apparatus. The measurement of the wires diameters is performed making the stand slide on the rail by means of the long turning screw and using the acquisition program described in § 6.3.2.

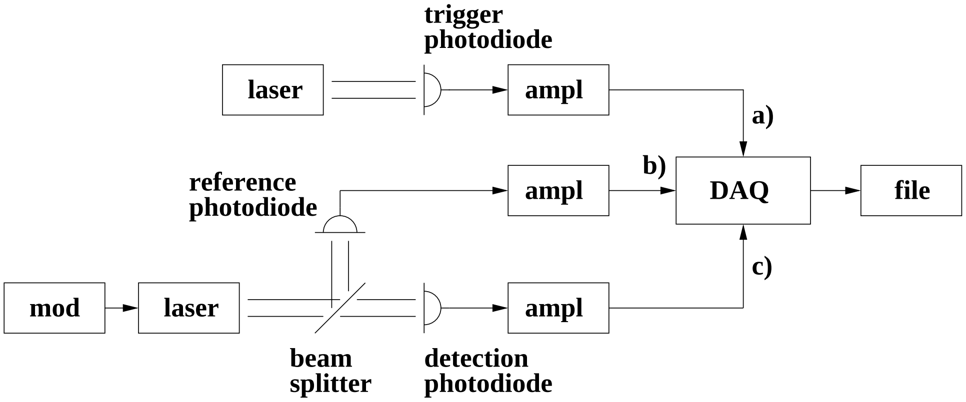

Figure 6.15: A sketch of the acquisition system for profile measurement is shown. The signals from the three photodiodes are amplified and come to the acquisition system. Using the signal (a) as a trigger, the ratio between the main signal (c) and the reference one (b) is performed and stored in a file.

The data, stored in a file, are used for a calibration of the signal from the sensing photodiode.

Then it is necessary to accurately clean the surface of the fibre with isopropilic alcohol, to remove impurities and chemical volatile residuals, which could compromise the Q-factor measurement and the efficiency of the vacuum system.

The fibre is filed at one end on two opposite sides as shown in figure 6.16. In this way the contact surface is increased allowing a tighter clamping and lowering the probability of breaking the fibre in the clamping process. A total force acting on the clamp is chosen and is applied using a simple device based on scales and a press.

The fibre, together with its clamp, is put on the stand of the profile apparatus. Profile measurements are performed as just described for the calibration procedure and fibre diameters are measured for several rotation angles around fibre axis, usually every 30°. The produced data are used inside a finite element analysis (FEA) to reproduce an accurate model of the fibre as explained in § 6.4.3.

Then the fibre is ready for the ϕ measurement and it is settled in the vacuum chamber and blocked on the stand together with the clamp. Using the centering program described in § 6.3.1, the position read-out system is set in order to center the fibre shadow w.r.t. the gap between the two sensing photodiodes. The vacuum chamber is closed and the air pressure is lowered as described in § 6.3.1. In this phase it is important to avoid activating the excitation system: around a pressure of 1 mbar the gas in the chamber is at a critical pressure for the production of electric discharges.

At a level below 10^{-5} mbar the measurement can start. Preliminarily, it is necessary to identify the various resonance mode frequencies of the fibre.

A power-spectrum analyzer is used to display the frequency response of the fibre to a white noise excitation. The analyzer shows a mean over several acquisitions and the visible peaks reveal the presence of resonances. The FEA model gives these frequencies with a good level of precision, except for a scale factor very near to unity. This can be very useful in speeding up the procedure: once the first two modes are identified, it is easy to find all the others, exciting with a sweeping frequency near the expected ones.

The test program described in § 6.3.1 allows a direct check of the damping behavior of the found frequencies.

When a set of frequencies is available, for each one a Q-factor measurement is performed exciting the oscillation and then interrupting the excitation abruptly. The subsequent damping motion is detected and recorded as a file for possible further analysis. The standard measurement program gives an estimate of the Q-factor. For each frequency the measurement is repeated several times and the mean of the results is taken as the final value with an error equal to the standard deviation of the set. This error ranges from 1%

to 5%; the contribution coming from the fit is only al the level of 1%.

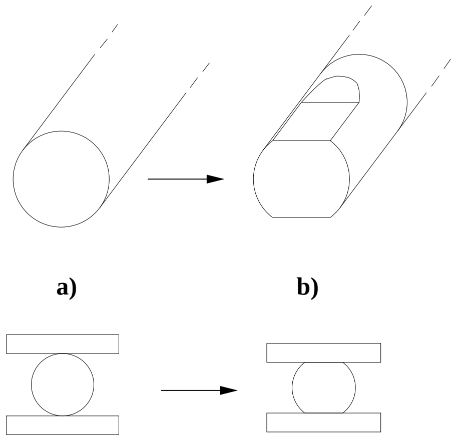

Figure 6.16: The head of the cylindrical fibre (a) is filed on two sides in order to allow a better clamping (b).

6.4.2 The etching process

It is possible to operate on the fibres with a chemical process called etching. It consists essentially of a bath in a chemical solution that acts on the surface of the fibre removing atoms layers.

It can be very useful if it is necessary to polish the surface from contaminants or unwanted oxides. Their presence can jeopardize the measurement of the fibre Q-factor hiding the real loss angle of the material as described in § 3.2.3.

Another advantage of the etching process is that it allows to deeply act on the fibre shape.

On the one hand it is possible to lower the fibre diameter for exploring different regions of the thermoelastic noise, whose frequency peak depends on the diameter. In fact, there are problems in producing fibres with diameters below 500 μm, because of instabilities and technical difficulties occurring during the micro-pulling down process.

On the other hand the form of the profile can be shaped in order to reduce clamp losses or correct macroscopic defects. In fact, the etching can be realized only on certain parts of the surfaces, shielding the rest with a layer of enamel — like the nail varnish —.
It is possible to shield the head of the fibre: the obtained bigger head allows a better clamp — the bigger the surface, the more tightened the clamp can be — and shifts the most solicited parts of the fibre to a region that is far from the clamp itself. The latter condition is important because the heavily solicited parts near the clamp can introduce extra friction on clamp surfaces and transmit energy to it affecting the loss angle measurement.
It is also possible to act locally on different segments of the fibre in order to correct any defects that may have risen during the growing process. In this way the fibre can be made more regular by simplifying the modelization and analysis phases.

The used chemical solution is composed of nitric acid by 75% (HNO_3 at a 70% concentration), fluoridric acid by 15% (HF at a 59.2% concentration) and acetic alcohol by 10% (CH_3COOH). Etching occurs via a redox reaction followed by the dissolution of the oxide by HF that acts as a complexing agent. The reaction can be schematized as

$$\mathrm{Si} + \mathrm{HNO_3} + 6\mathrm{HF} \;\rightarrow\; \mathrm{H_2SiF_6} + \mathrm{HNO_2} + \mathrm{H_2O} + \mathrm{H_2}\ . \tag{6.14}$$

Points on silicon surface randomly become oxidation or reduction sites. These act like localized electrochemical cells, sustaining corrosion currents of about 100 A/cm^2, which are relatively large currents. For the kind of solution under consideration, each point spends, on the average, the same amount of time being an anode or a cathode site; this leads to an isotropic etching, i.e. an etching whose corrosion velocity of the material is the same in all directions.

The nitric acid gives birth to NO_2, that is reduced at a cathode site which produces free holes:

$$2\mathrm{NO_2} \;\rightarrow\; 2\mathrm{NO_2^-} + 2\mathrm{h^+} \;. \tag{6.15}$$

Simultaneously, silicon is promoted to a higher oxidation state at an anodic site through positive charges in the form of holes:

$$\mathrm{Si^0} + 2\mathrm{h^+} \rightarrow\; \mathrm{Si^{2+}} \;. \tag{6.16}$$

The $\mathrm{Si^{2+}}$ combines with $\mathrm{OH^-}$ to form $\mathrm{SiO_2}$:

$$\mathrm{Si^{2+}} + 2\mathrm{OH^-} \rightarrow\; \mathrm{Si(OH)_2} \;\rightarrow\; \mathrm{SiO_2} + \mathrm{H_2O} \tag{6.17}$$

and $\mathrm{SiO_2}$ is then dissolved by HF to form a water soluble complex of $\mathrm{H_2SiF_6}$:

$$\mathrm{SiO_2} + 6\mathrm{HF} \;\rightarrow\; \mathrm{H_2SiF_6} + 2\mathrm{H_2O} \;. \tag{6.18}$$

The nitric acid has a complex behavior and its concentration manages a chain of reactions that form an autocathalitic cycle for holes production and $\mathrm{HNO_2}$. The acetic acid is a frequent substitute for water as a diluent; it has a lower dielectric constant w.r.t. water, thus it produces a minor dissociation of $\mathrm{HNO_3}$, yielding a higher oxidation power for the etching. Furthermore, acetic acid is less polar than water and it can help to achieve proper wetting of slightly hydrophobic silicon.

In figure 6.17 it is shown a triangular diagram [116] that allows to find the various etching velocity depending on the concentrations of the three solution components. The little circle represents the working point chosen for the solution described above.

The etching is performed in a long basin filled with the HNA solution. The fibre can enter the solution staying in a horizontal position. This is a much more efficient way of doing the etching w.r.t. a vertical immersion: in the latter case the reaction products, which are hotter and come to the solution surface, do create vertical gradients — either gradient of the reagents

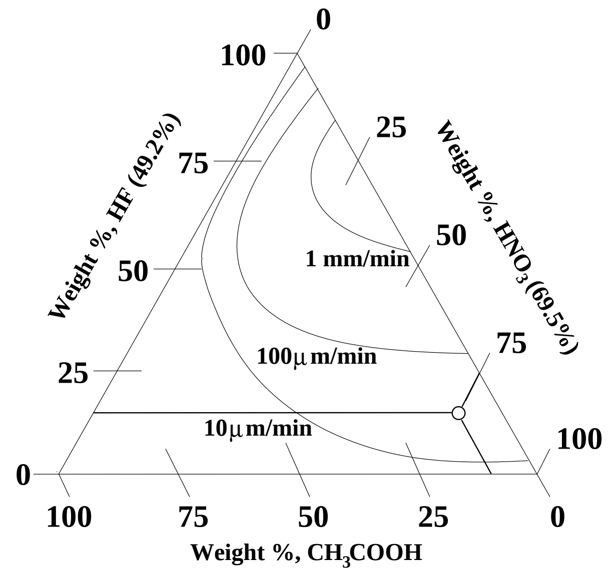

Figure 6.17: Diagram of the etching velocity for an HNA etching solution. Three iso-velocity lines are shown together with the working point corresponding to the solution used for the fibre etching described in the text.

concentration, or gradient of temperature — that can deeply modify the velocity of the etching itself. In fact, it was experimentally found that the fibre surface is etched faster at the top than at the bottom. With a horizontal etching the above mentioned problems are avoided and the reaction velocity is seen to be constant all along the fibre.

The etching procedure consists of three steps. First of all an etching lasting some minutes is performed in order to remove the superficial impurities. Secondly, after deciding the target diameter of the fibre and calculating the duration time of the etching, which depends on the particular HNA chosen solution, a second etching is performed. During this phase it is also possible to apply nail varnish on the fibre surface in regions that are already thin or on the part chosen to become the head to be inserted in the clamp. Finally the nail varnish is removed with acetone and the fibre is subsequently dipped into a fluoridric acid solution to deeply clean the fibre from the oxide that may still be present on its surface. An example of a fibre etching is shown in figure 6.18.

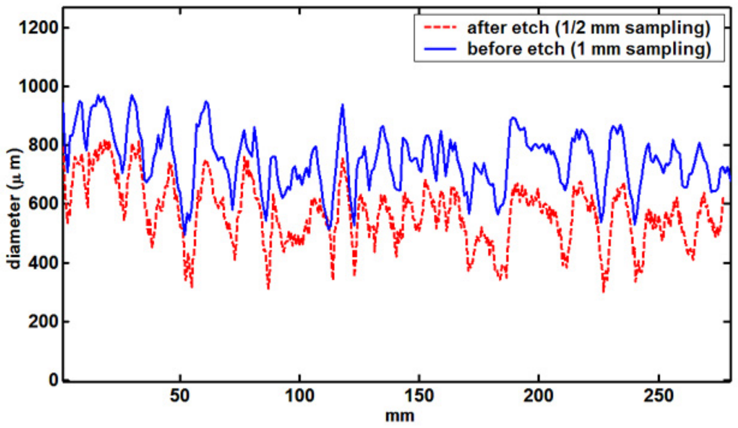

Figure 6.18: The profile of a fibre at a particular angle is shown before (solid blue line) and after (dashed red line) an etching. It is evident that the diameter has reduced of about 200 μm.

6.4.3 Modeling the fibre

From the data obtained with the profile measurement apparatus, described in § 6.3.2, it is possible to reproduce a 3-D model of the fibre to be used for a finite element analysis (FEA) in the framework of the `ANSYS`®`8.1` [103] software.

Profiles alignment

The data coming from the profile measurement (§ 6.3.2) are 6 vectors of numbers representing the longitudinal views of the same fibre every 30° of rotation along the fibre axis. The data acquisition has not a definite and reproducible starting point of one profile w.r.t. the subsequent rotated one. Therefore, to make the fibre profiles correspond to one another it is necessary to manually align them. The procedure is done with the help of a `MATLAB`®`6.5` [117] program that acquires the data and shows the different profiles on the same

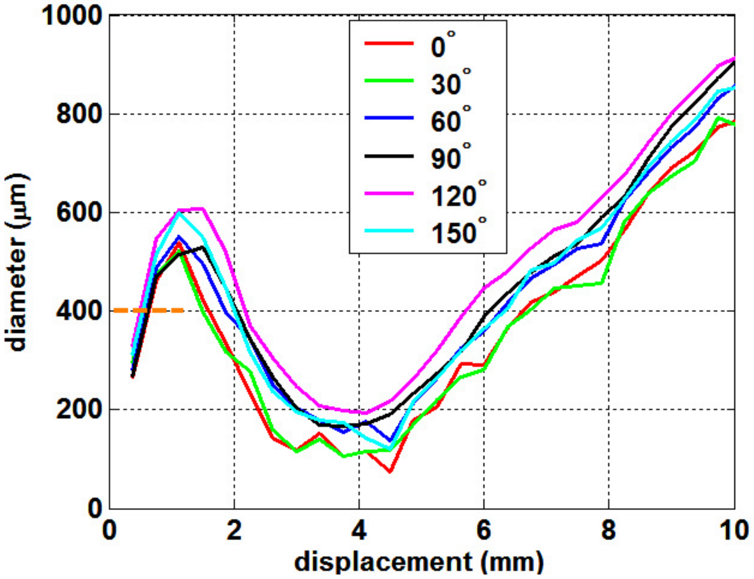

Figure 6.19: Profiles at various section angles are shown for the part of the fibre near to the tip. The alignment of the different data sets (one for each angle) is realized manually over-imposing along the x axis the points preceding the 400 μm-diameter line crossing indicated on the left by the orange dashed line.

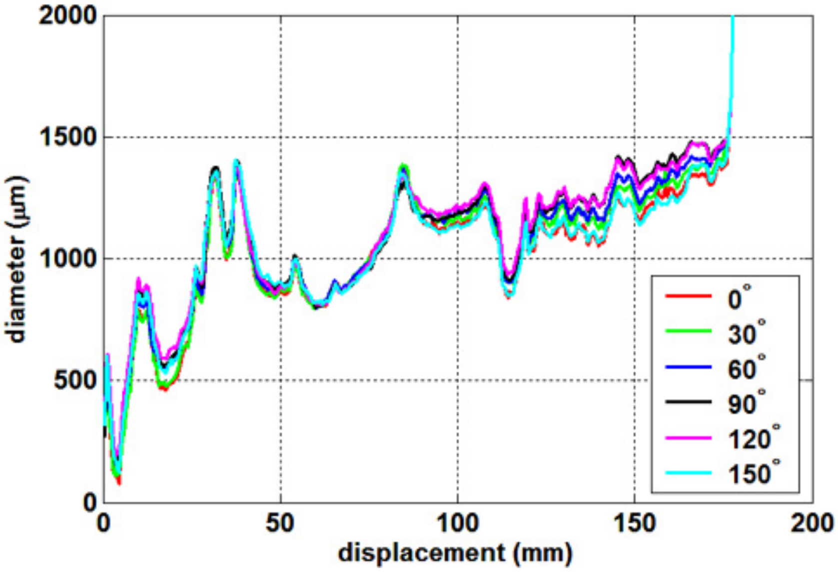

Figure 6.20: Profiles at various section angles.

plot. In figure 6.19 the beginning of the 6 sets is shown after the alignment, done by choosing as starting points the ones preceding the crossing of the 400 μm-diameter line indicated in orange. In figure 6.20 an example of the aligned profiles is shown for a 177.5 mm-long fibre. It is evident that the fibre is not a perfect cylinder but it is also evident that the various profiles are very similar to one another. The aligned profiles are stored in a matrix for further analysis.

Shadow-projection correction

Data have to be corrected for a geometrical effect due to the setup of the profile apparatus. The laser-shadowmeter system systematically overestimates the diameter at the various acquisition angles: the parts of the fibre projecting the shadow are not always the expected ones because the fibre is not a perfect cylinder. To understand this effect refer to figure 6.21, in which the "true" fibre section is drawn in blue and the direction of the projecting shadow is indicated by black arrows every 30°. Without making any correc-

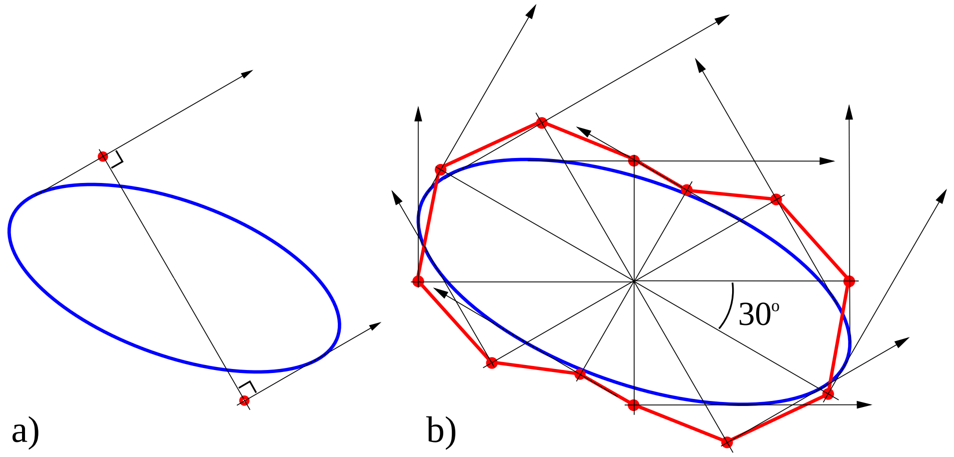

Figure 6.21: Estimation of the fibre section from profile measurements. Projecting directions of the shadows are indicated by black arrows and estimated section points are in red (a). Without any correction the "true" section of the fibre (blue ellipse) is falsely interpreted to be the red polygon (b).

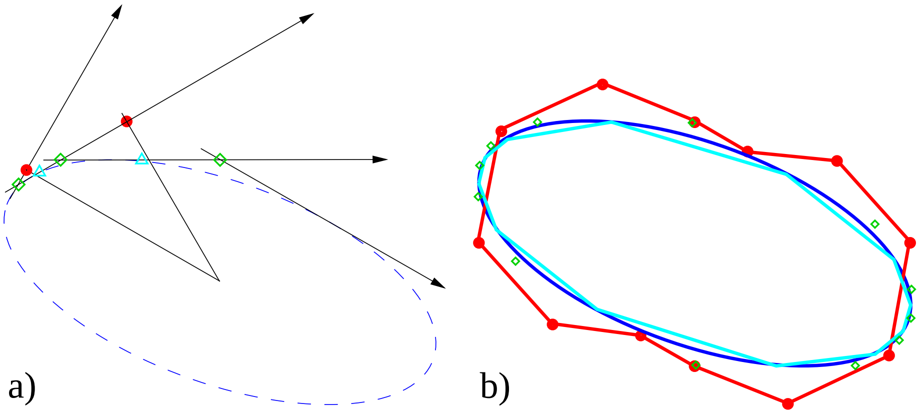

Figure 6.22: Correction of the estimated fibre section from profile measurements. Two consecutive shadow projections identify construction points (the green squares). The new estimated section points (cyan triangles) are chosen to be the mid-points of the segments delimited by the green squares (a). A comparison among the “true” section (in blue), the fake estimation (in red) and the corrected one (in cyan) is given (b). It is evident that the peanut-shell deformation is corrected.

tions, the shadows are interpreted to come from the red points and not from the tangential points between the fibre and the black arrows. It is evident that elliptical sections are distorted toward a peanut-shell shape. The more the eccentricity, the more the deformation and if the fibre were perfectly cylindrical this effect would disappear. This is not the case, because most of the sections are roughly elliptical.

Therefore an algorithm done with `MATLAB`® software was developed to correct the introduced bias. It resides on the idea that the real section of the fibre is contained inside the envelope of all the projection directions of the shadows. As shown in figure 6.22 a, two consecutive shadow projections intersect in construction points identified with green squares. The new estimated section points (cyan triangles) are chosen to be the mid-points of the segments delimited by the green squares. A comparison among the “true” section (in blue), the fake estimation (in red) and the corrected one (in cyan) is given in figure 6.22 b. It is evident that the peanut-shell shape, present in the red curve, is corrected toward a shape much more similar to the real one.

The finite element model

The corrected data are imported in `ANSYS`® thanks to a routine done with `AWK` [104], a pattern-directed scanning and processing language. The routine converts the data file into an `ANSYS`® macro file that executes all the commands to create the keypoints. They are intermediate point-like structures used as frames to construct areas, volumes and, finally, the elements of the 3-D model. These steps of the model creation are done with an automated `ANSYS`® macro file that has just to be slightly corrected from fibre to fibre, depending on the number and the length of the profiles and on the mean section of the fibre itself.

Firstly the lateral surface of the fibre is created. It is simply a set of triangles sharing edges. The triangles have two keypoints of one section and one keypoint of the previous section or the following one. A view of the lateral surface of a fibre is shown in figure 6.23 for two adjacent rings of triangles.

Secondly areas associated to each fibre section are created. They have no physical significance but they are of fundamental importance for creating intermediate volumes, delimited by 2 of these areas and by 24 lateral triangles. The volumes are glued together to form a unique object and the model is ready to be meshed.

Usually it suffices to mesh volumes with an automated command provided by `ANSYS`®, called “free mesh”. In some particular cases[2], the mesh has to be guided by an intermediate one, generally done on 2-D surfaces. This is the

---

[2] This usually happens when the model is a 3-D model with one dimension that extends much more or much less w.r.t. the others.

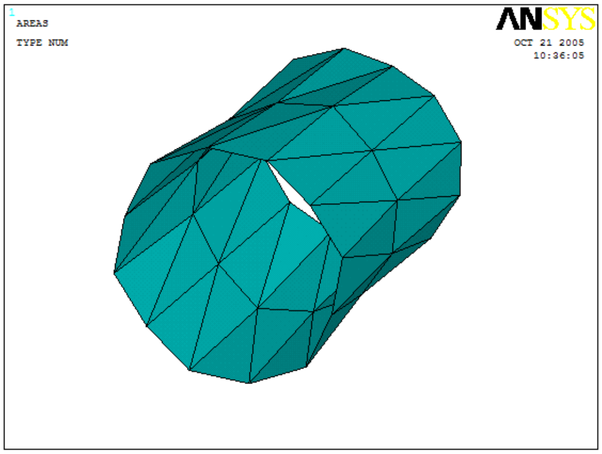

Figure 6.23: A part of the lateral surface creation of the fibre model is shown. The surface is constructed by the definition of triangles connecting two adjacent fibre sections.

case, and a mesh is preliminarily done with PLANE2 elements on the slice areas. The elements are triangular and their dimensions are taken in order to have 12÷16 elements for each section. This feature is obtained imposing single elements to have a size proportional to the section area. In figure 6.24 several fibre sections are shown together with the PLANE2 elements on them. It is evident that the number of elements per section is constant even if the section is widely changing dimension.

Thanks to the grid provided by the PLANE2 elements on the sections, it is straightforward to mesh the whole model. It suffices to force no line division[3], in order not to have too many elements, and to use the standard *free-mesh* command with 3-D SOLID92 elements. A view of the model elements is shown in figure 6.25 where a set of them has been removed to permit the vision of the other underlying elements.

The elements can be assigned the material properties, i.e. Young's mod-

---

[3] This means that the *mesher* cannot use parts of the already defined lines in building the elements of the model.

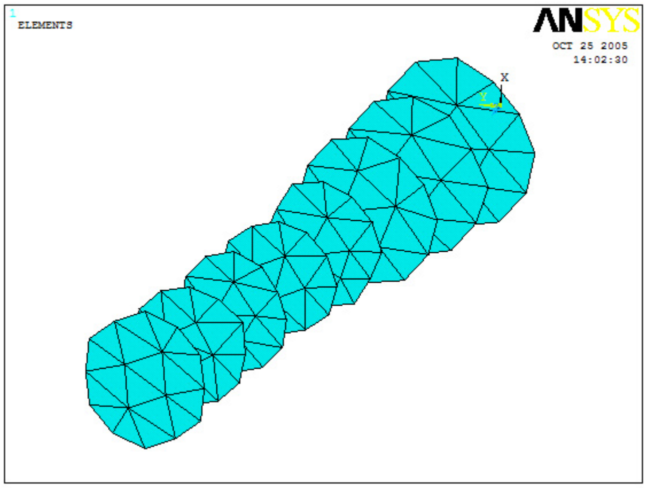

Figure 6.24: Several sections of a fibre are shown together with the triangular elements on them. The number of elements per slide is not depending on the slide dimension.

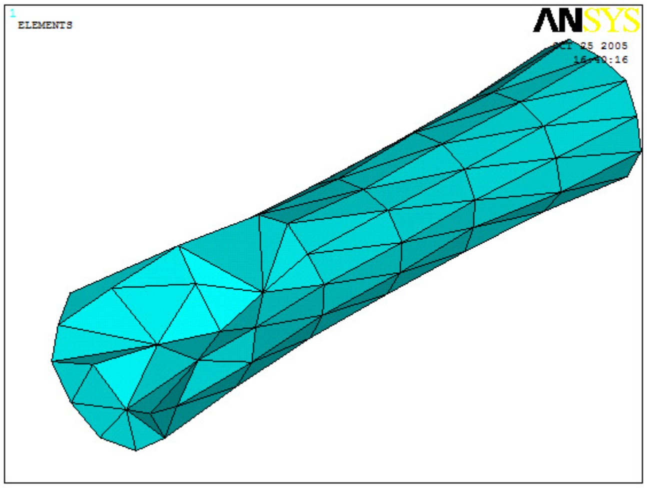

Figure 6.25: View of elements of a fibre model. Some of them are removed to allow the vision of the underlying elements.

ulus, Poisson's ratio and the density. In order to simulate the clamping, the last section on one end of the fibre is constrained in all the degrees of freedom.

The model is ready to perform a modal analysis on it. In the modal analysis the software extracts the frequencies and the shapes of the resonance modes. It allows also the user to look for stress and strain distribution on the surface or inside the simulated objects.

6.4.4 Phi measurements

Measurements of the thermoelastic peak are performed following the procedure described in § 6.4.1.

The measured values for a 308 mm long fibre are shown in figure 6.26; the free length of this fibre after the clamping is 289 mm. As it will be explained in § 6.5, from the analysis of these data the values of Young's modulus E, of the thermal expansion coefficient α and of the thermal conductivity κ can be evaluated. Using the measured value of E, an "effective" diameter can be defined for each resonance mode. On assuming a cylindrical-shaped fibre with this diameter it is possible to predict a value for the loss angle for each resonance frequency. These predictions, with the error coming mainly from the uncertainty in the diameter measurement, are also shown in figure 6.26.

It is quite evident that there is the presence of an excess loss. This excess can be due to contaminants present on fibre surface: after the production of the fibre, the external surface is in fact subject to oxidation; furthermore the deposition of some impurities on it, during the growing process, is also possible. To verify this hypothesis a chemical etching process was performed on the fibre as described in § 6.4.2, removing the first silicon layers. The part of the fibre inside the clamp was not etched: in this way the narrowing of the fibre just outside the clamp can help to further reduce the clamping losses.

In figure 6.27 the measured values of the loss angle for the same fibre after the etching are shown. The free length of the fibre after the clamping is 278 mm and the diameter reduction shifts the position of the thermoelastic peak to higher frequencies.

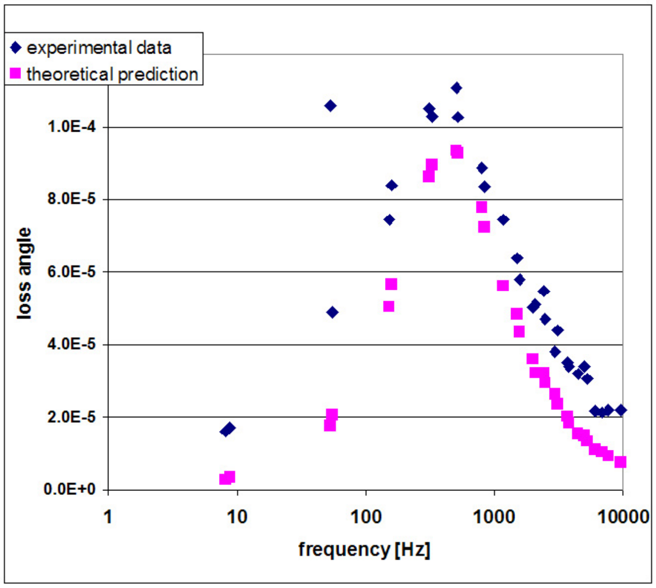

Figure 6.26: Measured loss angle for a 289 mm (free length) fibre, with an average diameter of 746 μm. The squares represent the thermoelastic contribution as predicted by the model described in the text.

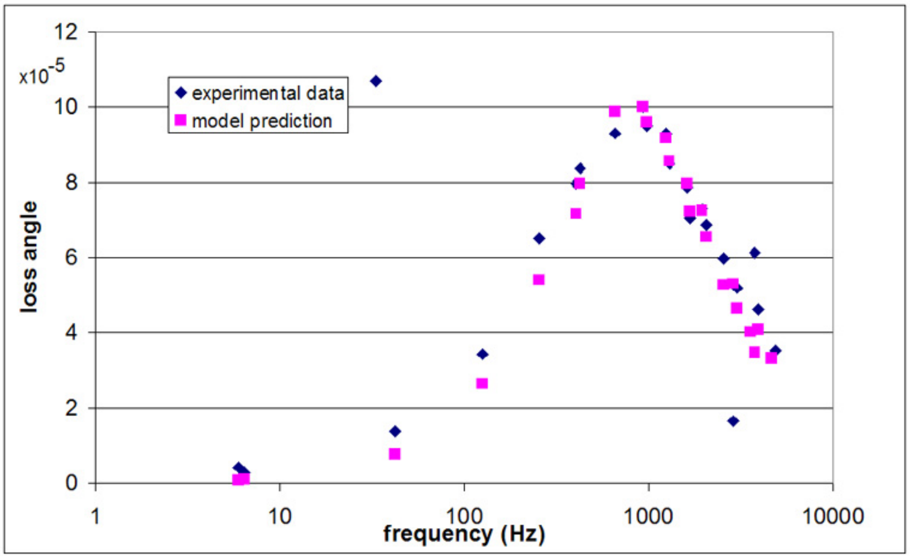

Figure 6.27: Measured loss angle for the same fibre as that shown in figure 6.26 after the etching process; the average diameter is now 574 μm, while the free length is 278 mm.

The comparison between these values and the expected thermoelastic losses, computed as previously described, points out that the excess loss is not present anymore, thus confirming the surface contamination hypothesis. A small excess is still found at low frequencies: this is probably due to clamp losses.

In figure 6.28 the measured values of ϕ for another fibre — 111.5 mm long — treated with chemical etching are shown. Since this fibre has a roughly elliptical section, it is evident that there are two sets of modes, corresponding to the different length of the two ellipse axes. An unloaded cylindrical fibre of length L, diameter d and clamped at the upper edge shows a set of resonance frequencies given by [30]:

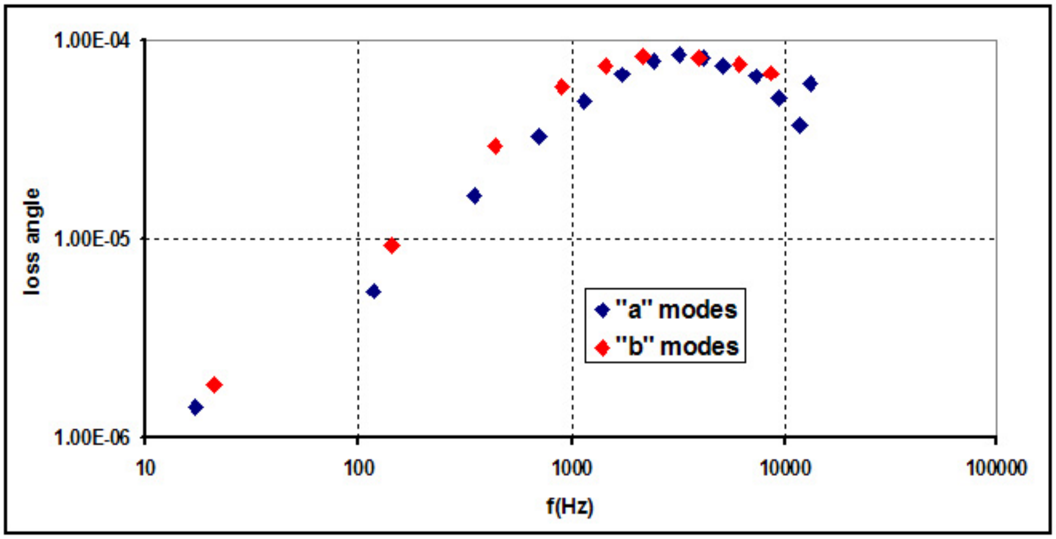

Figure 6.28: Measured loss angle for a 111.5 mm (free length) fibre. The blue and the red squares represent the measured loss angle values relative to “a” and “b” modes respectively.

$$f_i = \frac{1}{2\pi L^2}\sqrt{\frac{EI}{\rho S}}k_i^2 = \frac{d}{8\pi L^2}\sqrt{\frac{E}{\rho}}k_i^2 \,, \tag{6.19}$$

where $k_i = \alpha_i / L$, α_i are the solutions of

$$\cos(\alpha)\cosh(\alpha) + 1 = 0 \tag{6.20}$$

and E, S and I are Young's modulus of the material, the section and the cross-section moment of inertia of the fibre. A very good approximation for α_i values is

$$\alpha_i = \begin{cases} 1.8755\ , & \text{for } \ i = 1\ , \\ (i - \frac{1}{2}\pi)\ , & \text{for } \ i \geqslant 2\ . \end{cases} \tag{6.21}$$

Therefore, in the case of an elliptical fibre there will be a split of each resonance in doublets. The frequencies will roughly correspond to the ones of the cylindrical fibres with sections tangent to the ellipse as shown in figure 6.29.

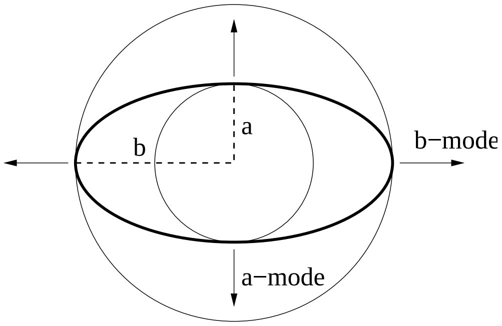

Figure 6.29: The section of an elliptical fibre is shown together with the direction of the split modes due to the difference between the 2 semi-axes "a" and "b" of the ellipse. The modes relative to the shorter axis are at a lower frequency and usually called *a-modes*; the ones relative to the longer axis are at a higher frequency and called *b-modes*.

6.5 Extraction of silicon thermo-mechanical properties

The analysis done for extracting the silicon thermo-mechanical properties from the measurement of the thermoelastic peak resides on the finite element model realized with `ANSYS`® (see § 6.4.3). The model is constructed on the data coming from profile measurements, as described in § 6.3.2. Therefore it is important to estimate carefully the errors coming from the profilation procedure.

6.5.1 Estimating the errors of the profilation

The data coming from the profilation apparatus are pure numbers, taken as ratios R between the signals coming from the detection photodiode and the reference one (see figure 6.14 on page 143). Therefore they need a calibration to be converted in displacements. It is better to do the calibration just before and after the profiles measurement on a fibre.

A series of wires of well known diameter is measured with the profilation apparatus bringing a set of data like the ones reported in figure 6.30. The

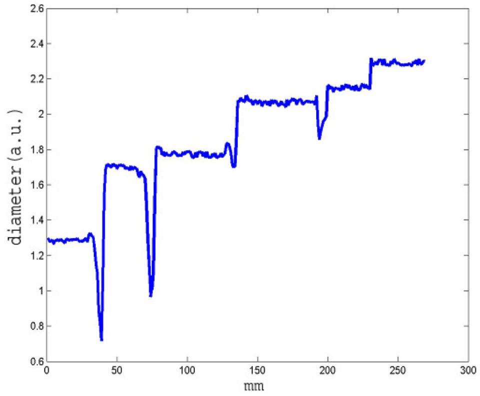

Figure 6.30: Profile of the series of wires used for calibrating the profile measurement apparatus.

ratio R and its error are taken to be the mean and the mean square difference of the oscillations in each of the six steps. The values are fitted with a straight line $R(d)$:

$$R = ad + b \tag{6.22}$$

and the value of the diameter can be extracted:

$$d(R) = \frac{R - b}{a} \tag{6.23}$$

The error σ_d on d is calculated as

$$\sigma_d^2 = \frac{1}{a^2}(\sigma_R^2 + d^2\sigma_a^2 + \sigma_b^2) \tag{6.24}$$

and it is around 100 μm, i.e. around 10%, dominated by the σ_a^2 term. To measure the fibre profile there is also an independent method, more precise but extremely slow. It resides on the possibility of taking several photos of the fibre profile with a digital camera set on a microscope. The photos are merged into a unique image that is processed by a `MATLAB`® program that finds the edges of the fibre. The error for this method is a composition of the error on the pixel/mm conversion factor and the error on the position of the edge found by the algorithm. In figure 6.31, the data obtained with the camera profile (green bars) and the standard procedure (red bars) are shown for a part of a fibre. It is evident that there is a overestimation of the errors for the standard procedure. That is the case for all the regions inspected along the fibre. Thanks to the agreement found, it seems reasonable to downscale the error on the standard profile measurement to the value coming from the camera profilation, i.e. 3.5%.

6.5.2 Young's modulus

From (6.19) it follows that for a cylindrical fibre the value f_i/k_i^2 is constant. For an elliptical one two preferred values are expected. That is what happens, for example, with the 111 mm long fibre as it can be seen in figure 6.32. The data, indicated by blue squares, follow two different trends reflecting the ellipticity of the fibre section; the values are not constant since the fibre geometry is irregular.

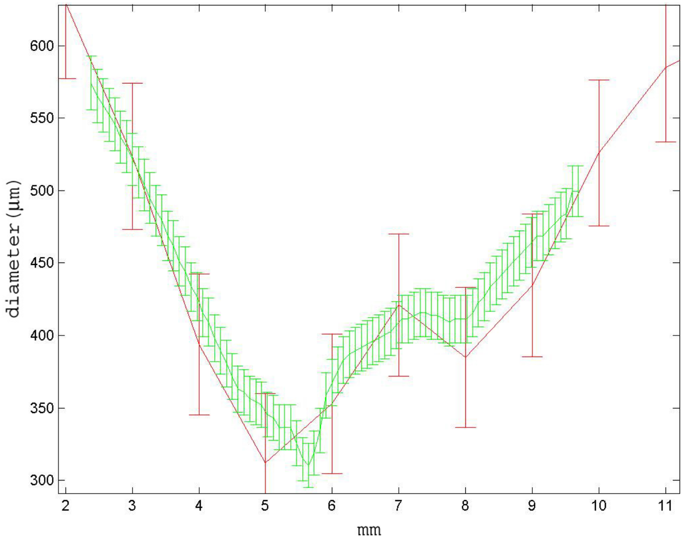

Figure 6.31: Comparison between profile measurements on a part of a fibre, obtained with the digital camera (little green bars) and with the standard procedure (big red bars).

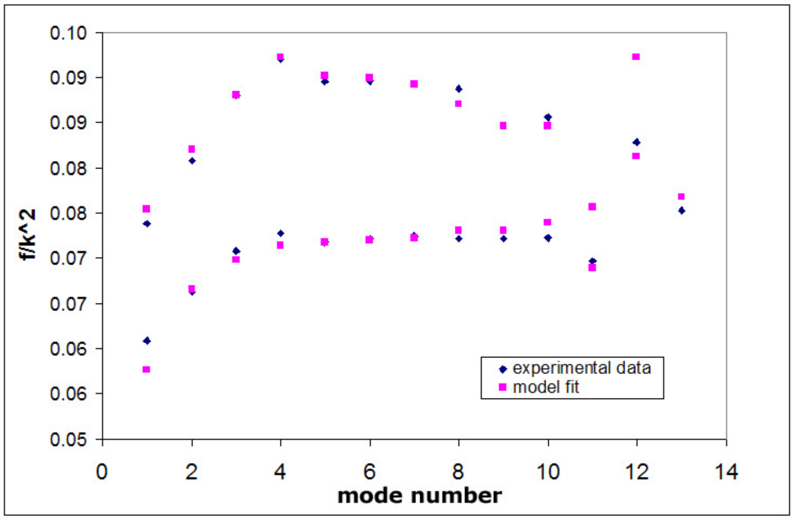

Figure 6.32: Plot of f_i/k_i^2 versus the mode number for the 111 mm long fibre.

With the FEA on the modeled fibre it is possible to predict the values f_i/k_i^2 and find the best Young's modulus E^{best} to use in order to obtain a set of frequencies f_i^{model} that minimizes the quantity

$$\sum_i \left(\frac{f_i^{\text{exp}} - f_i^{\text{model}}}{k_i^2} \right)^2 . \tag{6.25}$$

As for this fibre, E^{best} is 150 GPa with an error of 11 GPa coming mainly from the diameter uncertainty. In figure 6.32 there are also shown, with magenta squares, the values predicted by the FEA using for Young's modulus the obtained value E^{best}. The agreement between data and prediction is very good: since the model considers a fibre whose properties are constant along the length, it is possible to conclude that the geometry of the fibre is taken into account properly and that any variation of the mean[4] Young's modulus is small along the fibre. Using FEA it is also possible to identify some modes which are not purely transversal; in these modes the plane of oscillation changes a lot along the fibre axis (see figure 6.33 a) or the violin-string oscillations are coupled with "breathing" modes (see figure 6.33 b). These modes are not used in thermoelastic analysis since there is not a simple

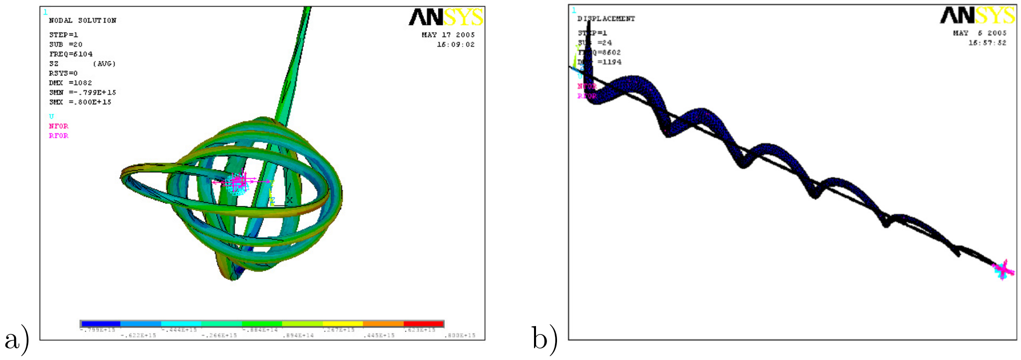

Figure 6.33: Two non-purely-transversal modes of the 111 mm long fibre are shown. In the mode at 6104 Hz (a) the plane of oscillation is changing a lot along the fibre axis. In the mode at 8602 Hz (b) the transversal oscillation is coupled with an "explosion" mode.

---

[4] It can happen that Young's modulus has big changes on the scale of some millimeters or less; in these cases the modes only "see" an average value of Young's modulus, and it is this quantity that has to be considered.

model of the loss angle for these situations.

An analogous analysis on the 308 mm long fibre leads to a value of (174±12) GPa for Young's modulus.

6.5.3 The coefficient of linear thermal expansion

The experimental value of the thermoelastic peak together with its theoretical prediction — equation (3.54) — allows to estimate the coefficient of linear thermal expansion α. By using the known specific heat $c_V = 707$ J/(kgK) and density $\rho = 2330\,\mathrm{kg/m^3}$ of silicon [111], for the 308 mm long fibre the extracted peak value is $\phi_0 = (10.12 \pm 0.12) \times 10^{-5}$.

The error is due to the fact that the thermoelastic peak is sampled only at the resonance frequencies and the maximum amplitude is estimated using the ϕ trend around the peak. The maximum for the peak value was taken equal to the intersection point of the two steepest straight lines that can be constructed with the couples of experimental points just before and after the peak. The minimum for the peak estimate was taken equal to the maximum measured values. An example of the process on this fibre is given in figure 6.34. Assuming for T the measured value of 293 K it follows that $\alpha = (2.56 \pm 0.11) \times 10^{-6}\ \mathrm{K}^{-1}$. For the 111 mm long fibre the extracted value for the peak is $\phi_0 = (17.26 \pm 0.24) \times 10^{-5}$ and $\alpha = (2.54 \pm 0.13) \times 10^{-6}\ \mathrm{K}^{-1}$.

6.5.4 The coefficient of thermal conduction

The τ_{th} parameter in the thermoelastic curve, discussed in § 3.2.2, allows a determination of the thermal conductivity κ of the fibre. The heat flux characteristic time is

$$\tau_{\mathrm{th}} = F \frac{c_V d^2}{\kappa} \tag{6.26}$$

where d is an effective distance for the heat flow and F is a geometrical constant keeping into account the shape of the fibre section. For the measured

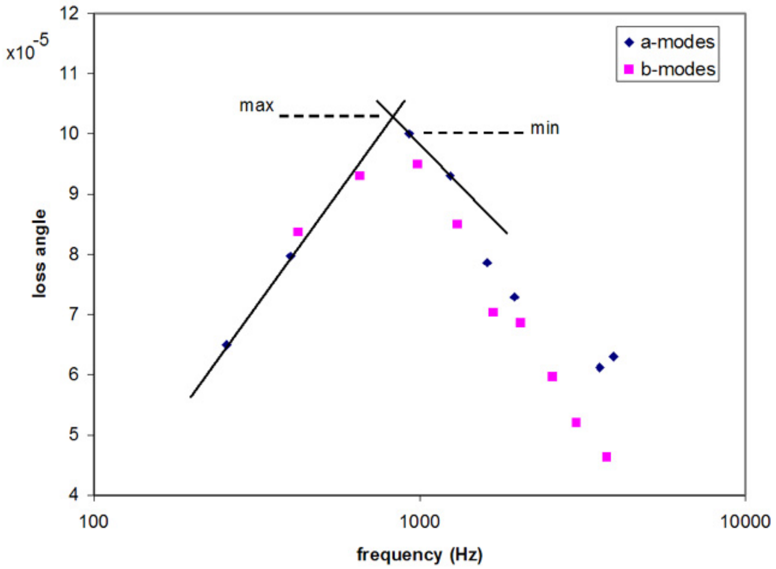

Figure 6.34: An enlargement of loss angle measurements around the thermoelastic peak is shown for the 308 mm long fibre. There are also indicated, as “min” and “max”, the limits of the error interval taken for the peak value.

roughly-elliptical fibres an estimate of d can be deduced for each mode by assuming a cylindrically shaped fibre oscillating at that frequency. In this way the elliptical section is approximated with two circular sections, one with the larger axis as a diameter and the other with the dimension of the shorter axis, for the two main oscillating directions (refer to figure 6.29). Nevertheless the larger curvature radius assumed for the external circular section leads to an underestimation of the heat gradient and consequently to an overestimation of τ_{th}; the opposite happens assuming the internal circular section. A better first order estimation can be obtained by modifying (6.26) with the introduction of a parameter c correcting the form factor known for a cylindrical geometry

$$\tau_{\mathrm{th}} = \frac{1}{2.16}(1 \pm c)\frac{c_V d^2}{\kappa} \,, \tag{6.27}$$

where the sign + in front of c is used when the inscribed circular cross section is taken into account. The values found with a fit by using this expression for the 111 mm long fibre are $\kappa=(146\pm13)$ W/(mK) and $c=0.18\pm0.002$, only considering the pure transverse resonance modes. The error was evaluated varying the model parameters inside their errors. For the 308 mm fibre, performing the same fit, the obtained values are $\kappa = (138 \pm 11)$ W/(mK) and $c=0.001\pm0.001$. In table 6.1 the physical parameters measured for the 111 mm long fibre and the 308 mm long one are summarized.

L (mm)	E (GPa)	α (K^{-1})	κ (W/(mK))
111.5±0.5	150±11	$(2.54\pm0.13)10^{-6}$	146±13
308.0±0.5	174±12	$(2.56\pm0.11)10^{-6}$	138±11

Table 6.1: Measured parameter for two different silicon fibres.

6.6 Future work

The activity described in this chapter has been done in the framework of a larger research program on new materials for interferometric detectors of the 3$^{\text{rd}}$ generation. The group that I belong to is constructing a cryogenic facility to measure, on fibres, the coefficient of thermal conductivity κ, of thermal expansion α and the loss angle ϕ as a function of temperature. In fact, it is of crucial importance to have the possibility of measuring these properties easily, in a robust way and on fibre shaped samples, in order to characterize silicon and new silicon-based materials, whose properties have not been measured yet.

Measuring $\kappa(T)$

Inside a cryostat, already installed and working at liquid nitrogen temperature, there will be a metallic copper box — whose temperature is tunable thanks to coil heaters — inside which a fiber is clamped. The specific thermal conductivity of the fiber will be calculated by measuring fiber geometry and its absolute conductivity (through thermometers at the end of an induced temperature gradient along the fibre itself).

Measuring $\alpha(T)$

The same cryostat will be used for the absolute measurement of the linear coefficient of thermal expansion.

Because of the low value of thermal expansion expected for silicon, which is of the order of $10^{-8}\,\mathrm{K}^{-1}$ (see figure 6.1), the displacement detector should have a stability of 1 nm over a period of 10÷15 minutes. The choice of a suitable optical layout fell on Fabry-Perot cavities.

The final design of the full facility is sketched in figure 6.35. A 20 cm

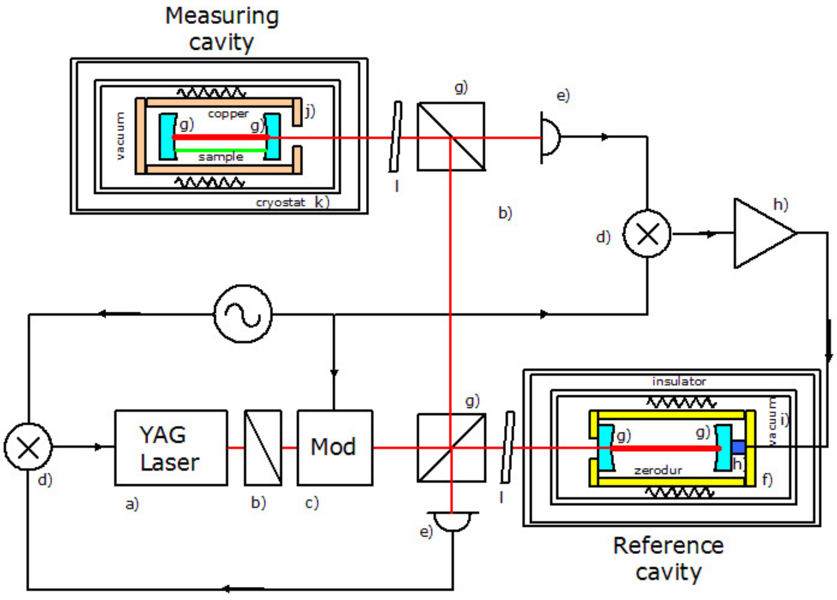

Figure 6.35: Layout of the thermal expansion measurement facility. a) 200 mW Yag laser; b) Faraday isolator; c) EO modulator; d) mixer; e) InGaAs photodiode; f) Zerodur cavity; g) flat-concave optical cavities; h) piezo; i) vacuum tank; j) copper shield; k) cryostat; l) quarter wave plates.

long Zerodur reference cavity controls the frequency of a 200 mW YAG laser through a piezoelectric actuator, which has its negative expansion coefficient partially matched by a washer of aluminum with a suitable thickness. The laser beam coming out of the reference cavity tracks the changes of length in the measuring cavity. The information on the fibre length is contained in the signal fed into the piezo.

Measuring $\phi(T)$

The facility realized for measuring fibers loss angles can be used at cryogenic temperatures with minor changes.

Particular care should be paid in order to realize a clamp that does not become too tight or too loose on the fibre going towards low temperatures. The realization of a composite clamp, made of two different materials — whose thermal expansion coefficients add up to be near the silicon thermal expansion — is being investigated: particular clamps like the one shown in figure 6.36 have been designed and realized. In the future they will be tested on silicon fibres.

Figure 6.36: Sketch of a realized clamp made of brass and aluminum.

Chapter 7

Conclusions

This work has moved from the idea of using finite element analysis (FEA) as a general tool for thermal noise studies relating to improve the performances of interferometric gravitational wave antennae.

On the one hand FEA has been used to simulate some thermal noise contributions for the Virgo mirrors. For the first time ever, a complete model of a Virgo mirror has been used to perform Brownian thermal noise calculations through the numerical dynamic approach, which relies on Levin's method. The analysis is a harmonic FEA, of the same kind as other analyses already made, but presents a series of new important elements:

- the analysis is performed including in one model only all the ancillary components on the mirror: the coating, the markers, the spacers and the magnets (in former analyses all those contributions were investigated separately as worsening inputs);
- the mesh of the coating is driven in a new way, with a double advantage:
  - it allows to apply in a more efficient and precise way the pressure profile on the mirror;
  - it allows the creation of relatively simple models on which parametric analyses can be run;

- the coating is simulated using SHELL99 elements, which allow to define up to 250 layers with different properties.

The results are in agreement with the ones by Levin [46] and by Numata [18]. Besides,

- the effects of the mirror resonance modes on the read-out have been calculated on the actual model of a Virgo mirror through a modal FEA and
- a parametric analysis has been done moving the position of the markers and showing, for the first time, the heuristic relation between the distance of the markers from the laser beam axis and the induced silicate bonding Brownian thermal noise.

On the other hand, in the framework of research of new suspension materials for future interferometric antennae, a facility for measuring fibre loss angle ϕ has been realized. For the first time, measurements on crystalline silicon fibres have been performed with the ring-down technique.

FEA enters that experiment in a novel way: an apparatus to measure the fibre profiles — which, for production problems, is not perfectly cylindrical as aimed to be — has been made and the profile data are used to create finite element models. The creation of the 3-D models of such thin objects resides on the particular mesh-driving process used. A modal analysis allows to find the resonances of the fibers helping the Q-measurement procedure and a parametric analysis w.r.t. Young's modulus E allows to fit E itself from the modeled frequencies and the theoretical wave numbers.

The values obtained for the measured loss angles are consistent with the predicted thermoelastic peaks and are encouraging thanks to the possibility of clamping the fibre without evident clamping losses.

In the future the efforts will be focused on performing:

- a simulation of thermoelastic noise in the mirror;
- a complete simulation of thermoelastic noise in fibres;
- a modelization of the clamping dissipative processes;
- cryogenic measurements of thermal conduction coefficient, thermal expansion coefficient and loss angle on silicon fibres.

Bibliography

[1] A. Einstein, *Sitz.-Ber. Preuß. Akad. Wiss.* (1916) 514

[2] J.H. Taylor and J.M. Wiesberg, *Astrophys. J.* **345** (1989) 434

[3] T. Nakamura, M. Sasaki, T. Tanaka and K.S. Thorne, *Astrophys. J.* **487** (1997) L139

[4] T. Nakamura, *Proc. 2^{nd} TAMA Workshop on Grav. Wave Detection*, Univ. Acad. Press (2000) 123

[5] G.A. Prodi et al., *Proc. 2^{nd} Edoardo Amaldi Conf. on Grav. Waves*, CERN, July (1997) 148; http://www.auriga.lnl.infn.it

[6] P. Astone et al., *Phys. Rev.* D **47** (1993) 362; http://www.lnf.infn.it/esperimenti/rog

[7] P. Astone et al. *Astrophys. J.* **7** (1997) 231; http://www.lnf.infn.it/esperimenti/rog

[8] E. Mauceli et al., *Phys. Rev.* D **54** (1996) 1264; http://sam.phys.lsu.edu

[9] A. Abramovici et al., Science **256** (1992) 325; http://www.ligo.caltech.edu

[10] A. Giazotto, *Phys. Rep.* C **182** (1989) 365; C. Bradaschia et al., *Nucl. Instr. Methods* A **289** (1990) 518; http://www.virgo.infn.it

[11] K. Danzmann et al., *GEO600: Proposal for a 600 m Laser Interferometric Gravitational Wave Antenna*, Max-Planck Institut für Quantenoptik Report **190**, Garching, Germany (1990);
http://www.geo600.uni-hannover.de

[12] K. Tsubono et al., *Proc. Intern. Conf. on Grav. Waves, Sources and Detectors*, World Scientific, Singapore (1997); http://tamago.mtk.nao.ac.jp

[13] A. Buonanno, Y.B. Chen, *Phys. Rev.* D **69** (2004) 102004

[14] A. Brillet et al., *Advanced Techniques*, in *"The Detection of Gravitational Waves"*, D. Blair ed., Cambridge University Press, Cambridge, UK (1999) 369-405

[15] P.R. Saulson, *Fundamentals of Interferometric Gravitational Wave Detectors*, World Scientific, Singapore (1994).

[16] A. Nakagawa, B.A. Auld, E. Gustafson and M.M. Fejer, *Rev. Sci. Instrum.* **68** (1997) 3553

[17] F. Bondu, *Dark Fringe Shot Noise Sensitivity*, Virgo note, VIRNOTOCA1390243 (2003)

[18] K. Numata, *Direct Measurement of Mirror Thermal Noise*, thesis, University of Tokyo (2002)

[19] P.R. Saulson, *Phys. Rev.* D **30** (1984) 732

[20] M. Beccaria et al., *Class. Quant. Grav.* **15** (1998) 3339

[21] J.-Y. Vinet et al, *Phys. Rev.* D **56** (1997) 6085

[22] G. Losurdo, *Ultra-Low Frequency Inverted Pendulum for the Virgo Test Mass Suspension*, Ph.D. thesis, Scuola normale superiore di Pisa (1998)

[23] M. Punturo, *The Virgo Sensitivity Curve*, Virgo note, VIR-NOT-PER-1390-51 (2001)

[24] A. Einstein, *Annalen der Physik* **17** (1905) 549

[25] H.B. Callen and T.A. Welton, *Phys. Rev.* **83** (1951) 34

[26] R.F. Greene and H.B. Callen, *Phys. Rev.* **83** (1951) 1231

[27] H.B. Callen and R.F. Greene, *Phys. Rev.* **86** (1952) 702

[28] R.F. Greene and H.B. Callen, *Phys. Rev.* **88** (1952) 1387

[29] H. Nyquist, *Phys. Rev.* **32** (1928) 110

[30] L.D. Landau and E. M. Lifshitz, *Theory of Elasticity*, Addison-Wesley (1959)

[31] F. Bondu, *Étude de Bruit Termique et Stabilisation en Fréquence du Laser du Détecteur Interférométrique d'Ondes Gravitationelles Virgo*, Ph.D. thesis, Univesité de Paris-Sud, Centre d'Orsay (1996)

[32] J.M. Ziman, *Principles of the Theory of Solids*, 2nd ed., Cambridge University Press (1979)

[33] J.M. Ziman, *Electrons and Phonons. The Theory of Transport Phenomena in Solids*, Oxford University Press (2001)

[34] C. Zener, *Phys. Rev.* **52** (1937) 230

[35] C. Zener, *Phys. Rev.* **53** (1938) 90

[36] J. Ferreirinho, *Internal Friction in High Q Materials*, in *The Detection of Gravitational Waves*, D.G. Blair ed., Cambridge University press, first reprint (1991) 116-151

[37] A.M. Gretarsson and G.M Harry, *Rev. Sci. Instrum.* **70** (1999) 4081

[38] G.M. Harry et al., *Class. Quant. Grav.* **19** (2002) 897

[39] P.R. Saulson, *Phys. Rev.* D **42** (1990) 2437

[40] V.B. Braginsky, V.P. Mitrofanov, V.I. Panov, *System with Small Dissipation*, University of Chicago Press (1985)

[41] A.V. Granato and K. Lücke, *Appl. Phys. J.* **27** (1956) 583

[42] G.I. Gonzáles and P.R. Saulson, *Phys. Lett.* A **201** (1995) 12

[43] M. Kajima, N. Kusumi, S. Moriawaki and N. Mio, *Phys. Lett.* A **264** (1999) 251

[44] N. Ohishi, S. Otsuka, K. Kawabe and K. Tsubono, *Phys. Lett.* A **266** (2000) 228

[45] K. Yamamoto, *Study of the Thermal Noise Caused by Inhomogeneusly Distributed Loss*, Ph.D. thesis, University of Tokyo (2000)

[46] Y. Levin, *Phys. Rev.* D **57** (1998) 659

[47] J.E. Logan, N.A. Robertson, J. Hough and P.J. Veitch, *Phys. Lett.* A **161** (1991) 101

[48] A.D. Gillespie, *Thermal Noise in the Initial LIGO Interferometers*, Ph.D. thesis, California Institute of Technology (1995)

[49] E. Majorana and Y. Ogawa, *Phys. Lett.* A **233** (1997) 162

[50] F. Bondu, J.-Y. Vinet, *Phys. Lett.* A **198** (1995) 74

[51] A.E.H. Love, *A Treatise on the Mathematical Theory of Elasticity*, Dover Publ., New York (1944)

[52] J.R. Hutchinson, *J. Appl. Mech.* **47** (1980) 901

[53] V.B. Braginsky, M.L. Gorodetsky, S.P. Vyatchanin, *Phys. Lett.* A **264** (1999) 1

[54] F. Bondu, P. Hello, J.-Y. Vinet, *Phys. Lett.* A **246** (1998) 227

[55] A. Nakagawa, E. Gustafson, P. Beyersdorf and M.M. Fejer, *Phys. Rev.* D **65** (2002) 082002

[56] Y.T. Liu and K.S. Thorne, *Phys. Rev.* D **62** (2000) 122002

[57] A. Nakagawa, A.M. Gretarsson, E.K. Gustafson and M.M. Fejer, *Phys. Rev.* D **65** (2002) 102001

[58] M. Cerdonio, L. Conti, A. Heidmann and M. Pinard, *Phys. Rev.* D **63** (2001) 082003

[59] G.M. Harry, *Incorporating Coating Anisotropy into Coating Thermal Noise*, LIGO technical note, LIGO-T0040029-00-R (2004)

[60] V.B. Braginsky, S.P. Vyatchanin, *Phys. Lett.* A **312** (2003) 244

[61] M.M. Fejer, S. Rowan, G. Cagnoli, D.R.M. Crooks, A.M. Gretarsson, G.M. Harry, J. Hough, S.D. Penn, P. Sneddon, S.P. Vyatchanin, *Phys. Rev.* D **70** (2004) 082003

[62] S.R. Rao, *Mirror Themal Noise in Interferometric Gravitational Wave Detectors*, Ph.D. thesis, California Institute of Technology, Pasadena, CA (2003)

[63] V.B. Braginsky, M.L. Gorodetsky and S.P. Vyatchanin, *Phys. Lett.* A **271** (2000) 303

[64] M. Punturo, *Advanced Virgo Sensitivity Curve: a Possible Scenario*, Virgo note, VIR-NOT-PER-1390-283 (2004)

[65] J.E. Logan, J. Hough and N.A. Robertson, *Phys. Lett.* A **183** (1993) 145

[66] J. Kovalik and P.R. Saulson, *Rev. Sci. Instrum.* **64** (1993) 2942

[67] G.I. González and P.R. Saulson, *J. Acoust. Soc. Am.* **96** (1994) 207

[68] S. Rowan, G. Cagnoli, P.H. Sneddon, J. Hough, R. Route, E.K. Gustafson, M.M. Fejer and V. Mitrofanov, *Phys. Lett.* A **265** (2000) 5

[69] K. Numata, *Phys. Lett.* A **276** (2000) 37

[70] K. Numata, *Class. Quant. Grav.* **19** (2002) 1697

[71] K. Numata, *Phys. Lett.* A **327** (2004) 263

[72] P. Willems and D. Busby, *Report to the April 25, 2003 Core Optics Downselect Commettee Meeting*, LIGO technical note, LIGO-T030087-00-R (2003)

[73] J.R. Smith, G. Cagnoli, D.R.M. Crooks, M.M. Fejer, S.J. Goßler, H. Lück, S. Rowan, J. Hough and K. Danzmann, *Class. Quant. Grav.* **21** (2004) S1091

[74] S.D. Penn, A. Ageev, D. Busby, G.M. Harry, A.M. Gretarsson, K. Numata and P. Willems, *Frequency and Surface Dependence of the Mechanical Loss in Fused Silica*, arxiv.org/abs/gr-qc/0507097 (2005)

[75] J. Wiedersich, S.V. Adichtchev and E. Rössler, *Phys. Rev. Lett.* **84** (2000) 2718

[76] S.D. Penn, G.M. Harry, A.M. Gretarsson, S.E. Kittelberger, P.R. Saulson, J.J. Shiller, J.R. Smith, S.O. Sword, *Rev. Sci. Instrum.* **72** (2001) 3670

[77] A. Ageev, B.C. Palmer, A. De Felice, S.D. Penn, P.R. Saulson, *Class. Quant. Grav.* **21** (2004) 3887

[78] J.-Y. Vinet, *Noises Produced by Opto-Thermal Couplings in Mirrors*, Virgo note, VIR-NOT-OCA-1390-166 (2001)

[79] K. Yamamoto, S. Otsuka, M. Ando, K. Kawabe and K. Tsubono, *Phys. Lett.* A **280** (2001) 289

[80] K. Yamamoto, M. Ando, K. Kawabe and K. Tsubono, *Phys. Lett.* A **305** (2002) 18

[81] K. Yamamoto, S. Otsuka, M. Ando, K. Kawabe and K. Tsubono, *Class. Quant. Grav.* **19** (2002) 1689

[82] K. Yamamoto, S. Otsuka, Y. Nanjo, M. Ando and K. Tsubono, *Phys. Lett.* A **321** (2004) 79

[83] A.M. Gretarsson, G.M. Harry, S.D. Penn, P.R. Saulson, J.J. Shiller, W.J. Startin, *Proc.* 3^{rd} *Edoardo Amaldi Conf. on Grav. Waves*, July 12-16 (1999)

[84] D.R.M. Crooks et al., *Class. Quant. Grav.* **19** (2002) 883

[85] S.D. Penn et al., *Class. Quant. Grav.* **20** (2003) 2917

[86] M.N. Inci, *Simultaneous Measurements of Thermal Optical and Linear Thermal Expansion Coefficients of* Ta_2O_5 *Films*, ICO 19, Firenze, Italy, August 25-30 (2002)

[87] C.-L. Tien, C.-C. Jaing, C.-C. Lee, and K.-P. Chuang, *J. Mod. Opt.* **47** (2000) 1681

[88] V.B. Braginsky and A.A. Samoilenko, *Phys. Lett.* A **315** (2003) 175

[89] S.P. Baker, C.R. Ottermann, M. Laube, F. Rauch, and K. Bange, *Proc. Mat. Res. Soc. Symp.*, Pittsburgh, PA, **436** (1997) 71

[90] A, Gillespie and F. Raab, *Phys. Lett.* A **178** (1993) 357

[91] A, Gillespie and F. Raab, *Phys. Lett.* A **190** (1994) 213

[92] G. Cagnoli, L. Gammaitoni, J. Kovalik, F. Marchesoni, M. Punturo, S. Braccini, R. De Salvo, F. Fidecaro and G. Losurdo, *Phys. Lett.* A **237** (1997) 21

[93] S. Traeger, B. Willke and K. Danzmann, *Phys. Lett.* A **225** (1997) 39

[94] S. Rowan, S.M. Twyford, J. Hough, D.-H. Gwo and R. Route, *Phys. Lett.* A **246** (1998) 471

[95] A.Y. Ageev, I.A. Bilenko, V.B. Braginsky and S.P. Vyatchanin, *Phys. Lett.* A **227** (1997) 159

[96] A.Y. Ageev, I.A. Bilenko and V.B. Braginsky, *Phys. Lett.* A **246** (1998) 479

[97] A.M. Gretarsson and P.R. Saulson, *Monitoring the Thermal and Non-Thermal Excitation of Fibers*, http://www.ligo.org/pdf_public/saulson.pdf

[98] G. Cagnoli, L. Gammaitoni, J. Kovalik, F. Marchesoni and M. Punturo, *Phys. Lett.* A **255** (1999) 230

[99] V.B. Braginsky, V.P. Mitrofanov and K.V. Tokmamov, *Phys. Lett.* A **218** (1996) 164

[100] G. Cagnoli, L. Gammaitoni, J. Hough, J. Kovalik, S. McIntosh, M. Punturo and S. Rowan, *Phys. Rev. Lett.* **85** (2000) 2442

[101] S. Rowan, R. Hutchins, A. McLaren, N.A. Robertson, S.M. Twyford and J. Hough, *Phys. Lett.* A **227** (1997) 153

[102] A.M. Gretarsson, G.M. Harry, S.D. Penn, P.R. Saulson, W.J. Startin, S. Rowan, G. Cagnoli and J. Hough, *Phys. Lett.* A **270** (2000) 108

[103] Ansys version 8.1, ANSYS Inc., Canonsburg, PA, USA (2004) http://www.ansys.com

[104] A.V. Aho, B.W. Kernighan, P.J. Weinberger, *The AWK Programming Language*, Addison-Wesley (1988)

[105] M. Punturo, F. Travasso, *Evaluation of the bulk loss angle of the Virgo Mirrors from C2 data*, Virgo note, VIR-NOT-PER-1390-263 (2004)

[106] D.R.M. Crooks et al., *Class. Quant. Grav.* **21** (2004) S1059

[107] P.H. Sneddon, S. Bull, G. Cagnoli, D.R.M. Crooks, E.J. Elliffe, J.E. Faller, M.M. Fejer, J. Hough and S. Rowan, *Class. Quant. Grav.* **20** (2003) 5025

[108] S.M. Hu, *J. Appl. Phys.* **53** (1982) 3576

[109] D.F. McGuigan et al., *J. Low Temp. Phys.* **30** (1978) 621

[110] C.C. Lam and D.H. Douglas, *Phys. Lett.* A **85** (1981) 41

[111] Material Properies Database (MPDB), http:/www.jahm.com

[112] G. Cagnoli, L. Gammaitoni, J. Kovalik, F. Marchesoni and M. Punturo, *Rev. Sci. Instrum.* **71** (2000) 2206

[113] D.H. Yoon and T. Fukuda, *J. Cryst. Gr.* **144** (1994) 201

[114] V. Chani, A. Yoshikawa, Y. Kuwano, K. Hasagawa and T. Fukuda, *J. Cryst. Gr.* **204** (1999) 155

[115] http://www.ni.com/labview

[116] S.K. Ghandi, *VLSI Fabrication Principles*, Wiley, New York, 2nd ed. (1994)

[117] Matlab version 6.5, The MathWorks Inc., Natick, MA, USA (2002) http://www.mathworks.com